Indexed / Abstracted in:

TR-Dizin, EXALY Full-Text Search Engine, Index Copernicus, Root Indexing, Google Scholar,
Harvard University Library, Scilit, journaltocs, Sobiad Fatcat, Cite Factor

Aims and Scopes

European Mechanical Science (EMS) is an international, peer reviewed journal which publishes full length original research papers, reviews related to all areas of Mechanical Engineering such as: Solid Mechanics, Materials Engineering, Automotive Engineering, Fluid Mechanics, Thermal Engineering, Engine and Power Engineering, Dynamics & Control, Robotics & Mechatronics, Transportation Engineering, Computational Mechanics, Design, Systems, Manufacturing, BioMedical Engineering; Process Engineering, Aerospace Engineering. No charges are required from the Authors to publish the articles.EMS is a quarterly published journal operating an online submission and peer review system. It allows authors to submit articles online and track their progress via its web interface.

https://dergipark.org.tr/ems

Contents

– *Research Articles*

Investigation of an energy pile application and its economic analysis

Sertaç Coşman[1*], Olcay Kıncay[2]

[1]Burdur Mehmet Akif Ersoy University, Department of Mechanical Engineering, Türkiye
[2]Yıldız Technical University, Faculty of Mechanical Engineering, Türkiye

Orcid: S. Coşman (0009-0005-9360-216X), O. Kıncay (0009-0006-1232-2789)

Abstract: In this study, the heating and cooling needs of an airplane hangar by integrating a heat pump system into bored piles were investigated. For this purpose, U-type pile heat exchangers were installed inside the piles. 600 bored piles were integrated with heat exchangers depending on the heating requirements of the hangar. Energy calculations were performed for a single pile, and the total amount of energy that could be extracted from the ground was determined. The main goal is to supply cooling and heating for the hangar throughout the year without the use of any additional conventional system. Thus, cost-analysis results for both the heat pump and traditional system using levelized cost method were presented. The study results showed that the annual operating cost $(C_{OM})_{PW}$, total operating cost $(I_{OM})_{PW}$, equivalent annual operating cost (C_{OM}), and total annual cost (C_T) for the present condition reduced by nearly 38.5%, 35%, 35%, and 34% against the conventional system, respectively. The simple payback period was calculated as 1.1 years. Finally, it was seen that using the energy piles can provide the heating and cooling requirements of the hangar throughout the year without any additional conventional system.

Keywords: Ground source heat pump, Energy pile, Pile heat exchanger, Renewable energy.

1. Introduction

The substantial increase in fossil fuel consumption over recent decades has led to the buildup of greenhouse gases, ultimately causing global warming, and giving rise to irregular weather patterns and health issues. To address this, numerous approaches have been explored to reduce global warming. These include enhancing the efficiency of current energy conversion processes through the utilization of effective energy conversion devices, which have minimal or zero environmental impacts. Some examples include fuel cells powered by environmentally friendly fuels like hydrogen, methanol, ethanol, wastewater, etc. Additionally, efforts involve transitioning towards renewable energy sources such as solar, biomass, wind, ocean, and geothermal energy [1,2].

A key solution for global warming and the fossil energy crises is the advancement and use of renewable energy. The benefits of vast reserves and global distribution have drawn more attention to geothermal energy in recent years as a clean and sustainable energy source. As a prominent form of renewable energy, geothermal energy has outstanding benefits such as high sustainability, low emissions, and eco-friendly. Its application varies based on ground temperature, electricity generation, direct heating, and indirect heating/cooling through heat pumps. The utilization of ground source heat pump

systems (GSHPs) has grown dramatically in the last few decades all over the world. This is attributed to their low carbon footprint and capacity to gain heat from the ground for building both cooling and heating purposes in various climate conditions. Besides, previous studies have shown that GSHPs are more efficient than HVAC technologies with reduced running costs. Because GSHP units and installation have high capital costs, and are still higher than that of standard systems. However, if governments provide extra incentives, GSHPs may be an affordable alternative solution [3-5].

Although various methods exist for utilizing soil as an energy source, energy piles represent the latest innovation in this field. In unstable foundations, a heat exchange pipe is inserted into a bored pile to reinforce the ground and additionally utilize soil heat. This system is installed at a reasonable cost, making it a desirable option. Therefore, it has become one of the most sought-after cooling and heating systems in recent times. A brief review of some significant research articles about energy piles is presented here. Chen et al. developed a machine learning-based algorithm for COP estimation, an important indicator in GSHPs. A field study was performed for two years on energy pile systems integrated into the heat pump. Study results indicated that the ambient temperature significantly influenced COP performance, while humid-

ity had a comparatively minimal impact [6]. Mousa et al. conducted a simulation study using the 3-D finite element method to examine the performance of Phase Change Material (PCM) on energy piles. The study revealed that the heat pump COP performance increased up to 5.28% using PCM with high latent heat capacity [7]. Cui and Zhu investigated the whole-year performance of a GSHP with multiple energy piles using a 3-D heat transfer model. The GSHP cooling and heating capabilities were analyzed. The findings of the study revealed that the maximum heating and cooling COPs were 3.63 and 4.73 respectively in the whole season operation period [8]. Carotenuto et al. developed a numerical model to assess the heat transfer performance on energy piles with different configurations. Presented results in the study indicated that the heat transfer performance was increased by up to 42% using concrete with a higher thermal conductivity coefficient [9]. Fadejev et al. researched a review study on energy pile design in geothermal plants. In this study, a high overall system of Seasonal Coefficient of Performance (SCOP) value was higher than 4.5 in properly designed heat pump systems integrated energy piles. However, the impact of convenient design and sizing was demonstrated by SCOP values that were twice as low in some certain case studies [10]. Fadejev and Kurnitski used simulation software to evaluate the performance of the whole building SCOP for cold climate conditions in Finland. Simulation results indicated that utilizing borehole heat exchanger fields and energy piles might yield substantial heat pump SCOP values of up to 5.3 in a commercial hall-type building [11]. Moon and Choi investigated the heating performance characteristics of GSHPs with energy piles and energy slabs. Study findings revealed that the heat pump unit achieved minimum COP values of 4.2 for the energy pile system and 4.5 for the energy slab system [12]. Morrone et al. investigated the technical and economic viability of utilizing geothermal heat pumps (GHPs) with energy piles for cooling and heating in residential houses [13]. Two-story building designed as both an office and residential building was constructed, and friction piles were used on the ground in Sapporo. Four different U-type pile heat exchangers were tested. Heat dissipation rates were calculated for three of these four different heat exchangers, and performance test results were compared. The single U-type pile heat exchanger was selected in terms of economic efficiency and usability [14]. A research project in Austria explored the heat transfer between soil/concrete and the absorber fluid circulating in the pipes, along with a discussion on pile arrangement. The study results indicated that factors such as well resistance and soil shear resistance did not change significantly during the heat drawing from the ground [15]. A case study was conducted to evaluate the application of geothermal energy in heating and cooling systems in Shanghai, China. Several performance tests were then performed to identify the most efficient option among four different pile heat exchangers, and numerical results were compared against experimental data. The W-type heat exchanger was chosen as the preferred model [16]. In another study conducted in Shanghai, average, numerical, and experimental results for W-type and three different

U-type configurations of pile heat exchangers for different flow rates were analyzed. It was found that the W-type had 43% more heat dissipation than the U-type [17]. Moel et al. pointed out the technological advantages of energy pile systems. It was stated that the applications of these systems provide significant energy savings [18]. Wood et al. investigated the effect of using a pile system as a heat exchanger in combination with a GSHP for residential heating. The results of the study indicated that the total energy gain from the heat pump throughout the entire heating season was 17.24 MWh [19]. Singh et al. performed an experimental study by designing a small pile in Victoria City, Australia. Based on the study results, if the system were fully implemented in a multi-purpose office building, it would save around $60,000 per year on its energy bills, and reduce 400 tons of CO_2 emissions annually [20]. Cui et al. conducted a study to compare spiral-type pile heat exchangers to other heat exchanger types in terms of heat conduction. It was revealed that the spiral-type pile heat exchanger has an advantage in both heat transfer area and flow profile [21]. Suryatriyastuti et al. carried out a simulation study to understand the heat transfer mechanism in the pile system. Parameters related to the heat transfer process in the pile and soil system such as soil temperature, thermal properties of the soil, groundwater flow, and its effect were presented [22]. Amatya et al. performed a study to analyze the axial stresses in the concrete pile because of heating-cooling. In addition, axial thermal load profiles and their effects on the soil around the pile were investigated [23].

In this study, the heating requirement of an airplane hangar built in Istanbul Sabiha Gökçen International Airport was investigated using an energy pile system. U-type pile heat exchangers were installed inside the piles. 600 bored piles were integrated with heat exchangers depending on the heating requirements of the hangar. Energy calculations were performed for a single pile, and the entire potential energy that could be driven from the ground was determined. The main goal is to supply cooling and heating for the hangar throughout the year without the use of any additional conventional system. Therefore, the cooling requirement of the hangar was also considered in the cost analyses. Finally, cost-analysis results are presented for both the conventional and the heat pump integrated energy pile system using the levelized cost method.

2. Material and Methods

2.1. Energy Pile Systems and Operating Principle

In modern high-rise buildings, bored piles are used to strengthen the ground during foundation works on soils with poor bearing properties due to static problems. When pipelines are integrated into these piles to utilize geothermal energy, they are called energy piles. In other words, heat can be extracted from the ground for building heating, and it can be transferred to the ground for building cooling. The pile foundations allow heat to be extracted from the ground to utilize the heat energy stored in summer and winter for heating and cooling

purposes in residences using a heat pump.

The use of geothermal energy has become quite widespread in recent years. Geothermal energy varies in depth from 10 to 50 meters in many European countries, with an average soil temperature of 10-15°C. Energy extraction through pile foundations is a relatively new concept. Such a technology can be described as acquiring thermal energy from the ground through heat exchangers that are connected to a building's heat pump. The soil provides heat energy to the building during the winter and takes on the cooling role for the summer season.

Figure 1 depicts the energy pile system and its elements [22]. These systems include three basic cycles. In the first cycle, the soil is used as a heat source for the building's needs in the winter season, and the summer season vice versa, that is, the heat is given to the soil for cooling purposes. The second cycle is where the heat carrier fluid is transferred from the soil to the building via absorbing pipes in the concrete pile. The third cycle is a heating-cooling circuit consisting of closed pipelines embedded in the floors and walls of the building. The amount of energy production depends on the performance coefficient defined for the heat pump. The COP range typically varies between 3.0-6.0. For the best economic energy
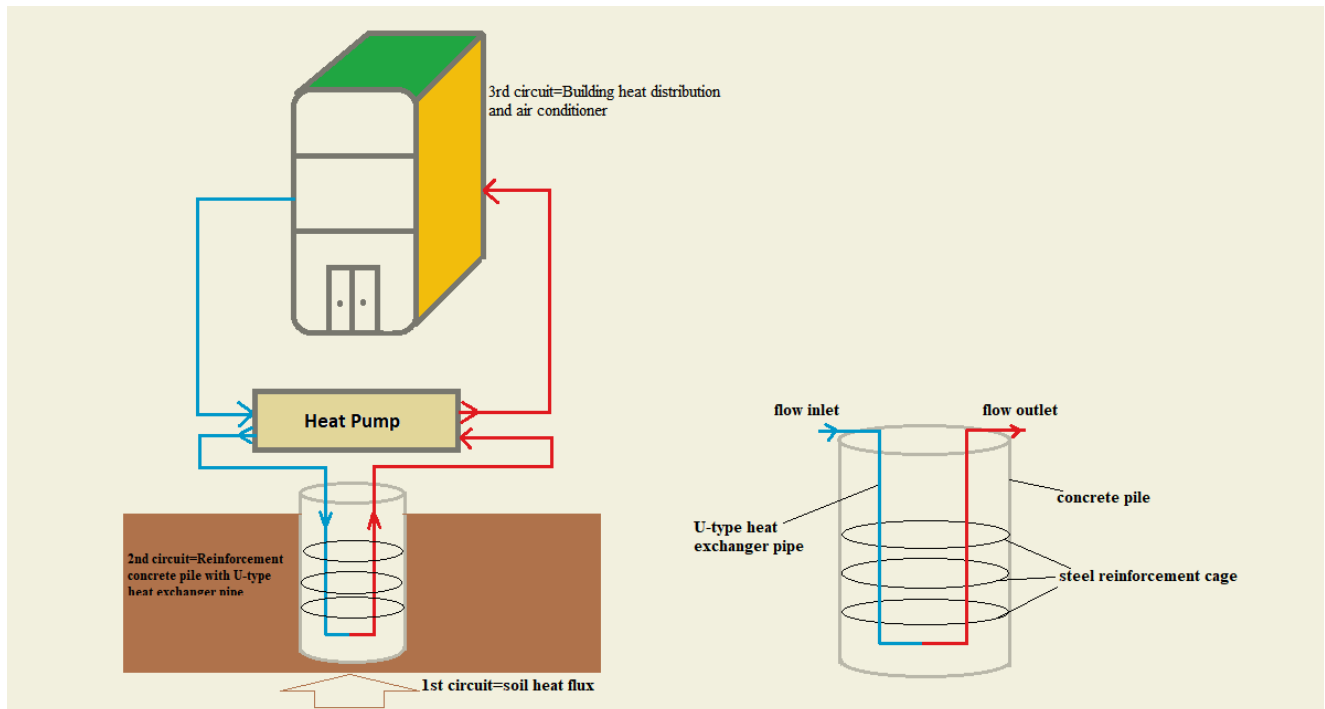
Figure 1. Energy pile cycle and its components
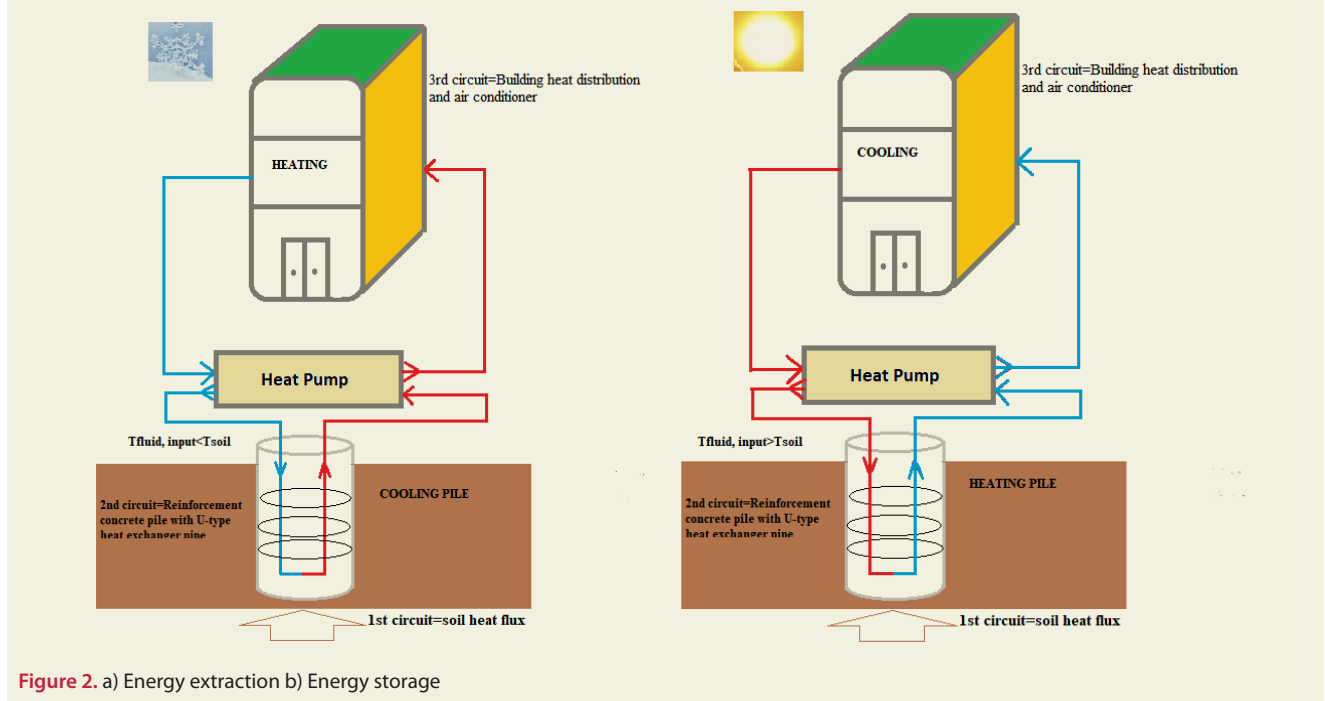
Figure 2. a) Energy extraction b) Energy storage

production, the COP should be 4.0 or above.

There are two types of operating in energy piles: one-way operating and seasonal operation mode. In the one-way operating mode, energy flow occurs only in one direction. In seasonal operation mode, the aim is to maintain the thermal balance in the soil. In this mode, heat is extracted from the ground during certain periods, while in other periods, heat is supplied to the ground. The thermal balance of the soil is maintained by both cooling and heating throughout the year. This operating system is preferred for its environmental friendliness in sustaining underground water. Energy extraction and storage are shown in Figure 2.a and Figure 2.b respectively [22].

2.2. Pile Installation

Piles containing steel pipes are usually filled with concrete, and concrete columns are equipped with heat-absorbing pipes using vibroflotation technique. In short, the vibroflotation method is a technique of compacting deep granular soils with vibratory drilling tools. Hence, ground strength increases using this compaction meth-

od [24]. In addition to this system, pile heat exchangers are installed. Installation phases for energy pile are illustrated in Figure 3 (a,b,c,d,e,f). First, the reinforcement cage where the pile heat exchanger pipes will be mounted is prepared (Figure 3.a). In the second stage, boreholes are drilled in the area where the piles will be driven (Figure 3.b). In the third stage, heat exchanger pipes are integrated into the prepared reinforcement cage (Figure 3.c). In the fourth stage, the cage is placed inside the casing pipe in the drilled hole. The purpose of the casing pipe is to ensure that the cage is correctly and stably placed in the boreholes (Figure 3.d). In the fifth stage, a funnel is placed over the cage and the borehole is filled with mortar (Figure 3.e). Finally, the casing pipe is removed again, and the pile construction is completed (Figure 3.f). The final state of the energy piles is shown in Figure 4 [25].

2.3. Energy Calculation for Pile Circuit

When the static project of the hangar was studied, it was determined that a total of 1.000 bored piles with a diameter of 80 cm and a length of 25 m were used. The height of the hangar is 32 m. Its length and width are 160 m and

Figure 3. Installation stages of energy pile [25]

Figure 4. Final state of energy piles [25]

180 m, respectively. Underfloor heating was envisaged in the project, and the heat requirement was determined as 1.100 kW. The interior temperature of the hangar was set at 18 °C. In order to meet the heating load of the hangar, it has been suggested to convert 600 bored piles into energy piles. Typically, the distance between the boreholes is taken as 5-7 m in the studies conducted for the vertical GSHPs [26,27]. According to the data in the project, the desired distance between the pile wells is 4 m or more, which is acceptable in terms of heat transfer in the soil. The aim is to extract maximum heat from the energy piles. Therefore, it was decided to use a U-module pipe to achieve the maximum possible energy gain. Since the heat transfers to the piles from the soil, the structure of the soil plays an important role in energy extraction. In practice; first, the lateral surface area (m²) of the pile is calculated. Then, the energy value that can be extracted from the surface, based on the soil type is multiplied by 10-35 W/m². Since the pile diameter is 80 cm and the soil type is slightly moist-clayey, the specific heat capacity is considered 25 W/m² in the study [25]. Soil types and specific heat capacity values are listed in Table 1.

Table 1. Soil Types and Specific Heat Capacity [28]

Soil Types	Specific Heat Capacity [W/m²]
Dry, Sandy Soil	10 – 15
Moist, Sandy Soil	15 – 20
Dry, Clayey Soil	20 – 25
Moist, Clayey Soil	25 – 30
Watery Ground (groundwater)	30 – 35

Once the soil type is determined, the energy extracted from the pile can be calculated. The lateral surface area of the pile is determined by

$$A_{pile-lateral} = \pi \cdot D \cdot L_{pile} \tag{1}$$

where D is the pile diameter, and L_{pile} is the pile length. Energy extraction for one pile can be expressed as

$$Q_{pile} = A_{pile-lateral} \cdot \text{Specific Heat Capacity} \tag{2}$$

Four heat exchangers have been installed in each pile. Thus, the energy obtained from each heat exchanger has been calculated as 0.392 kW. The total energy obtained from the energy pile system is determined by

$$Q_{pile,t} = Q_{pile} \cdot n_{pile} \tag{3}$$

where n_{pile} is the number of energy piles used in the system. $Q_{pile,t}$ was found to be 942 kW. This result gives us the maximum amount of energy that can be extracted from the primary circuit, i.e. through the pile heat exchangers [29]. A cross-section view of a pile with heat exchangers is shown in Figure 5.
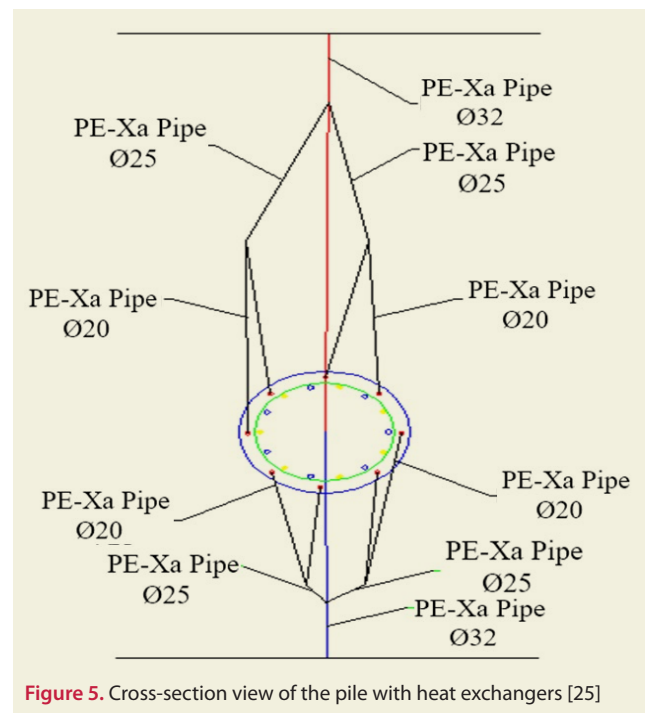
Figure 5. Cross-section view of the pile with heat exchangers [25]

There are four U-type heat exchangers (cross-linked polyethylene, PE-Xa) inside each pile. Pipes having 20 mm diameter are connected to a diameter of 25 mm pipes in pairs. Pipes with a diameter of 25 mm are connected to 32 mm ones. Finally, the pipes with a diameter of 32 mm, which leave from the pile, are attached to the pipe in the collector line. Hence, 20 piles were gathered in one collector. The connection diagram for one collector is illustrated in Figure 6.

There are 6 collectors in the critical line. The last collector is connected to the main line leading to the heat pump. Calculations for collector-1 on the critical line are done similarly. The heating power has been recalculated since 20 energy piles are connected to each collector. The heating power for each collector can be calculated using Equation 4.

$$Q_{collector} = 20 \cdot Q_{pile} \tag{4}$$

Thus, the heating power for collector-1 was found to be

31.4 kW. The COP value of the heat pump used in the system is 3.5. The heat pump capacity can be determined by Equation 5.

$$Q_{capacity} = Q_{pile,t} \cdot \left(\frac{COP}{COP-1} \right) \quad (5)$$

The heat pump capacity was determined as 1,318.8 kW. This value calculated at the heat pump output easily meets the heat loss of the airplane hangar. It was deemed appropriate to use two ground source heat pumps, each with a capacity of 600 kW [25,29].

2.4. Cost Analysis

The initial investment costs and operating costs for the conventional and heat pump integrated energy pile systems were evaluated separately. The amount of total annual energy costs for both systems was obtained using the levelized cost method [30,31].

2.4.1. Initial Investment Costs

While calculating the initial investment cost for the heat pump system, piping and labor, pump, expansion tank, and heat pump device were taken into consideration as system components. For the conventional system, components such as natural gas installation and labor, chimney, chiller, and boiler have been considered [25,29]. Initial investment cost values (I_A) for both systems are shown in Table 2.

2.4.2. Operating Costs

When calculating operating costs, the annual heating energy requirement, annual electricity consumption, and costs are determined based on the operating times throughout the summer and winter seasons for both the traditional and heat pump systems. The results were presented in the discussion section.

Heating cost calculations for the winter season (Heat Pump System):

First, the annual heating energy has been calculated. The operating time of the heat pump for the winter season is 1,440 hours in total for 6 months (October-November-December-January-February-March) with an average of 8
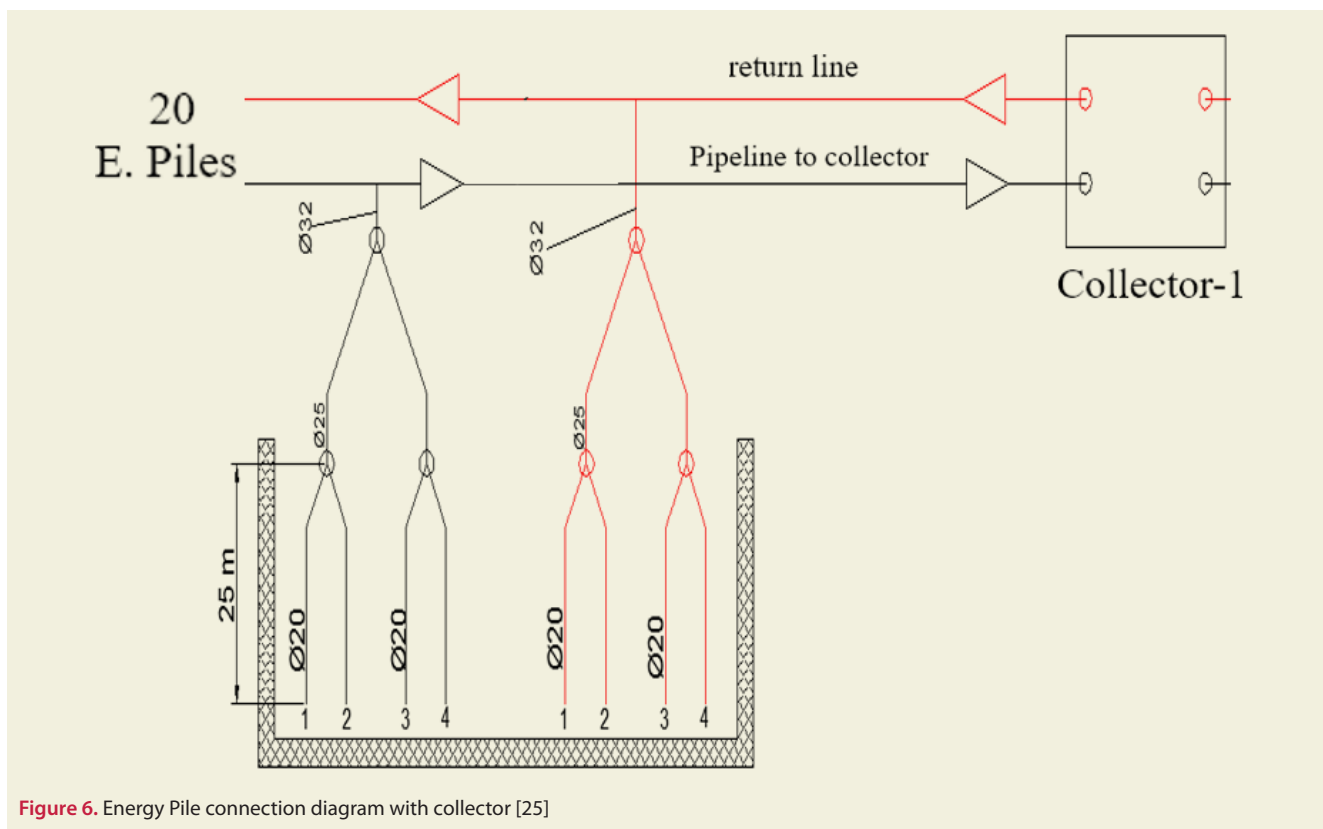
Figure 6. Energy Pile connection diagram with collector [25]

Table 2. Initial investment cost values for heat pump and conventional system

Heat Pump System		Conventional System	
System Components	Price [€]	System Components	Price [€]
Piping and Labor	24,000	Natural Gas Installation and Labor	10,000
Pump	2,000	Chimney	4,500
Expansion Tank	800	Chiller	42,000
Heat Pump (2)	2x35,000	Boiler	20,000
I_A: 96,800 €		I_A: 76,500 €	

hours per day. The annual heating energy requirement (AHER) for the winter season can be defined as

$$AHER = Q_{HHR} \cdot t_{operating} \tag{6}$$

where Q_{HHR} is the hangar heat requirement. The annual electricity consumption (AEC) is given in Equation 7.

$$AEC = \frac{AHER}{COP} \tag{7}$$

The COP for heating in the winter season is 3.5. The unit price of electricity determined by Turkish Electricity Distribution Corporation (TEDAŞ) is taken as 0.19 €/kWh [32]. The annual heating cost (AHC) can be calculated by using Equation 8.

$$AHC = AEC \cdot \text{Electricity Unit Price} \tag{8}$$

Similarly, the cooling cost was also calculated for the summer season. The average operating time of the heat pump device is 10 hours a day over 6 months (April-May-June-July-August-September) for a total of 1,600 hours. The COP value of the heat pump for the summer season is taken as 6.

The same calculation method was applied to conventional systems. The operating times are the same as those of the heat pump system. The calorific value of natural gas (NGCV) and the gas unit price provided by Istanbul Gas Distribution Corporation (IGDAS) are taken as 8,250 kcal/m³ and 0.42 €/m³ [33]. The boiler efficiency was chosen as 0.90. The natural gas requirement over the operation period and its cost were obtained by using the relations given in 9 and 10, respectively.

Heating cost calculations for the winter season:

$$ANGR = \frac{AHER}{NGCV \cdot \eta_{boiler}} \cdot 860 \tag{9}$$

$$AHC = ANGR \cdot \text{Natural Gas Unit Price} \tag{10}$$

In the same way, the cooling cost for the conventional system was calculated. The COP value of Chiller is taken as 2.2.

For a better comparison, the levelized cost method was used to calculate the expenses incurred during the installation and operation of the device by bringing them to a certain reference date [30,31]. The annual cost of initial investment (C_A) is determined by

$$C_A = I_A \cdot DF \tag{11}$$

where DF is the damping factor. DF is calculated by using Equation 12.

$$DF = \frac{(1+i)^n \, i}{(1+i)^n - 1} \tag{12}$$

The total life-cycle period of the system (n) is estimated as 20 years, and the nominal annual interest rate (i) is considered as 3%. The annual operating cost for present conditions $(C_{OM})_{PW}$ covers mainly electricity, fuel costs, and annual maintenance costs (AMC) for the system. $(C_{OM})_{PW}$ is determined by Equation 13.

$$(C_{OM})_{PW} = AOC + MC \tag{13}$$

The average maintenance costs for the heat pump system, boiler, and chiller are determined to be 200 €/year, 600 €/year and 400 €/year, respectively. The total operating cost for present conditions $(I_{OM})_{PW}$ is expressed as

$$(I_{OM})_{PW} = (C_{OM})_{PW} \frac{1}{(i - e_f)} \left[1 - (1 + e_f)^n (1 + i)^{-n} \right] \tag{14}$$

where e_f is the escalation rate. When calculating $(I_{OM})_{PW}$, the future annual escalation rate (e_f) is taken as 2.5% for natural gas, and 4% for electricity [31]. Therefore, the boiler and chiller were evaluated separately for the conventional system. Equivalent annual operating cost and total annual cost relations are given in Equation 15 and 16, respectively.

$$C_{OM} = (I_{OM})_{PW} \cdot DF \tag{15}$$

$$C_T = C_A + C_{OM} \tag{16}$$

Finally, the simple payback period for the system can be determined by using Equation 17.

$$\text{Payback Time} = \frac{(I_A)_{\text{Heat Pump}}}{(C_{OM})_{PW,\text{Conventional}} - (C_{OM})_{PW,\text{Heat Pump}}} \tag{17}$$

3. Results and Discussion

First, the soil type was determined. Then the energy extracted from the pile was calculated. Since the energy obtained from each pile heat exchanger is determined as 0.392 kW, the calculated heating power for one pile or pile circuit is 1.57 kW. Each collector line has twenty piles. Thus, the heating capacity for each collector in the critical line was found to be 31.40 kW. The heating powers of pile heat exchangers and collectors for each line are given in Table 3.

Calculations were carried out for other collectors. The distance between each collector is 15 m. The main pipeline to heat pump which is connected to collector-6 is 50 m. The energy pile installation diagram for cirtical line is shown in Figure 7.

Table 3. Heating powers for pile heat exchangers and collector lines

	Pile Circuit	Line 1	Line 2	Line 3	Line 4	Line 5	Line 6 (Connected to mainline)
Line Length [m]	25	40	15	15	15	15	50
Heating Power [kW]	1.57	31.40	62.80	94.20	125.60	157	188.40

Table 4. Annual operating costs for heat pumps and conventional system

Heat Pump System			Conventional System		
Heating Cost [€/year]	Cooling Cost [€/year]	Annual Operating Cost [€/year]	Heating Cost-Boiler[€/year]	Cooling Cost-Chiller[€/year]	Annual Operating Cost [€/year]
85,988.5	55,733.3	141,721.8	77,056	152,000	229,056

Table 5. All cost results for heat pump and conventional system

System Type	I_A [€]	C_A[€/year]	$(C_{OM})_{PW}$ [€/year]	$(I_{OM})_{PW}$ [€]	C_{OM}[€/year]	C_T[€/year]
Heat Pump	96,800	6,505	141,922	3,025,372	203,305	209,810
Conventional	76,500	5,140	230,056	4,689,065	315,105	320,245
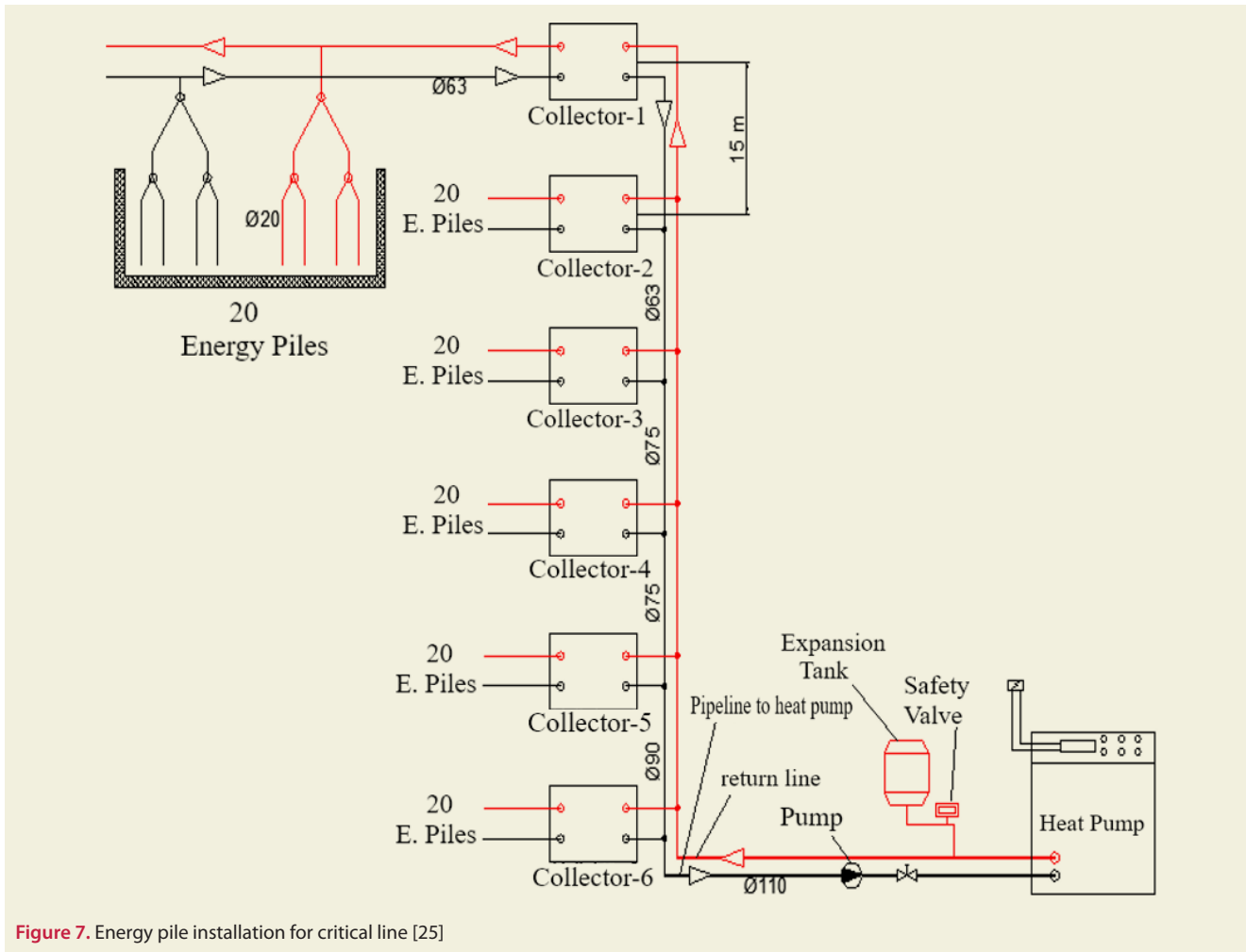
Figure 7. Energy pile installation for critical line [25]

Operating cost calculations were considered separately for heat pump and conventional system. When the heat pump system was used for the pile application, it was seen that the annual operating costs almost decreased by %40 compared to the conventional system. The annual operating costs (AOC) for both systems are given in Table 4.

For a better comparison, the costs incurred during the installation and operation of the devices have been evaluated using levelized cost method. Thus, C_A, $(C_{OM})_{PW}$, $(I_{OM})_{PW}$, C_{OM} and C_T were calculated for present condition. Based on the final cost results, it was shown that the $(C_{OM})_{PW}$, $(I_{OM})_{PW}$, C_{OM} and C_T decreased by approximately 38.5%, 35%, 35% and 34% compared to conventional system, respectively. Finally, simple payback period was

calculated as 1.1 years. All cost results for heat pump and conventional systems were presented in Table 5.

4. Conclusion

In this study, it was aimed to heat an airplane hangar at Sabiha Gökçen Airport using energy piles. Depending on the static project of the hangar and the heat requirement, U-type heat exchangers were integrated into the bored piles. Underfloor heating was envisaged for the hangar, and the heat requirement was determined as 1,100 kW. It was suggested to convert 600 bored piles into energy piles. First, energy extraction for one pile was calculated. Then the total energy gain from the system was obtained. The energy drawn from each pile, and total primary circuit

was calculated as 1.57 kW and 942 kW, respectively. The initial investment costs and operating costs for the heat pump and the conventional systems were calculated. The calculations performed for the heating and cooling season were carried out separately. Similar procedure was applied for cooling season as well. Finally, levelized cost method was used to perform cost analysis for both heat pump and conventional system. Results are presented as follows:

- When the heat pump system was used for the pile application, it was shown that the annual operating costs nearly decreased by %40 compared to conventional system.

- Cost analysis results for the heat pump and conventional systems have been found as: 6,505 and 5,140 €/year for annual cost of initial investment, 141,922 and 230,056 €/year for operating costs, 3,025,372 and 4,689,065 € for total annual operating costs, 203,305 and 315,105 €/year for equivalent annual operating costs for present condition.

- Based on the cost analysis results, it was seen that the $(C_{OM})_{PW}$, $(I_{OM})_{PW}$, C_{OM} and C_T decreased by approximately 38.5%, 35%, 35% and 34% compared to conventional system, respectively.

- Simple payback period has been calculated as 1.1 years. The critical point here is that the initial investment cost values obtained for both systems are close to each other. It might be explained by the fact that there is no additional drilling cost in energy piles. Therefore, the system amortized itself in a short time.

As a result, the heating and cooling needs of the hangar can be met throughout the year using the energy pile system without any additional conventional system.

Conflict of Interest

The authors declare that there is no conflict of interest regarding the publication of this paper.

Nomenclature

GSHP	Ground Source Heat Pump
COP	Coefficient of Performance
I_A	Initial Investment Cost
AHER	Annual Heating Energy Requirement
AEC	Annual Electricity Consumption
AHC	Annual Heating Cost
ANGR	Annual Natural Gas Requirement
AOC	Annual Operating Cost
MC	Maintenance Cost
DF	Damping Factor
C_A	Annual Cost of Initial Investment
$(C_{OM})_{PW}$	Annual Operating Cost for Present Condition
$(I_{OM})_{PW}$	Total Operating Cost for Present Condition
C_{OM}	Equivalent Annual Operating Cost
C_T	Total Annual Cost

References

[1] Olabi, A. G., Mahmoud, M., Obaideen, K., Sayed, E. T., Ramadan, M., & Abdelkareem, M. A. (2023). Ground source heat pumps: Recent progress, applications, challenges, barriers, and role in achieving sustainable development goals based on bibliometric analysis. Thermal Science and Engineering Progress, 101851.

[2] Shen, J., Zhou, C., Luo, Y., Tian, Z., Zhang, S., Fan, J., & Ling, Z. (2023). Comprehensive thermal performance analysis and optimization study on U-type deep borehole ground source heat pump systems based on a new analytical model. Energy, 274, 127367.

[3] Luo, J., Zhang, Q., Liang, C., Wang, H., & Ma, X. (2023). An overview of the recent development of the Ground Source Heat Pump (GSHP) system in China. Renewable Energy.

[4] Li, H. X., Okolo, D. E., Tabadkani, A., Arnel, T., Zheng, D., & Shi, L. (2023). An integrated framework of ground source heat pump utilisation for high-performance buildings. Scientific Reports, 13(1), 371.

[5] Miglioli, A., Aste, N., Del Pero, C., & Leonforte, F. (2023). Photovoltaic-thermal solar-assisted heat pump systems for building applications: Integration and design methods. Energy and Built Environment, 4(1), 39-56.

[6] Chen, Y., Kong, G., Xu, X., Hu, S., & Yang, Q. (2023). Machine-learning-based performance prediction of the energy pile heat pump system. Journal of Building Engineering, 77, 107442.

[7] Mousa, M. M., Bayomy, A. M., & Saghir, M. Z. (2022). Long-term performance investigation of a GSHP with actual size energy pile with PCM. Applied Thermal Engineering, 210, 118381.

[8] Cui, Y., & Zhu, J. (2018). Year-round performance assessment of a ground source heat pump with multiple energy piles. Energy and Buildings, 158, 509-524.

[9] Carotenuto, A., Marotta, P., Massarotti, N., Mauro, A., & Normino, G. (2017). Energy piles for ground source heat pump applications: Comparison of heat transfer performance for different design and operating parameters. Applied Thermal Engineering, 124, 1492-1504.

[10] Fadejev, J., Simson, R., Kurnitski, J., & Haghighat, F. (2017). A review on energy piles design, sizing and modelling. Energy, 122, 390-407.

[11] Fadejev, J., & Kurnitski, J. (2015). Geothermal energy piles and boreholes design with heat pump in a whole building simulation software. Energy and buildings, 106, 23-34.

[12] Moon, C. E., & Choi, J. M. (2015). Heating performance characteristics of the ground source heat pump system with energy-piles and energy-slabs. Energy, 81, 27-32.

[13] Morrone, B., Coppola, G., & Raucci, V. (2014). Energy and economic savings using geothermal heat pumps in different climates. Energy Conversion and Management, 88, 189-198.

[14] Hamada, Y., Saitoh, H., Nakamura, M., Kubota, H., & Ochifuji, K. (2007). Field performance of an energy pile system for space heating. Energy and Buildings, 39(5), 517-524.

[15] Brandl, H. (2006). Energy foundations and other thermo-active ground structures. Géotechnique, 56(2), 81-122.

[16] Gao, J., Zhang, X., Liu, J., Li, K. S., & Yang, J. (2008). Thermal performance and ground temperature of vertical pile-foundation heat exchangers: A case study. Applied Thermal Engineering, 28(17-18), 2295-2304.

[17] Gao, J., Zhang, X., Liu, J., Li, K., & Yang, J. (2008). Numerical and experimental assessment of thermal performance of vertical energy piles: an application. Applied Energy, 85(10), 901-910.

[18] De Moel, M., Bach, P. M., Bouazza, A., Singh, R. M., & Sun, J. O. (2010). Technological advances and applications of geothermal energy pile foundations and their feasibility in Australia. Renewable and Sustainable Energy Reviews, 14(9), 2683-2696.

[19] Wood, C. J., Liu, H., & Riffat, S. B. (2010). An investigation of the heat pump performance and ground temperature of a piled foundation heat exchanger system for a residential building. Energy, 35(12), 4932-4940.

[20] Singh, R. M., Bouazza, A., Wang, B., Barry-Macaulay, D., Haberfield, C., Baycan, S., & Carden, Y. (2011). Geothermal Energy Pile: Thermal cum Static Load Testing.". In Australian Geothermal Energy Conference (pp. 245-248).

[21] Cui, P., Li, X., Man, Y., & Fang, Z. (2011). Heat transfer analysis of pile geothermal heat exchangers with spiral coils. Applied Energy, 88(11), 4113-4119.

[22] Suryatriyastuti, M. E., Mroueh, H., & Burlon, S. (2012). Understanding the temperature-induced mechanical behaviour of energy pile foundations. Renewable and sustainable energy reviews, 16(5), 3344-3354.

[23] Amatya, B. L., Soga, K., Bourne-Webb, P. J., Amis, T., & Laloui, L. (2012). Thermo-mechanical behaviour of energy piles. Géotechnique, 62(6), 503-519.

[24] López-Querol, S., Peco, J., & Arias-Trujillo, J. (2014). Numerical modeling on vibroflotation soil improvement techniques using a densification constitutive law. Soil Dynamics and Earthquake Engineering, 65, 1-10.

[25] REHAU Polimeri Kimya Sanayi Anonim Şirketi, İstanbul, October 2012. https://www.rehau.com/tr-tr

[26] Zhang, H., Han, Z., Li, X., Ji, M., Zhang, X., Li, G., & Yang, L. (2021). Study on the influence of borehole spacing considering groundwater flow and freezing factors on the annual performance of the ground source heat pump. Applied Thermal Engineering, 182, 116042.

[27] Puttige, A. R., Andersson, S., Östin, R., & Olofsson, T. (2022). Modeling and optimization of hybrid ground source heat pump with district heating and cooling. Energy and Buildings, 264, 112065.

[28] Republic of Türkiye Ministry of Environment, Urbanization and Climate Change. General Technical Specifications for Mechanical Installation, Heat Pumps. (accessed date: 11 December 2023). https://webdosya.csb.gov.tr/db/yfk/icerikler//sartname-mgts-15-isi-pompalari-20201026120829.pdf

[29] Deltam Mühendislik ve Ticaret Ltd. Şti. Ümraniye, İstanbul. Isı Pompası Uygulamaları, 22 April 2013.

[30] Aybers, N., Şahin, B. (1995). Enerji Maliyeti. Yıldız Teknik Üniversitesi Yayınları, No. 299.

[31] Kıncay, O., Akbulut, U., Ağustos, H., Açıkgöz, Ö., & Çetin, Ö. (2008). Güneş Enerjisi ve Toprak Kaynaklı Isı Pompası Sistemlerinin Konvansiyonel Sistemlerle Ekonomik Olarak Karşılaştırılması. Tesisat Mühendisliği, 106.

[32] Turkish Electricity Distribution Corporation. (accessed date: 17 June 2013). https://www.tedas.gov.tr/tr/1

[33] Istanbul Gas Distribution Corporation (accessed date: 17 June 2013). https://www.igdas.istanbul/

Research Article

The influence of the raster angle on the dimensional accuracy of FDM-printed PLA, PETG, and ABS tensile specimens

Oğuz Tunçel[1*]

[1]Siirt University, Engineering Faculty, Mechanical Engineering Department, Siirt, Türkiye

Orcid: O. Tunçel (0000-0002-6886-6367)

Abstract: 3D printing is a rapidly developing manufacturing method that produces objects in layers. Fused Deposition Modelling (FDM) is a 3D printing technology where the material is melted in a hot nozzle and placed on a build platform to create a prototype layer by layer. In this study, the effects of different raster angles (0°, 45°, 90°, 45°/-45°, 0°/90°) on dimensional accuracy for PLA, PETG, and ABS materials produced using FDM were investigated. The results revealed that PETG generally shows higher dimensional deviations than PLA and ABS. Samples with a raster angle of 90° typically have lower deviation percentages than other angles. Width deviations (approximately 1.5% on average) were lower than thickness deviations (about 9.5% on average). Analysis of the cross-sectional areas shows that all samples are above the theoretical area (41.6 mm^2). PETG samples with a raster angle of 45°/-45° exhibit the largest cross-sectional area (46.78 mm^2), while ABS samples with a raster angle of 90° exhibit the smallest (45.46 mm^2). This study is essential to understand the impact of material selection and raster angle on dimensional accuracy, and it is recommended to account for cross-sectional deviations and calculate the stress based on the actual cross-sectional area to achieve more accurate results in applications requiring precise measurements. These data offer valuable information for those interested in 3D printing and its professionals and can lead to further research in this field so that printing techniques can be further developed and product quality can be improved.

Keywords: Dimensional accuracy, raster angle, FDM, PLA, PETG, ABS

1. Introduction

3D printing is a rapidly advancing manufacturing technique that produces parts in layers. 3D printing uses 3D computer-aided design (CAD) data to convert it directly into a physical prototype. Most 3D printing methods involve dividing a computer-aided design (CAD) model into successive 2D layers and constructing the prototype by layering them one upon another. This technology has distinct advantages over traditional manufacturing techniques, such as producing very complex geometries, assembled functional parts, lattice structures, and multi-material components without tooling [1–5].

Fused deposition modeling (FDM) is a widely embraced additive manufacturing (AM) technique for producing three-dimensional components. It involves depositing material layer by layer using a plasticizing nozzle that moves in the X-Y plane. In this process, a material filament is melted in a heated nozzle and deposited on a building platform. This nozzle is moved in the XY plane using a 3-axis motion system and prints a prototype layer. Once a layer is finished, the build platform descends by one increment, referred to as the slice thickness, in the

Z direction, and the sequence is reiterated for the subsequent layer until the entire model is constructed [6–9].

Previous studies examining the dimensional accuracy of parts produced by FDM are included in this paragraph. Frunzaverde et al. [10] examined FDM-printed PLA tensile specimens, exploring the impact of filament color. They varied layer heights (0.05 mm, 0.10 mm, 0.15 mm, 0.20 mm) and filament colors (natural, black, red, grey). Results showed color significantly affected both dimensions and tensile strength. The two-way ANOVA revealed PLA color (η^2 = 97.3%) as the dominant factor for strength, followed by layer height (η^2 = 85.5%) and their interaction (η^2 = 80.0%). Black PLA excelled in dimensional accuracy (0.17% width, 5.48% height), while grey PLA exhibited high tensile strength (57.10 MPa to 59.82 MPa) under identical conditions. Bolat and Ergene [11] studied how filament type and layer height affect dimensional accuracy in 3D printed tensile test samples (PLA, PET-G, ABS) using Fused Filament Fabrication (FFF). Varying layer heights (0.2 mm, 0.3 mm, 0.4 mm) maintained consistent parameters, except for nozzle and platform temperature. They measured length, width,

and height, comparing results with design dimensions. PLA had the best surface quality, while PET-G excelled in length and height accuracy. Tezel's study [12] explores additive manufacturing, which is vital in machine design and part production. A popular method, FDM uses polymers like ABS, PLA, and PET-G, impacting part strength and surfaces. Precise 3D printing relies on parameters like speed and temperature. PET-G samples (hollow and solid), 5-15 mm diameter, were made with FDM, varying temp (220°C, 240°C) and speed (30 mm/s, 40 mm/s) to assess dimensional accuracy, highlighting temperature's impact. Stojković et al. [13] focused on PLA, PETG, and carbon fiber-reinforced PETG in 3D printing. They investigated annealing's impact on tensile strength and dimensions, varying layer heights (0.1 mm, 0.2 mm, 0.3 mm), and annealing conditions (60–100°C, 30–90 min). Regression models highlighted layer height's dominant effect on strength. Optimal settings were determined for each material. PETGCF showed minimal dimensional changes and the best elasticity. This study adds crucial insights to the annealing discussion in 3D printing. Akbaş et al. [14] studied nozzle temperature and feed rate effects on FDM part dimensional accuracy with ABS and PLA. They used both simulations and experiments with varying parameters. PLA outperformed ABS in accuracy. Higher nozzle temps increased PLA strip width, but effects were mixed for ABS. Increased feed rates reduced strip width. A regression model ranked the importance of measurement position, feed rate, and nozzle temp. Finite element modeling accurately predicted polymer swell. Future work includes refining three-dimensional modeling with non-symmetric conditions. Mohanty et al. [15] optimized ABS M30 parts using FDM and the MARCOS Method, establishing purposeful dimension relationships. Findings favored a part orientation of a 30°, a layer thickness of 0.127 mm, 30° raster angle, 0.004 mm air gap, and 0.5064 mm raster width via ten nature-inspired meta-heuristic methods. Component orientation played a pivotal role in ensuring FDM-built item dimensional accuracy. This study enhances FDM optimization, elevating component construction quality by considering diverse process constraints and complex geometric factors. Çakan's study [16] on FDM revealed that varying raster angles significantly impact polymer filament parts. The ultimate tensile strength decreased with increasing raster angle, peaking at 0° for maximum strength. Additionally, ±45° angles exhibited the highest ductility, with fracture mechanisms dependent on raster orientation. Tanoto et al. [17] investigated FDM 3D printing using ABS plastic, assessing machine parameters' impact on outcomes. They explored three deposit orientations (XY, YX, ZX), measuring processing time, dimensional accuracy, and strength. The third orientation was the fastest (2432 seconds), followed by the first and second. Dimensional accuracy varied compared to ASTM 638-02 standards. Tensile tests revealed the second orientation with the highest strength (7.66 MPa), followed by the first and third (6.8 MPa and 3.31 MPa, respectively). This research highlights the influence of process parameters on 3D printing.

In the present study, tensile specimens with different raster angles (0°, 45°, 90°, 45°/-45°, 0°/90°) were produced according to ASTM D638-I standard using FDM technology. Five different raster angles were applied for PLA, PETG, and ABS materials. This study mainly investigates the effects of raster angle on the dimensional accuracy of tensile specimens for three different materials.

2. Material and Method

In this study, Creality brand CR-PLA, CR-PETG, and CR-ABS filaments are the materials used in sample production. All filaments are 1.75 mm in diameter. PLA, PETG, and ABS filaments are white, yellow, and grey, respectively. Due to their widespread use, these filaments were preferred as test materials [18].

The printing processes of the samples were carried out using a Creality Ender3 S1 Pro 3D printer. This printer allows a print size of 220x220x270mm. The maximum nozzle temperature of the 3D printer is 300 °C, the maximum table temperature is 110 °C, and the maximum printing speed is 150 mm/s. The test specimens used in the study were first designed in the Solidworks 2020 CAD program in accordance with the dimensions specified in ASTM D638–I [19]. Figure 1 shows the dimensions of the ASTM D638 standard type I test specimen on the technical drawing. The designed specimen geometry was converted to ".stl" file format and transferred to the CURA 5.4.0 program. CURA 5.4.0 program is used to create the G codes required for the 3D printer. In addition, thanks to this program, different manufacturing parameters can be determined with the 3D printer [20]. The fixed parameters used in the study are shown in Table 1. As the printing temperature, the middle value of the temperature range specified by the manufacturer was selected for all three filaments. The 3D printer and the image of the samples produced according to ASTM D638-I are given in Figure 2.

Sample width and thickness measurements were taken from the marked points shown in Figure 1 to evaluate the

Table 1. Printer, slicing program, and fixed parameters used in the experiments.

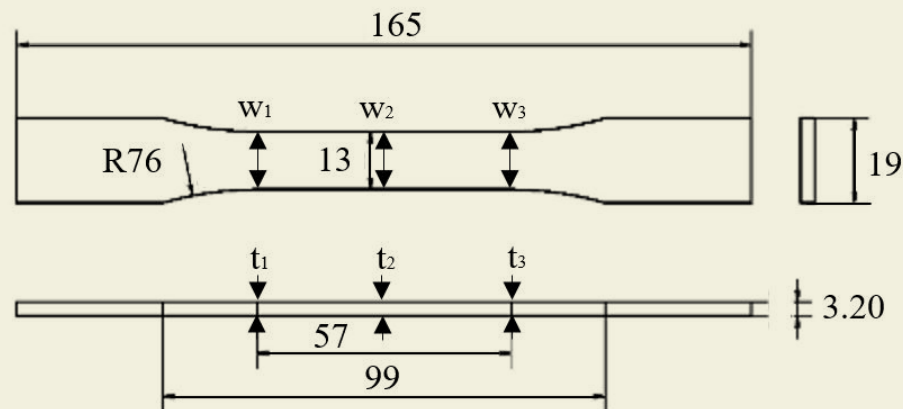| 3D Printer	Creality Ender3 S1 Pro
Slicing Program	Ultimaker Cura
Printing Temperature (°C)	PLA:210, PETG:240 ABS:260
Built Plate Temperature (°C)	PLA:60, PETG:70, ABS:110
Infill Density (%)	100
Infill Pattern	Lines
Layer Height (mm)	0.2
Print Speed (mm/s)	60
Nozzle Diameter (mm)	0.4
Wall Line Count	1
Top/Bottom Thickness (mm)	0.1
Fan Speed (%)	100

Figure 1. The CAD geometry of the printed samples with the positions of the dimensional accuracy measurements (w_1, w_2, w_3-width measurements; t_1, t_2, t_3- thickness measurements)

dimensional accuracy. The measurements were carried out with a KMP brand digital micrometer with a measuring width of 150 mm and an accuracy of ±0.01 mm. For each specimen, measures were taken for widths w_1, w_2, and w_3 and thicknesses t_1, t_2, and t_3. Three specimens were produced for each raster angle parameter, and w and t measurements were made for all three specimens (Figure 3). The mean and standard deviation values of the width and thickness measurements were calculated for each sample. Dimensional accuracy percentages and standard deviation values of these percentages were also calculated by considering the average results of three samples produced for each parameter result. Since the cross-sectional area in the tensile test is used as the basis for stress calculation, the w (mm) x t (mm) values (mm²) were also calculated, and the deviation of the area from the theoretical area was revealed.

3. Results and Discussion

This section gives width and thickness measurements varying with raster angle, and various dimensional accuracy calculations are made based on these measurements. The dimensional deviation percentages obtained as a result of the calculations are graphed. The graphi-
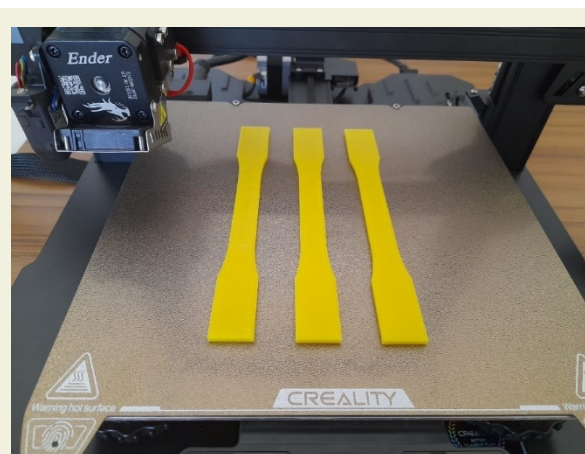

Figure 2. Image of some sample tensile specimens produced by 3D printer.

cal data allows us to compare the dimensional accuracy output varying with different material groups and raster angles. Sample width (w_1, w_2, and w_3) and thickness (t_1, t_2, and t_3) measurements were obtained from the measurement points shown in Figure 1. The raw results obtained from the measurements are given in Table 2.

Table 2 was used to calculate the width deviation varying with raster angle. Firstly, average widths were determined. The percentage deviation of these average widths from the theoretical width of 13 mm was calculated. The changing percentage deviations and the standard deviation values of these deviations are illustrated in Figure 4. In Figure 4, the y-axis scale was changed between 0-14% to be compatible with the thickness scale. The lowest average width value was 13.10 mm for the sample with PLA 45° raster angle, and the highest average width value was 13.27 mm for the sample with PETG 45°/-45° raster angle (Table 2). The width deviation ratio between the samples with the lowest and highest average widths varied between 0.79-2.08% (Figure 4). When Figure 4 is analyzed, it is seen that the width deviation in PETG measurements is higher than PLA and ABS. The average width measurement (mm) of the PETG sample is approximately 0.7% and 0.09 mm higher than the PLA and ABS samples. The percentage of width deviation (%) for PLA, PETG, and ABS specimens is in the order of PETG, ABS, and PLA, starting from the highest. The percentage of width deviation (%) for raster angles are in the following order, starting from the largest: 0°, 45°/-45°, 0°/90°, 90° and 45°. There is a difference of approximately 32% between the deviation rates (%) of the samples with 0° raster angle, which shows the highest percentage deviation, and the samples with 45° raster angle, which shows the lowest percentage deviation. If we look at the effect of the raster angle on the width deviation for each material individually, the highest deviation for PLA is 0°, the lowest deviation is 45°, the highest deviation for PETG is 45°/-45° and the lowest deviation is 45°, the highest deviation for ABS is 0° and the lowest deviation is 90°. This shows that the effects of raster angle on the width deviation are dissimilar in different materials.

The percentage deviations of the measured sample thicknesses with respect to the theoretical thickness of 3.2 mm are given in Figure 5. In the average thicknesses calculated based on Table 2, the highest thickness value is 3.55 mm for the PLA sample with a 45° raster angle, and the lowest is 3.47 mm for the PLA sample with a 0° raster angle. When Figure 5 is analyzed, it is seen that there are very small differences between the material and the varying thickness averages. The average thickness values in mm are PLA, PETG, and ABS, ranging from large to small. Percentage thickness deviations generally varied around 9.5%. In terms of raster angle, the percentage deviations are ranked as 45°, 0°/90°, 45°/-45°, 90°, and 0° starting from the largest. While the average percentage deviation of three different materials for 45° is 10.32%, this rate is 9.06% for 0°. While the length deviation rate was around 2% in width measurements, it was observed that it increased considerably in thickness measurements, rising to around 10%. If we look at the effect of raster angle on thickness deviation for each material individually, the highest deviation for PLA is 45°, the lowest deviation is 0°, the highest deviation for PETG is 0°/90°, and the lowest deviation is 0°, the highest deviation for ABS is 0° and the lowest deviation is 90°. For ABS, the highest deviation is 0°, and the lowest deviation is 90° in both width and thickness measurements. For PLA, the highest deviation angle of 0° in width measurements showed the lowest deviation angle in thickness measurements, and the lowest deviation angle of 45° in width measurements showed the highest deviation angle in thickness measurements.

In order to evaluate and visualize the overall effect of sample thickness and width on dimensional accuracy, average cross-sectional areas varying with raster angle are shown in Figure 6. The average cross-sectional area in all samples is greater than the theoretical cross-sectional area of 41.6 mm². While the largest cross-sectional area is 46.78 mm² in the PETG sample with a raster angle of 45°/-45°, the lowest cross-sectional area is 45.46 mm² in the ABS sample with a raster angle of 90°. When the average cross-sectional areas for all specimens are ranked according to the raster angle, the order from largest to smallest is 45°, 0°-90°, 45°-45°, 0° and 90°. When the area deviation is considered as the average of the three samples in general, the lowest deviation was at 90 degrees. PLA, PETG, and ABS were at 0°, 0°, and 90°, respectively. When the averages of the cross-sectional areas varying with the raster angle are considered material differences, the order of the area is PETG, PLA, and ABS from large to small.

Cross-section deviations in percentage terms are shown in Figure 7. In percentage terms, the deviation rate generally varied around 11.5%. The highest percentage deviation is 12.45% for the sample with PETG 45°/-45° raster angle, and the lowest percentage deviation is 9.28% for the sample with ABS 90° raster angle. The lowest percentage deviations of the cross-sectional area for PLA, PETG, and ABS materials are 9.71%, 10.72%, and 9.28% for 0°, 0°, and 90° raster angles, respectively. When the cross-sectional area is taken as the theoretical value in the tensile test, the stress value will be approximately 10% higher than in reality. For this reason, taking into account the cross-sectional deviations in the production of the materials used in the study with a 3D printer and calculating the stress according to the actual cross-sectional area will enable us to obtain more accurate results.
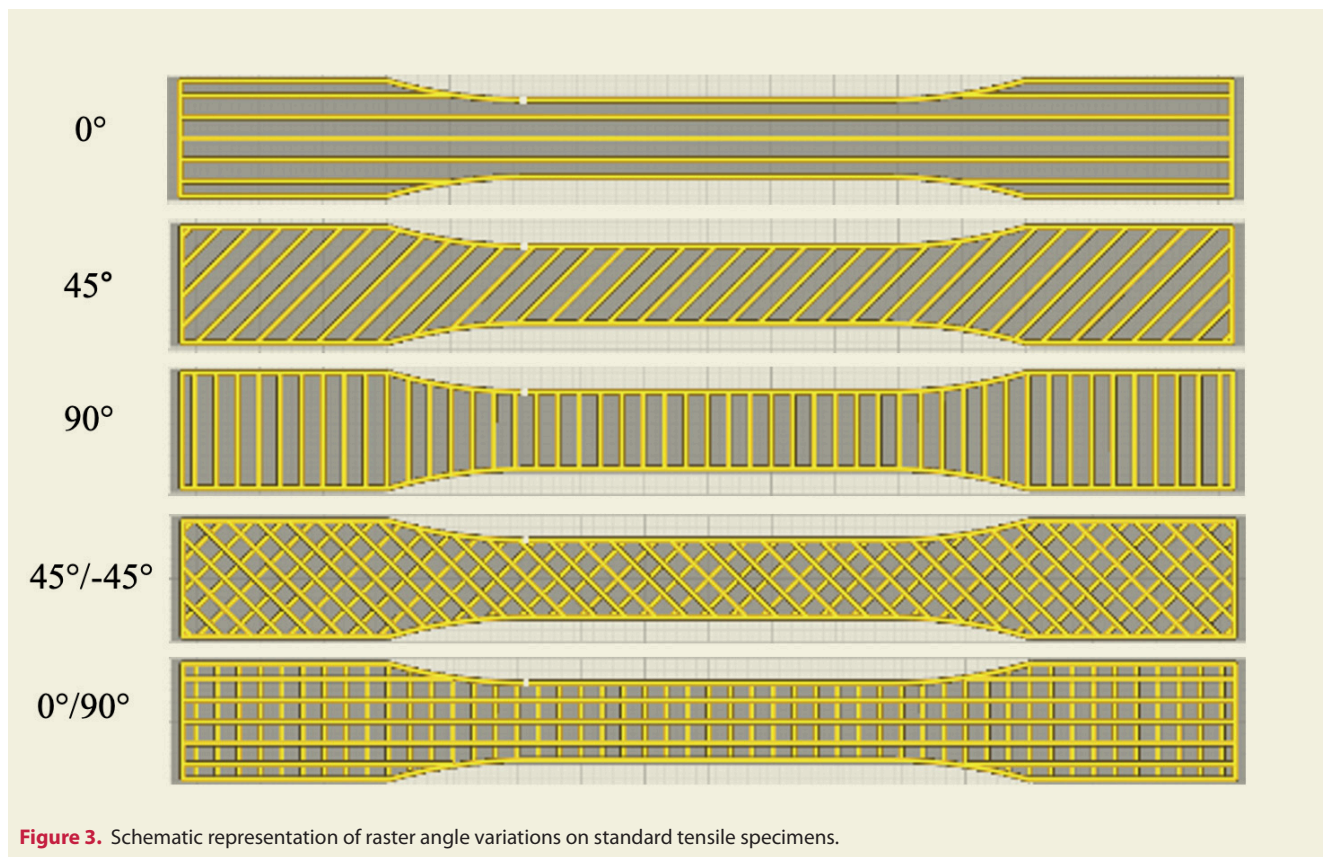

Figure 3. Schematic representation of raster angle variations on standard tensile specimens.

Table 2. Raw results from standard tensile specimens as a result of width (w) and thickness (t) measurements.

| Material	Raster Angle	No	w1 (mm)	w2 (mm)	w3 (mm)	t1 (mm)	t2 (mm)	t3 (mm)
PLA	0°	1	13.14	13.15	13.19	3.41	3.45	3.45
		2	13.15	13.21	13.21	3.51	3.49	3.51
		3	13.15	13.15	13.17	3.44	3.50	3.50
	45°	1	13.08	13.01	13.09	3.53	3.53	3.56
		2	13.10	13.12	13.12	3.57	3.57	3.50
		3	13.13	13.14	13.13	3.55	3.58	3.58
	90°	1	13.12	13.12	13.15	3.51	3.53	3.59
		2	13.13	13.13	13.17	3.52	3.51	3.51
		3	13.19	13.10	13.15	3.54	3.55	3.55
	45°/-45°	1	13.19	13.12	13.19	3.49	3.48	3.5
		2	13.14	13.14	13.16	3.45	3.46	3.46
		3	13.07	13.10	13.12	3.49	3.54	3.49
	0°/90°	1	13.18	13.20	13.19	3.56	3.57	3.57
		2	13.13	13.13	13.20	3.47	3.59	3.56
		3	13.11	13.13	13.18	3.55	3.51	3.55
PETG	0°	1	13.19	13.20	13.21	3.50	3.48	3.51
		2	13.26	13.28	13.29	3.48	3.43	3.49
		3	13.24	13.21	13.29	3.48	3.45	3.49
	45°	1	13.20	13.19	13.19	3.51	3.50	3.59
		2	13.21	13.22	13.32	3.56	3.53	3.5
		3	13.23	13.18	13.21	3.50	3.48	3.52
	90°	1	13.22	13.18	13.28	3.53	3.52	3.51
		2	13.26	13.17	13.22	3.48	3.49	3.48
		3	13.24	13.28	13.26	3.34	3.58	3.54
	45°/-45°	1	13.25	13.27	13.24	3.54	3.49	3.52
		2	13.28	13.22	13.29	3.53	3.55	3.55
		3	13.30	13.26	13.32	3.54	3.50	3.51
	0°/90°	1	13.22	13.18	13.19	3.49	3.51	3.51
		2	13.27	13.19	13.20	3.57	3.55	3.54
		3	13.27	13.29	13.29	3.53	3.54	3.53
ABS	0°	1	13.21	13.28	13.30	3.49	3.50	3.49
		2	13.16	13.19	13.20	3.54	3.59	3.50
		3	13.18	13.19	13.20	3.53	3.53	3.56
	45°	1	13.14	13.22	13.16	3.55	3.54	3.54
		2	13.20	13.11	13.18	3.47	3.49	3.50
		3	13.10	13.14	13.13	3.51	3.57	3.49
	90°	1	13.13	13.08	13.08	3.45	3.49	3.48
		2	13.11	13.17	13.11	3.48	3.53	3.46
		3	13.08	13.13	13.10	3.44	3.45	3.43
	45°/-45°	1	13.18	13.17	13.16	3.51	3.55	3.50
		2	13.22	13.15	13.13	3.50	3.57	3.49
		3	13.16	13.13	13.11	3.49	3.50	3.54
	0°/90°	1	13.18	13.13	13.14	3.48	3.47	3.48
		2	13.17	13.12	13.17	3.45	3.47	3.50
		3	13.19	13.14	13.12	3.52	3.53	3.51
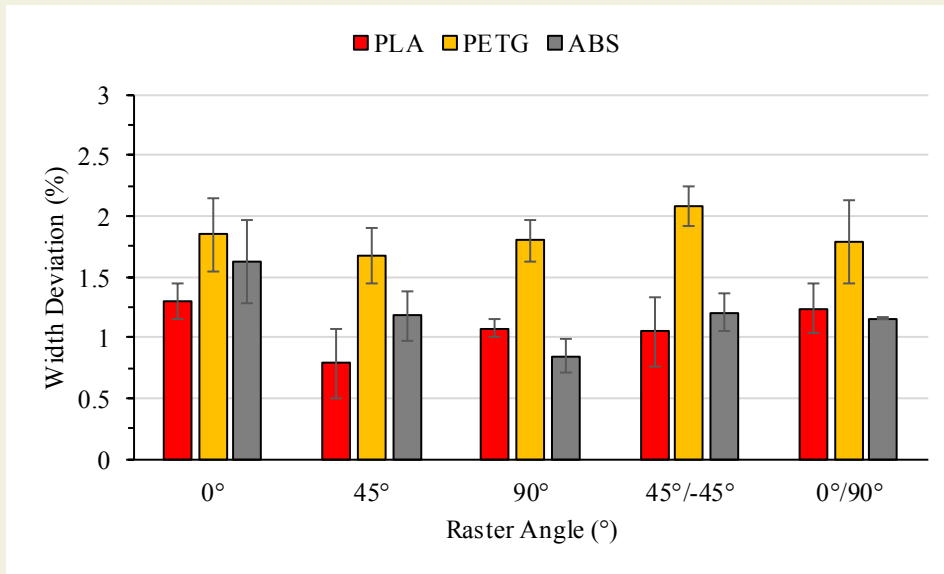
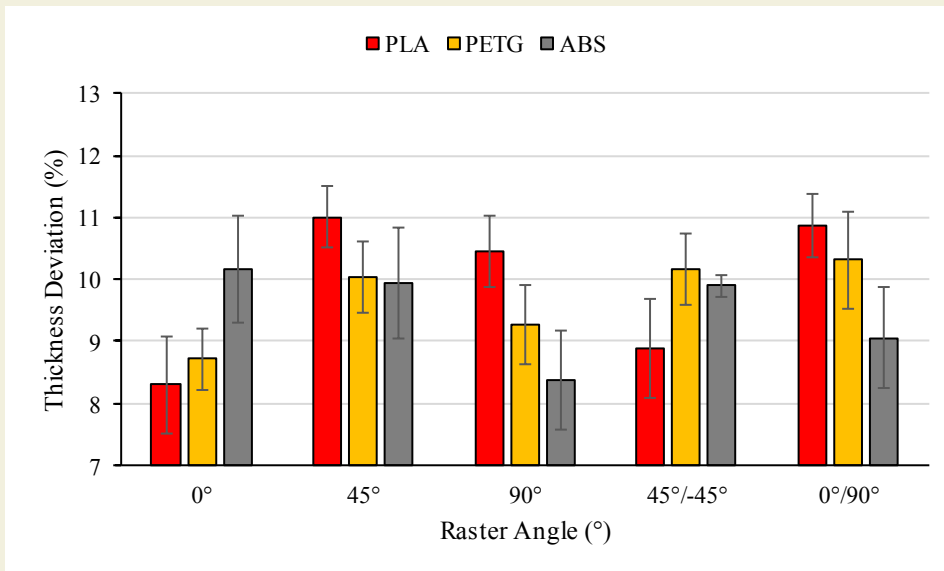**Figure 4.** Width deviation (%) with raster angle (°).

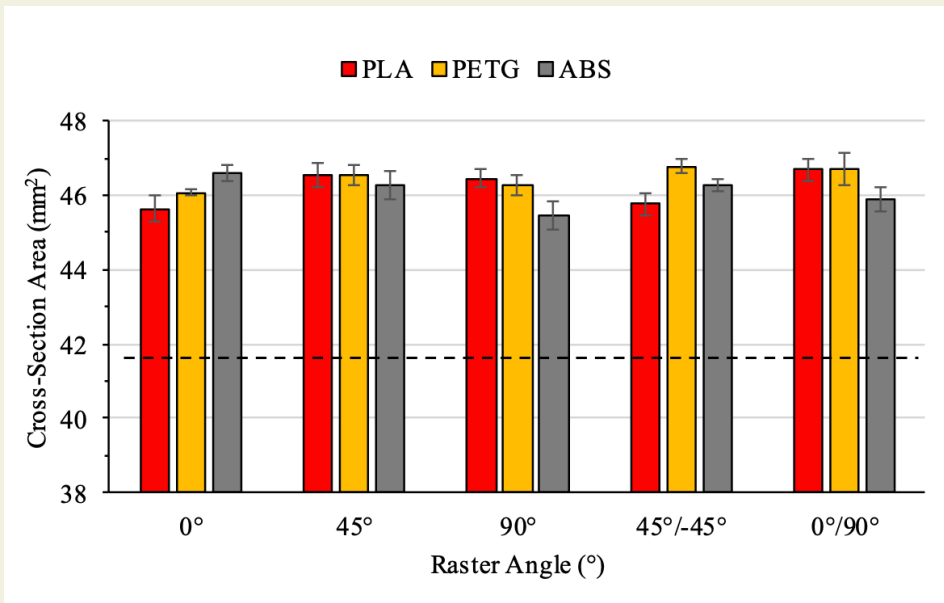**Figure 5.** Thickness deviation (%) with raster angle (°).

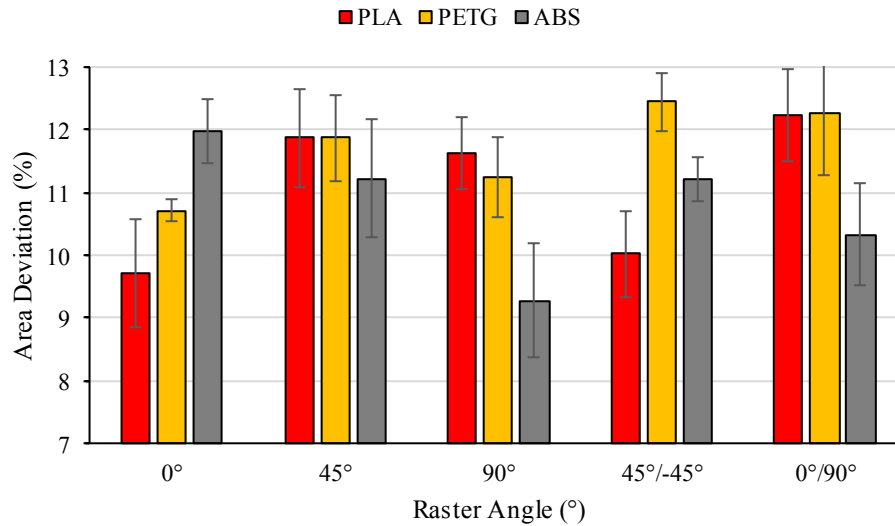**Figure 6.** Variation in the cross-section area (theoretical area: 41.6 mm²) with raster angle (°).

Figure 7. Cross-section area deviation (%) with raster angle (°).

4. Conclusions

In conclusion, the comprehensive analysis of dimensional accuracy in 3D printing, considering different materials (PLA, PETG, and ABS) and raster angles, has provided valuable insights. The following key findings emerge from this study:

- PETG exhibits a higher width deviation than PLA and ABS, indicating differences in dimensional stability. PETG's average width is slightly larger than that of PLA and ABS.

- Raster angle significantly affects width and thickness deviations. Samples with a 90° raster angle generally exhibit lower deviation percentages than 45° or 90° angles. This highlights the importance of selecting an appropriate raster angle for better dimensional accuracy.

- While width deviations remained relatively low (around 2%), thickness deviations were notably higher (around 10%). PETG and PLA show higher levels of thickness deviation, while ABS generally has lower deviations.

- The analysis of cross-sectional areas indicates that, on average, all samples exceed the theoretical area. Percentage deviations in the cross-sectional area generally hover around 11.5 %. PETG at a 45°/-45° raster angle exhibits the largest cross-sectional area, while ABS at a 90° raster angle has the smallest.

In practical terms, understanding the impact of material choice and raster angle on dimensional accuracy is crucial for optimizing 3D printing processes. For applications requiring precise measurements, it is recommended to account for cross-sectional deviations and to calculate the stress based on the actual cross-sectional area rather than the theoretical value to obtain accurate results.

In summary, this study provides valuable data for 3D printing enthusiasts and professionals, offering insights into how material selection and raster angle influence dimensional accuracy. Further research can lead to enhanced printing techniques and improved product quality.

References

[1] Gebisa, A.W., Lemu, H.G., (2019). Influence of 3D printing FDM process parameters on tensile property of ultem 9085. Procedia Manufacturing. 30: 331–8. doi: 10.1016/j.promfg.2019.02.047.

[2] Dawoud, M., Taha, I., Ebeid, S.J., (2016). Mechanical behaviour of ABS: An experimental study using FDM and injection moulding techniques. Journal of Manufacturing Processes. 21: 39–45. doi: 10.1016/j.jmapro.2015.11.002.

[3] Prakash, K.S., Nancharaih, T., Rao, V.V.S., (2018). Additive Manufacturing Techniques in Manufacturing -An Overview. Materials Today: Proceedings. 5(2): 3873–82. doi: 10.1016/j.matpr.2017.11.642.

[4] Kartal, F., Kaptan, A., (2023). Effects of annealing temperature and duration on mechanical properties of PLA plastics produced by 3D Printing 7: 152–9.

[5] Dogan, O., Kamer, M.S., (2023). Experimental investigation of the creep behavior of test specimens manufactured with fused filament fabrication using different manufacturing parameters. Journal of the Faculty of Engineering and Architecture of Gazi University. 38(3): 1839–48. doi: 10.17341/gazimmfd.1122973.

[6] Rajpurohit, S.R., Dave, H.K., (2018). Effect of process parameters on tensile strength of FDM printed PLA part. Rapid Prototyping Journal. 24(8): 1317–24. doi: 10.1108/RPJ-06-2017-0134.

[7] Sheth, S., Taylor, R.M., Adluru, H., (2020). Numerical investigation of stiffness properties of FDM parts as a function of raster orientation. Solid Freeform Fabrication 2017: Proceedings of the 28th

Annual International Solid Freeform Fabrication Symposium - An Additive Manufacturing Conference, SFF 2017.: 1112–20.

[8] Solomon, I.J., Sevvel, P., Gunasekaran, J., (2020). A review on the various processing parameters in FDM. Materials Today: Proceedings. 37(Part 2): 509–14. doi: 10.1016/j.matpr.2020.05.484.

[9] Dogan, O., (2022). Short-term Creep Behaviour of Different Polymers Used in Additive Manufacturing under Different Thermal and Loading Conditions. Strojniski Vestnik/Journal of Mechanical Engineering. 68(7–8): 451–60. doi: 10.5545/sv-jme.2022.191.

[10] Frunzaverde, D., Cojocaru, V., Bacescu, N., Ciubotariu, C.R., Miclosina, C.O., Turiac, R.R., et al., (2023). The Influence of the Layer Height and the Filament Color on the Dimensional Accuracy and the Tensile Strength of FDM-Printed PLA Specimens. Polymers. 15(10). doi: 10.3390/polym15102377.

[11] Bolat, Ç., Eergene, B., (2022). An Investigation on Dimensional Accuracy of 3D Printed PLA, PET-G and ABS Samples with Different Layer Heights. Çukurova Üniversitesi Mühendislik Fakültesi Dergisi. 37(2): 449–58. doi: 10.21605/cukurovaumfd.1146401.

[12] Tezel, T., (2019). FDM ile Üretilen PET-G Malzemenin Üretim Sıcaklığı ve Hızının Boyutsal Doğruluğa Etkisi. International Journal of Multidisciplinary Studies and Innovative Technologies. 3(2): 82–85.

[13] Stojković, J.R., Turudija, R., Vitković, N., Sanfilippo, F., Păcurar, A., Pleşa, A., et al., (2023). An Experimental Study on the Impact of Layer Height and Annealing Parameters on the Tensile Strength and Dimensional Accuracy of FDM 3D Printed Parts. Materials. 16(13): 4574. doi: 10.3390/ma16134574.

[14] Akbaş, O.E., Hıra, O., Hervan, S.Z., Samankan, S., Altınkaynak, A., (2020). Dimensional accuracy of FDM-printed polymer parts. Rapid Prototyping Journal. 26(2): 288–98. doi: 10.1108/RPJ-04-2019-0115.

[15] Mohanty, A., Nag, K.S., Bagal, D.K., Barua, A., Jeet, S., Mahapatra, S.S., et al., (2021). Parametric optimization of parameters affecting dimension precision of FDM printed part using hybrid Taguchi-MARCOS-nature inspired heuristic optimization technique. Materials Today: Proceedings. 50: 893–903. doi: 10.1016/j.matpr.2021.06.216.

[16] Çakan, B.G., (2021). Effects of raster angle on tensile and surface roughness properties of various FDM filaments. Journal of Mechanical Science and Technology, 35(8): 1–7. doi: 10.1007/s12206-021-0708-8.

[17] Tanoto, Y.Y., Anggono, J., Siahaan, I.H., Budiman, W., (2017). The effect of orientation difference in fused deposition modeling of ABS polymer on the processing time, dimension accuracy, and strength. AIP Conference Proceedings. 1788(September 2015). doi: 10.1063/1.4968304.

[18] Kumar, R., Sharma, H., Saran, C., Tripathy, T.S., Sangwan, K.S., Herrmann, C., (2022). A Comparative Study on the Life Cycle Assessment of a 3D Printed Product with PLA, ABS & PETG Materials. Procedia CIRP. 107(March): 15–20. doi: 10.1016/j.procir.2022.04.003.

[19] Bachhav, C.Y., Sonawwanay, P.D., Naik, M., Thakur, D.G., (2023). Experimental and FEA analysis of flexural properties of 3D printed parts. Materials Today: Proceedings. doi: 10.1016/j.matpr.2023.02.262.

[20] Eryıldız, M., (2021). Effect of Build Orientation on Mechanical Behaviour and Build Time of FDM 3D-Printed PLA Parts: An Experimental Investigation. European Mechanical Science. 5(3): 116–20. doi: 10.26701/ems.881254.

Experimental investigation and optimization of the effect garnet vibratory tumbling as a post-process on the surface quality of 3D printed PLA parts

Fuat Kartal[1*], Arslan Kaptan[2]

[1]Kastamonu University, Engineering and Architecture Faculty, Mechanical Engineering Department, Türkiye.
[2]Sivas Cumhuriyet University, Sivas Technical Sciences Vocational School, Motor Vehicles and Transportation Technologies Department, Türkiye.

Orcid: F. Kartal (0000-0002-2567-9705), A. Kaptan (0000-0002-2431-9329)

Abstract: The method known as additive manufacturing causes high surface roughness between layers depending on the technique used at the end of the product development process. This can be an important problem in three-dimensional (3D) manufacturing depending on the usage area. To solve this problem, this experimental study investigated the effect of vibratory rolling (VT) on surface roughness in 3D printed Polylactic Acid (PLA) parts using garnet abrasive particles. Optimization with the best parameters was also performed and the results were analyzed. The surface roughness (Ra) values were measured at different vibration durations for each mesh size. The study involved subjecting the printed parts to vibratory tumbling using garnet abrasive particles of various mesh sizes (80, 90, 100, 120, 150, 180, and 220 mesh). Surface roughness measurements were taken at different vibration durations (2, 4, 6, 8, 10, and 12 hours) for each mesh size. A surface roughness measuring device was used to obtain the roughness values. The findings reveal that vibratory tumbling with garnet abrasive particles effectively reduces surface roughness in 3D printed parts. As the vibration duration increased, smoother surfaces were achieved. The surface roughness of the printed samples was reduced by 60% on average by using the optimum values after post-process.

Keywords: 3D printing, surface roughness, vibratory tumbling, garnet abrasive, additive manufacturing, polylactic acid part.

1. Introduction

Additive Manufacturing (AM), also known as 3D printing, is a revolutionary process that enables the creation of parts layer by layer directly from 3D model data. This method offers advantages over traditional manufacturing processes, mainly when producing complex, customized, or low-volume parts. As a result, AM has gained widespread adoption and significantly impacted various industries, including aerospace, automotive, defense, and healthcare. AM's benefits include advanced customization options, reduced inventory costs, faster delivery times, and less material waste than traditional manufacturing methods. However, one of the significant challenges associated with AM is the need for better surface quality of printed parts. This issue has prompted the development of pretreatment techniques to minimize errors and determine optimal printing parameters [1-5]. Unfortunately, these preprocessing methodologies often have limited effectiveness. Additional finishing techniques, such as surface treatment and machining, are

often necessary to improve AM parts' dimensional and surface quality. Traditional methods like sanding, dremel tools, abrasive blasting, and barrel tumbling have been employed to achieve improved surface finishes. However, these techniques often come at the expense of dimensional accuracy [6]. For precision machining of complex parts, unconventional processes are required. One such process is Abrasive Flow Machining (AFM), which uses a flexible abrasive-based medium to achieve fine finishing of AM parts. AFM provides uniform, predictable, and repeatable results, making it well-suited for finishing complex geometries [7]. It has numerous industrial and material applications. Nevertheless, post-processes also have their limitations. Damage during the post-process can compromise the accuracy of the parts, and the chemicals used in specific processes may pose health risks to operators. To overcome these challenges, one approach is to design AM parts with finishing in mind. Potential issues can be addressed upfront by considering the finishing processes during the part design phase. Furthermore, better integration between AM technologies and

post-processes could unlock additional opportunities for improving the quality of parts. In conclusion, AM holds tremendous potential despite the challenges of achieving high surface quality. Various pre-treatment and post-process techniques can enhance the surface quality of AM parts, making them suitable for a broader range of applications. The integration and better understanding of these techniques are crucial for the continued growth and evolution of AM.

There are studies on optimizing process parameters, improving surface quality, and providing dimensional accuracy in Fused Deposition Modeling (FDM) and other AM processes. Mohamed et al., 2015: This article reviews current research and future perspectives on optimizing FDM process parameters. It discusses various approaches for optimizing process parameters for improved surface quality and dimensional accuracy [8]. Pandey et al., 2003: Authors investigate ladder-like machining method to enhance the surface quality in FDM. They analyze the effect of machining parameters on surface roughness and dimensional accuracy [9]. Sood et al., 2009: This article proposes to use the gray Taguchi method to improve the dimensional accuracy of FDM parts. It explores optimizing process parameters to minimize dimensional errors [10]. Ahn et al., 2009: The authors propose a method for estimating surface roughness in AM processes, including FDM, using measurement data and interpolation techniques [11]. Mohamed et al., 2016: This article focuses on mathematical modeling and optimizing FDM process parameters. They use the Q-optimization design approach to optimize the process parameters using the response surface methodology [12]. Ahn et al., 2009: The authors work on the representation of surface roughness in FDM and propose a model to explain the roughness properties of FDM fabricated surfaces [13]. Ibrahim et al., 2014: This article investigates the effect of process parameters on surface quality and estimating the roughness of FDM-produced surfaces [14]. Reddy et al., 2018: The authors examine the surface texture of FDM parts and analyze the effect of process parameters on surface roughness [15]. Akande, 2015: This article focuses on preferred ability function analysis to optimize the dimensional accuracy and surface quality of FDM parts [16]. Boschetto et al., 2016: This article explores machining using CNC machining to improve the surface quality of FDM parts [17].

Adel et al., 2018: This article evaluates the surface roughness of FDM parts after hot air jet machining and analyzes the effect of the process on the surface roughness [18]. Taufik and Jain, 2017: The authors propose a laser-assisted machining process to improve the surface quality of FDM parts [19]. Lalehpour et al., 2017: This article examines the surface roughness of FDM parts after an acetone steam bath straightening treatment [20]. Galantucci et al., 2009: The authors conducted an experimental study to improve the surface quality of FDM parts [21]. Galantucci et al., 2010: This article quantitatively analyzes a chemical process to reduce the roughness of parts

produced with FDM [22]. Garg et al., 2016: The authors examine the chemical vapor treatment of ABS parts made with FDM and analyze the effect of the treatment on surface quality and mechanical durability [23]. Singh et al., 2017: This article explores improving the surface quality of FDM parts by a steam straightening process [24]. Farbman and McCoy, 2016: Authors guide mechanical design by conducting material tests on 3D-printed ABS and PLA samples [25]. Singh et al., 2019: This article discusses multi-material AM of sustainable, innovative materials and structures involving FDM processes [26]. These references cover a broad knowledge of optimizing process parameters, improving surface quality, and dimensional accuracy in FDM and other AM processes.

When the literature is examined, no study has been found to improve the surface roughness by performing post-processing at different mesh sizes and at different times. In the experimental setup in this study, a vibratory post-processing application was carried out between 80 and 220 mesh and up to 12 hours. In addition, after the optimization process in which the best results were obtained, experimental verification was ensured by manufacturing. Thus, the target of successfully reducing the surface roughness to more acceptable levels has been achieved.

2. Material and Method

In the experimental study, geometries were chosen to represent samples where surface roughness is important. It is aimed to make the results obtained by printing in the parameters most preferred by 3D users more comprehensive. Printing parameters of parts produced from PLA material are seen in Table 1.

Table1. Production parameters of 3D printed parts with PLA material

Parameters	Units	Value
Layer height	(mm)	0.3
Shell thickness	(mm)	1.6
Bottom thickness	(mm)	1.6
Top thickness	(mm)	1.6
Fill density	(%)	20
Print speed	(mm/s)	50
Bed temperature	(°C)	60
Printing temperature	(°C)	220

A vibration tumbler was utilized in this experimental study to investigate the effect of vibratory tumbling (VT) on surface roughness in 3D printing PLA part using garnet abrasive particles (Figure 1.a). The vibration tumbler employed for this research had been specifically designed for this purpose and has been previously described in the literature [27,28]. The vibration tumbler consisted of a bowl or chamber, an electric motor, and an eccentric weight. The abnormal weight was carefully calibrated to provide the desired vibration intensity. A bowl/pool with a capacity of 5 liters (Leegol Electric 5LBs

PG-LG-003) made of steel material was used (Figure 1.b). Garnet abrasive particles with various mesh sizes (80, 90, 100, 120, 150, 180, and 220 mesh) were selected for the experiments. These garnet abrasive particles were commercially available and sourced from reputable suppliers. To perform the VT process, a predetermined amount of 3D printed parts was evenly distributed into the chamber of the vibration drum without using any fluid. The pieces were carefully placed to ensure consistent tumbling conditions. Subsequently, the appropriate garnet abrasive particles were added to the bowl according to the specific mesh size being tested. The VT, with the 3D printed parts and garnet abrasive particles, was operated for a predetermined duration for each experiment (Figure 1.c). The vibration duration varied for each mesh size and was carefully controlled to maintain consistency across the experiments. The duration of the VT process ranged from 0 to 12 hours, with specific time intervals (2, 4, 6, 8, 10, and 12 hours) chosen for measurement purposes. After the VT, the 3D-printed parts were carefully removed from the vibration tumbler for surface roughness measurement (Figure 1.d). Surface roughness (Ra) values were obtained using a surface roughness device (Mitutoyo Surftest SJ-210 Portable Surface Roughness Tester), following standard measurement procedures. The measurements were taken on multiple areas of each part to ensure representative data. The experimental design included ten replicates for each garnet mesh size, resulting in a total of 70 samples tested. The measurements of surface roughness were recorded for further analysis.

3. Results

The experimental results presented in the study demonstrate the effect of VT with garnet abrasive particles on the surface roughness of 3D-printed parts. The roughness measurements were conducted at different time intervals for each mesh size (80, 90, 100, 120, 150, 180, and 220). For the 80 mesh, the initial roughness Ra value was 24.45 μm, consistently decreasing as the vibration duration increased. At the end of the 12-hour vibration period, the roughness Ra value reached 16.8 μm (Figure 2.a). Similarly, for the 90 mesh, the initial roughness Ra value was 24.00 μm, gradually decreasing with longer vibration durations. After 12 hours of vibration, the roughness Ra value fell to 12.00 μm (Figure 2.b). In the case of the 100 mesh, the initial roughness Ra value was 23.8 μm. As the vibration duration increased, the roughness decreased

progressively, reaching a value of 11.2 μm after 12 hours (Figure 2.c). For the 120 mesh, the initial roughness Ra value was 23.2 μm, consistently decreasing with longer vibration durations. At the end of the 12 hours, the roughness Ra value reached 10.0 μm (Figure 2.d). The 150 mesh exhibited an initial roughness Ra value of 22.9 μm. Increasing the vibration duration resulted in a gradual decrease in roughness, with a value of 9.6 μm achieved after 12 hours (Figure 2.e). For the 180 mesh, the initial roughness Ra value was 22.6 μm. The roughness decreased as the vibration duration increased, reaching a value of 9.2 μm after 12 hours (Figure 2.f). Finally, the 220 mesh also displayed an initial roughness Ra value of 22.6 μm. With longer vibration durations, the roughness decreased, reaching a value of 9.2 μm after 12 hours (Figure 2.g). These results highlight the effectiveness of VT with garnet abrasive particles in reducing surface roughness in 3D printed parts. The findings indicate that longer vibration durations lead to smoother surfaces, suggesting optimizing the vibration duration to achieve the desired surface quality. Overall, this study contributes to understanding the relationship between VT and surface roughness in 3D printing, and it emphasizes the potential of this method for improving surface quality in AM applications. Further investigations could explore additional parameters and materials to gain deeper insights into surface roughness in 3D printing processes.

For 80 Mesh, the equation is y = -0.63x + 24.45. This equation represents measurement data for the "80 Mesh" size. The negative slope (-0. 63) indicates that an increase in time results in a decrease in roughness Ra. In other words, as time progresses for this mesh size, roughness Ra decreases, starting at 24.45 μm when time is zero (Figure 2.a). For 90 Mesh, the equation is y = -1.00x + 24.50. This equation also signifies measurement data for "90 Mesh." The negative slope (-1.00) indicates that an increase in time leads to a decrease in roughness Ra, with an initial value of 24.50 (Figure 2.b). For 100 Mesh is represented by the equation y = -1.05x + 24.30. The negative slope (-1.05) suggests that roughness Ra decreases as time increases, with an initial value of 24.30 (Figure 2.c). For 120 Mesh, the equation is y = -1.10x + 23.70, signifying data for "120 Mesh." The negative slope (-1.10) indicates a decrease in roughness Ra with increasing time, starting at 23.70 (Figure 2.d). For 150 Mesh is represented by the equation y = -1.11x + 23.35. The negative slope (-1.11) suggests that roughness Ra decreases with time, with an
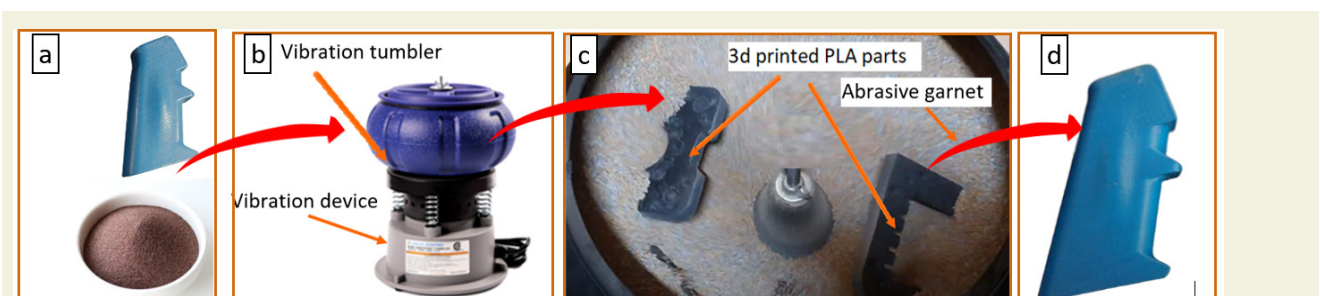

Figure 1. Post-process cycle (a) Garnet abrasive sand and PLA part (b) Experimental setup (c) The vibration tumbler with the 3D-printed parts is in progress (d) Processed part

initial value of 23.35 (Figure 2.e). The equation for 180 Mesh is y = -1.11x + 22.99. This equation represents data for "180 Mesh," and the negative slope (-1.11) indicates that roughness Ra decreases with time, starting at 22.99 (Figure 2.f). Finally, for 220 Mesh, the equation is y = -1.11x + 22.99. This equation represents "220 Mesh" data, and like the others, it has a negative slope (-1.11), indicating a decrease in roughness Ra as time increases, starting at 22.99 (Figure 2.g). All these equations express the linear relationship between time and roughness Ra for each mesh size. The slope reveals how steep or shallow this relationship is, while the intercept represents the initial roughness Ra when time is zero.

Figure 3 displays macro surface roughness views of 3D-printed parts after undergoing VT processes. The figure showcases the surface roughness of parts processed with different mesh sizes and vibration durations. Spe-

cifically, the figure illustrates the surface roughness of parts processed with the following parameters: 80 mesh for 2 hours of vibration (Figure 3.a), 100 mesh for 4 hours of vibration (Figure 3.b),120 mesh for 2 hours of vibration (Figure 3.c), and 220 mesh for 12 hours of vibration (Figure 3.d). The purpose of Figure 3 is to provide a visual representation of the surface roughness achieved for each combination of mesh size and vibration duration. By comparing the macro surface roughness views, one can observe the effects of different processing parameters on the surface quality of 3D-printed parts.

Figure 4 presents macro surface roughness views, comparing untreated 3D-printed parts with those subjected to vibrational tumbling using 80 mesh abrasive particles for different durations, specifically 6 and 12 hours. The untreated parts serve as a baseline reference (control surface), allowing us to assess the impact of the tumbling
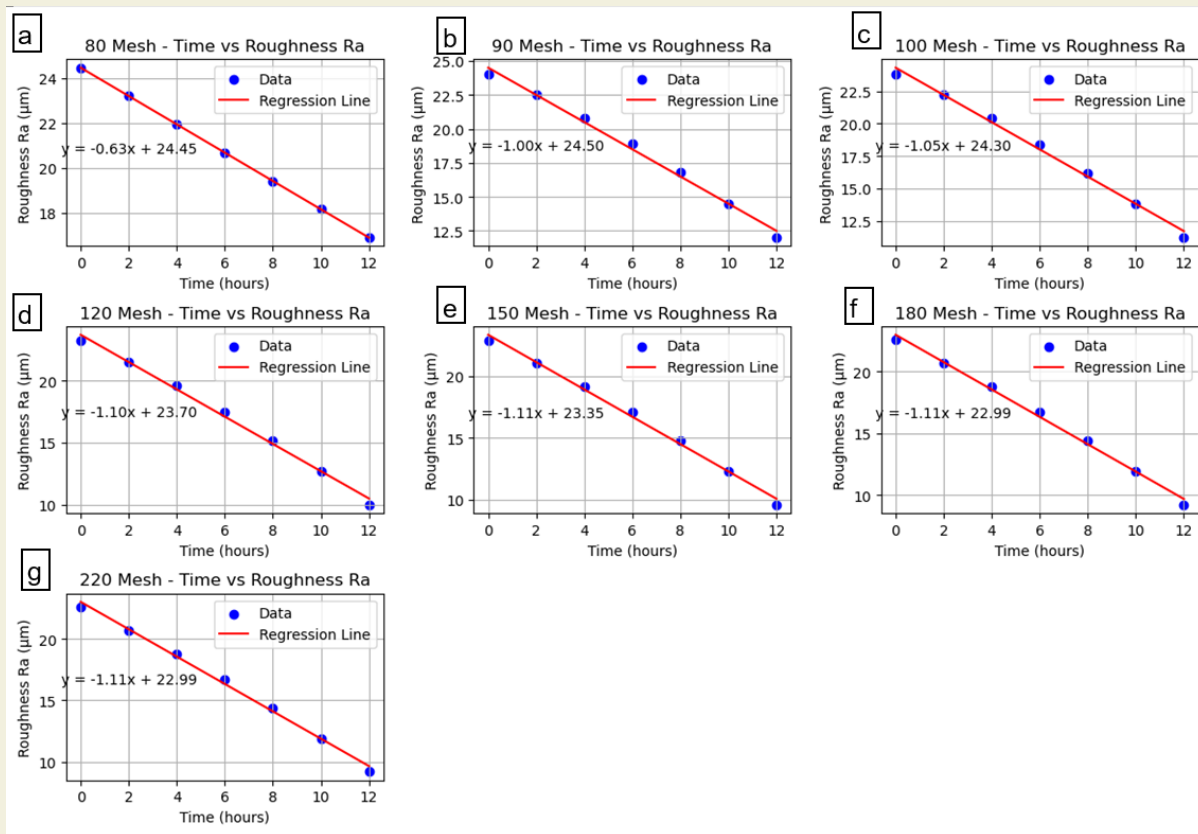

Figure 2. Results for different mesh sizes over various time intervals. (a) 80, (b) 90, (c) 100, (d) 120, (e) 150, (f) 180, and (g) 220 mesh
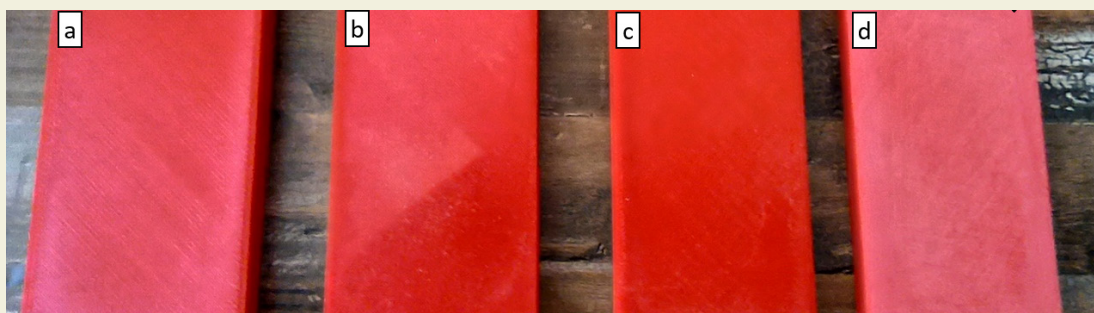

Figure 3. Randomly selected samples of a vibrated tumbler PLA part after the post-process (a) 80 mesh and 2 h, (b) 100 mesh and 4 h, (c) 120 mesh and 2 h, (d) 220 mesh and 12 h.

process on surface roughness (Figure 4.a). The images show clear surface texture and quality differences between the untreated and treated parts. As the tumbling duration increases from 6 to 12 hours, a noticeable improvement in surface smoothness is observed, indicated by a reduction in surface roughness (Figure 4.b and Figure 4.c). The findings underscore the effectiveness of vibrational tumbling with 80 mesh abrasive particles in enhancing the surface quality of 3D printed parts and highlight the importance of optimizing tumbling duration for achieving desired surface characteristics. These results contribute valuable insights for enhancing surface finish in AM applications and emphasize the significance of post-processing methods for improving overall part quality.

Figure 5 shows the optimal mesh sizes and corresponding durations that yield the most favorable surface roughness results in the context of the experimental study. The analysis shows that utilizing 180 mesh abrasive particles combined with a duration of 12 hours in the VT process leads to the lowest average surface roughness values among all evaluated combinations. Thus, it has been determined that the sandblasting process provides an average of 60% improvement in the surface roughness value. This finding underscores the significance of careful mesh size selection and duration optimization to achieve enhanced surface quality in 3D printed parts. Manufacturers can effectively minimize surface roughness by employing the recommended mesh size and duration, ensuring improved overall part quality and reinforcing the relevance of VT as a viable post-processing method in AM applications.

Figure 6 shows a scanning electron microscope (SEM) image of the micro-surface appearance of the 3D-printed parts after undergoing VT. The idea would provide a magnified view of the surface at a micro-scale, allowing for a detailed examination of the surface features and morphology. The SEM image would reveal the effects of
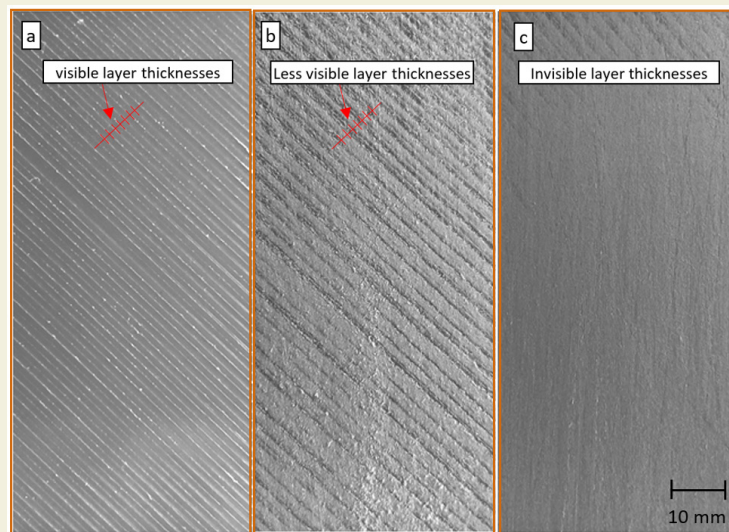

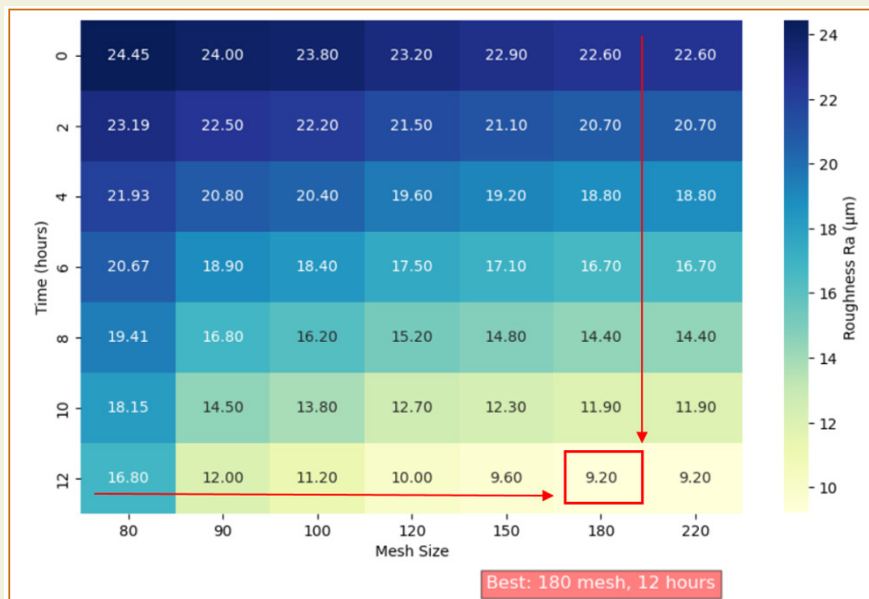**Figure 4.** (a) Control surface (b) 80 mesh 6 h, (c) 80 mesh 12 h.

Figure 5. Optimization of surface roughness Ra (μm) best mesh size and duration

the VT process on the surface of the 3D-printed parts. It may show the removal of layer lines or the presence of smaller-scale roughness features resulting from the tumbling action. The image could also highlight any changes in surface texture, such as smoothing or the formation of new surface structures. The purpose of Figure 6 would be to provide visual evidence and a closer examination of the micro-surface appearance after the VT process. It would aid in understanding the surface modifications and improvements achieved through this post-process method. The SEM images provide a high-resolution view of the microstructure of the surfaces, allowing for a de-

tailed examination of the changes induced by the tumbling process.

Figure 6.a presents a surface roughness appearance of 21.93 µm after 80 mesh and 4 hours of application. Figure 6.b shows the surface roughness of 17.5 µm after 120 mesh and 6 hours of application, and Figure 6.c shows the surface roughness of 9.2 µm after 180 mesh and 12 hours of application. Figure 6.c also gives the SEM image of the surface roughness obtained according to the optimized results. Comparing the photos for each mesh size, distinctive surface features and topography variations can
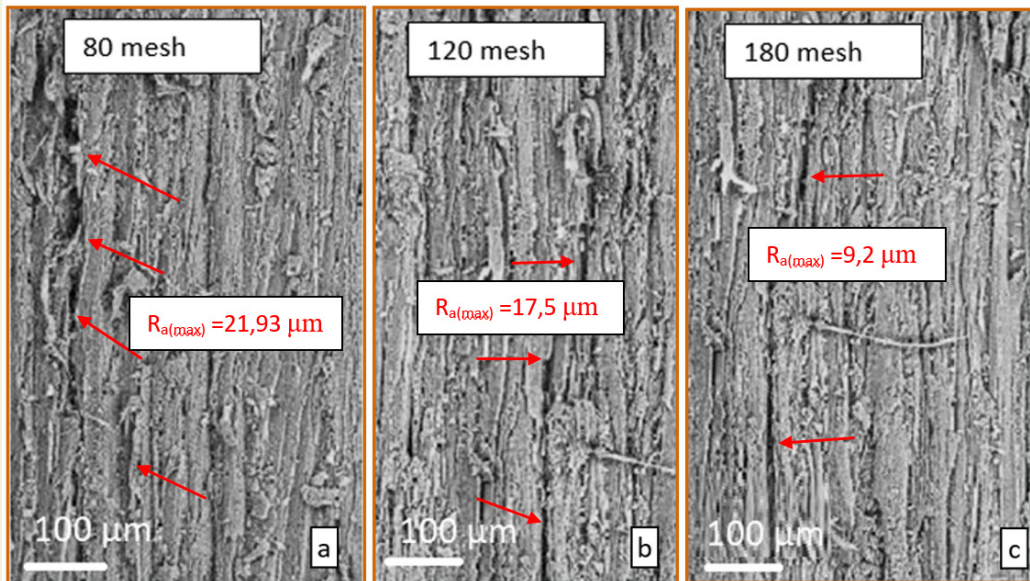

Figure 6. SEM image of the micro-surface of PLA parts. (a) 80 mesh and 4 h, (b) 120 mesh and 6 h, (c) 180 mesh and 12 h.
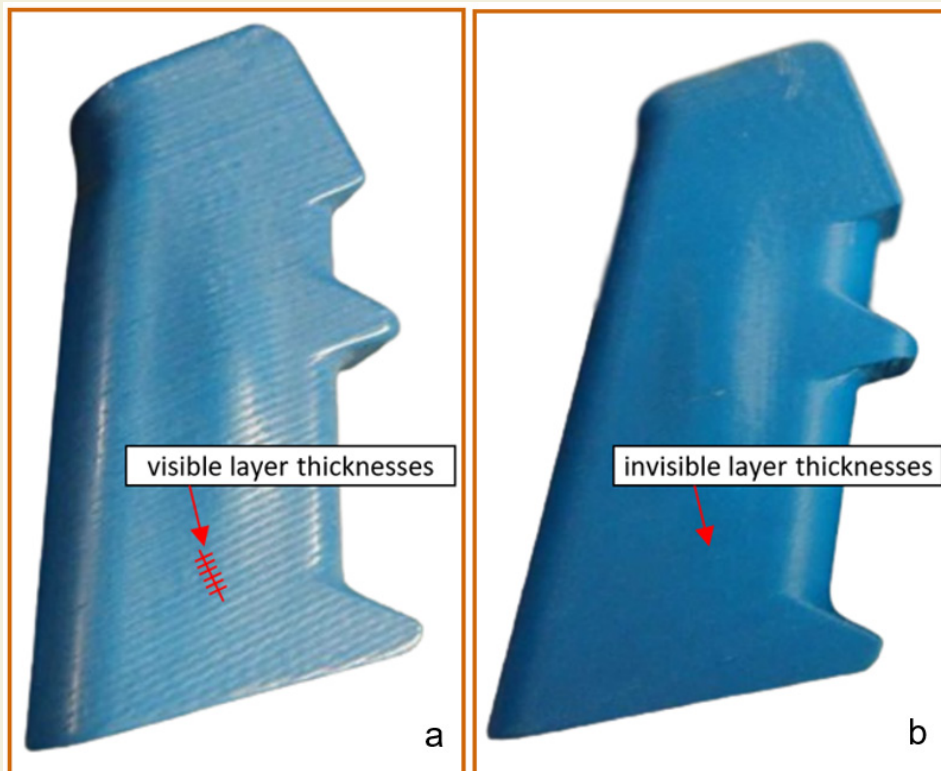

Figure 7. The comparison between 3D printed parts VT with (a) No post-process applied and (b) Post-processed according to optimized parameters.

be observed, revealing the impact of different abrasive particles on the micro-surface characteristics. The SEM images offer valuable insights into the effectiveness of VT with varying mesh sizes, shedding light on how specific mesh sizes influence the microstructural alterations of the 3D-printed parts. This analysis contributes to a comprehensive understanding of the relationship between mesh size and micro-surface quality, further advancing the knowledge of surface enhancement techniques in 3D-printing applications. The SEM images serve as a valuable visual aid, supporting the study's findings and emphasizing the significance of optimizing abrasive particle selection to achieve desired micro-surface properties in AM processes.

Figure 7 shows an example of a 3D-printed gun grip made of PLA material. Figure 7.a shows the no post-processing applied sample, and Figure 7.b shows the same sample as post-processed with optimized parameters. The purpose of this figure is to visually demonstrate the impact of VT on the surface quality of the 3D-printed parts. In image (Figure 7.b), which represents the 3D printed parts after VT with the optimized parameters, the surface appears smoother and more refined compared to the untreated parts in the image (Figure 7.a). The tumbling process using the optimal mesh size and duration has effectively reduced surface roughness, resulting in a more even and polished appearance. Additionally, any visible layer lines or surface defects that may have been present in the untreated parts are less apparent in the vibratory tumbled parts. By comparing both images, it becomes evident that VT with the optimized parameters has significantly improved the surface quality of the 3D-printed parts. This visual representation reinforces the findings presented in the results and discussion sections, highlighting the effectiveness of the VT process in achieving superior surface characteristics and enhancing overall part quality in AM applications.

4. Discussions

The experimental findings presented in this study shed light on the impact of VT with garnet abrasive particles on the surface roughness of 3D-printed parts. The results of roughness measurements conducted at various time intervals for each mesh size (80, 90, 100, 120, 150, 180, and 220 mesh) provide valuable insights into the effectiveness of this post-processing method. The initial roughness Ra values ranged from 24.45 μm to 22.6 μm (Figure 5, first line). They are notably, increasing the vibration time in all mesh sizes from 80 to 220 mesh decreases the surface roughness inversely. At the end of the 12-hour vibration period, the roughness Ra values reached their lowest points, measuring 16.8 μm for 80 mesh, 12.00 μm for 90 mesh, 11.2 μm for 100 mesh, 10.0 μm for 120 mesh, 9.6 μm for 150 mesh, and an impressive 9.2 μm for both 180 mesh and 220 mesh (Figure 5, last line). These findings demonstrate the efficacy of VT with garnet abrasive particles in reducing surface roughness, and they emphasize the importance of optimizing the

vibration duration to achieve the desired surface quality. The graphical representation in Figure 2 further confirms the trend of decreasing roughness Ra values with longer vibration durations. The graphs clearly illustrate that extending the vibration time results in lower roughness Ra values for all mesh sizes, reinforcing the effectiveness of VT in enhancing surface smoothness. Figure 3 provides macro surface roughness views, visually illustrating the surface roughness achieved for different mesh sizes and vibration durations. This visual representation supports the experimental data, providing additional evidence of the positive effects of VT in enhancing surface quality. Comparing macro surface roughness views in Figure 4, it is evident that untreated 3D-printed parts show higher surface roughness than parts subjected to vibrational tumbling with 80 mesh abrasive particles. Notably, increasing the tumbling duration from 6 to 12 hours results in a significant improvement in surface smoothness, highlighting the importance of optimal tumbling time to achieve desired surface characteristics. Finally, Figure 5 illustrates that the optimal mesh sizes and durations yield the most favorable surface roughness results. Utilizing 180 mesh abrasive particles combined with a 12-hour vibration period led to the lowest average surface roughness values among all combinations tested. This finding underscores the importance of careful mesh size selection and duration optimization in achieving enhanced surface quality in 3D printed parts. In Figure 6, the SEM image provides a detailed examination of the micro-surface appearance of 3D-printed parts after undergoing VT. The SEM image reveals the tumbling process's effects on the parts' microstructural properties. The distinct variations in surface topography observed for different mesh sizes underscore the influence of abrasive particle selection on the micro-surface characteristics, further enhancing our understanding of surface enhancement techniques in 3D-printing applications. In conclusion, the results from this experimental study demonstrate the effectiveness of VT with garnet abrasive particles in reducing surface roughness in 3D printed parts. The findings highlight the relationship between vibration duration, mesh size, and surface roughness, indicating the potential of this post-processing method for enhancing surface quality in AM. Further research could explore additional parameters and materials to gain deeper insights into surface roughness in 3D printing processes, contributing to continuous advancements in AM applications.

In addition, the following main inferences can be made about the VT method.

- It is more preferable if it is aimed to improve the surface roughness of the entire part in the sandbox/pool during processing. However, if it is to be used for improvements in the surface roughness on partial areas, it is not necessary to spend time and energy for these surfaces as well. For example, while the surface quality is important for the hand-touched area of a gun's grip, as in Figure 7, the interior of the grip

is not. However, since the whole part is processed in the sandbox, this can be said as the limitation of the VT method.

- In addition, the printed parts are contaminated during use. As a result of the difficulty of cleaning the residues accumulated in the recesses of the rough surfaces, it will cause negative results for terms of health. For this reason, the formation of these deposits on parts with lower surface roughness will become more difficult and it will be easier to clean. Thus, it can be said that VT is a helpful method in achieving antibacterial results.

- On the other hand, during the production of 3D-printed parts, it is inevitable to find burr residues after the parts added to hold the table well or after the support parts, if any, are separated from the main part. In order to remove these burrs from the part, the VT process helps to obtain more effective results in places where it is not very possible to perform burr removal with other methods, especially in narrow areas, depending on the geometry of the part.

- Many finishing methods result in chemical waste or tool wear. However, in the VT method, there are no such wastes or abrasions, and if the PLA particles in the garnet sand are added to the surface, the garnet sand can be cleaned by removing it from the surface due to the density difference. Garnet sand can be re-used as a result of re-drying.

- When many post-process methods are started, they need to wait until they are completed. For example, in surface treatment, the part must be connected, and in order for the processing machine to be used for other works, the part must be disassembled and the machine must be unloaded. However, the sandblasting process not only requires cheap processing equipment, but also allows the process to be kept on hold when desired (or in cases such as power cuts), and then to continue the process from where it was left off.

- Since the sandblasting method in the industrial area is mostly done by spraying the garnet sand on the surface of the part under pressure, it is known that the dust inhaled during this application causes *"silicosis"* disease in the lungs of the operator. Since the VT process is carried out without pressure in a closed pool in the current study, it will not create such a problem. Another advantage of performing the process in a closed environment is that the garnet sand does not scatter around and does not cause environmental pollution.

- Another way to improve the surface roughness of 3D printed parts is to keep the layer thickness value low during the manufacturing phase. However, this will not only increase the printing time but also keep the printers busy, as well as reduce the total lifetime of the printer due to longer working hours. At the same time, there will be long-term energy consumption to keep the nozzle temperature around ~200 °C. By using the VT method as a post-process, larger layer heights can be preferred during the manufacturing phase and economical results can be achieved.

- Another advantage of the method is that a large number of parts can be placed in the sandbox and subjected to an all-in-one surface roughness improvement. If this improvement was tried to be achieved with printer parameters (layer thickness etc.), it would cost long production times for each part separately.

- On the other hand, in cases where different values of surface roughness are needed, some of the parts processed in the same pool can be taken from the sandbox/pool and their processes can be completed. In order for the remaining parts in the sandbox/pool to reach better values, the experiment can be continued by adding the parts that need new processing to the empty places.

5. Conclusions

The experimental findings of this study provide valuable insights into the effectiveness of VT with garnet abrasive particles in reducing surface roughness in 3D-printed parts. The results demonstrate a consistent decrease in roughness Ra values as the vibration duration increases for all mesh sizes investigated. Notably, the optimal mesh size and time combination yielded the lowest average surface roughness values was 180 mesh with a 12-hour vibration period. These results hold significant implications for the AM industry. The reduction in surface roughness achieved through VT can directly impact the overall quality and performance of 3D-printed parts. Smoother surfaces contribute to enhanced aesthetics, improved functionality, and increased longevity of the printed components. As surface roughness is known to influence mechanical properties, wear resistance, and friction characteristics, the findings of this study emphasize the potential of VT as an effective post-processing technique for enhancing part quality in AM.

Based on the experimental results, the following key points can be recommended for conclusions and practical applications:

- *Optimization of Vibration Duration:* The results indicate that longer vibration durations lead to smoother surfaces, as evidenced by decreased roughness Ra values. However, further investigations could explore specific vibration duration ranges for different mesh sizes to identify the ideal duration that maximizes surface quality while minimizing processing time. Fine-tuning the vibration duration can offer an efficient and cost-effective approach to achieving the desired surface finish.

- *Tailoring Mesh Size Selection:* The influence of mesh size on surface roughness was evident in this study, with different mesh sizes resulting in distinct surface characteristics. Further research could explore the relationship between abrasive particle size and its impact on microstructural modifications. Understanding how different mesh sizes affect the surface properties of specific materials can guide material-specific post-processing strategies.

- *Characterization of Mechanical Properties:* While this study focused on surface roughness as a primary measure of surface quality, future investigations could explore the relationship between surface roughness and mechanical properties, such as tensile strength, hardness, and fatigue resistance. This comprehensive approach will provide a more holistic understanding of the influence of VT on part performance.

- *Alternative Abrasive Particles and Materials:* Exploring the efficacy of different abrasive particles and materials in the VT process may offer new insights into surface enhancement techniques. Investigating materials with varying hardness and particle size distributions can better understand how different materials interact with 3D-printed parts during tumbling.

- *Process Integration and Automation:* As the AM industry advances, streamlining post-processing techniques, including VT, becomes essential for scalability and efficiency. Integrating VT into automated post-processing systems can further enhance the reproducibility and consistency of surface post-process results.

In conclusion, the results of this study highlight the potential of VT as a viable post-processing method for reducing surface roughness in 3D-printed parts. The findings contribute to understanding the relationship between VT parameters and surface quality in AM. Manufacturers can achieve smoother surfaces and improved part performance by optimizing vibration duration and mesh size selection. These insights are valuable for researchers and practitioners seeking to enhance the surface quality of 3D printed components and advance the capabilities of AM technologies.

Acknowledgements

References

[1] Zhang, X., & Chen, L. (2020). Effects of laser scanning speed on surface roughness and mechanical properties of aluminum/Polylactic Acid (Al/PLA) composites parts fabricated by fused deposition modeling. Polymer Testing, 91, 106785. DOI: 10.1016/j.polymertesting.2020.106785.

[2] Dizon, J. R. C., Gache, C. C. L., Cascolan, H. M. S., Cancino, L. T., & Advincula, R. C. (2021). Post-processing of 3D-printed polymers. Technologies, 9(3), 61. DOI: 10.3390/technologies9030061.

[3] Kartal, F., & Kaptan, A. (2023). Investigating the Effect of Nozzle Diameter on Tensile Strength in 3D-Printed PLA Parts. Black Sea Journal of Engineering and Science, 6(3), 276-287. DOI: 10.34248/bsengineering.1287141.

[4] Özsoy, K., & Aksoy, B. (2022). Real-time data analysis with artificial intelligence in parts manufactured by FDM printer using image processing method. Journal of Testing and Evaluation, 50(1), 629-645. DOI: 10.1520/jte20210125

[5] Duman, B., & Özsoy, K. (2021). Toz yatak füzyon birleştirme eklemeli imalatta kusur tespiti için öğrenme aktarımı kullanan derin öğrenme tabanlı bir yaklaşım. Gazi Üniversitesi Mühendislik Mimarlık Fakültesi Dergisi, 37(1), 361-376. DOI: 10.17341/gazimmfd.870436

[6] Moradi, M., Karami Moghadam, M., Shamsborhan, M., Bodaghi, M., & Falavandi, H. (2020). Post-processing of FDM 3D-printed polylactic acid parts by laser beam cutting. Polymers, 12(3), 550. DOI: 10.3390/polym12030550.

[7] Dixit, N., Sharma, V., & Kumar, P. (2022). Experimental investigations into abrasive flow machining (AFM) of 3D printed ABS and PLA parts. Rapid Prototyping Journal, 28(1), 161-174. DOI: 10.1108/RPJ-01-2021-0013.

[8] Mohamed O A, Masood S H, and Bhowmik J.L. (2015). Optimization of fused deposition modeling process parameters: a review of current research and prospects. Advances in Manufacturing, 3, 42-53. DOI: 10.1007/s40436-014-0097-7.

[9] Pandey P, Venkata Reddy N, and Dhande S. (2003). Improvement of surface finish by staircase machining in fused deposition modeling. J. Mater. Process. Technol., 132, 323-331. DOI: 10.1016/S0924-0136(02)00953-6.

[10] Sood A, Ohdar R, and Mahapatra S. (2009). Improving dimensional accuracy of Fused Deposition Modelling processed part using grey Taguchi method. Mater. Des., 30, 4243-4252. DOI: 10.1016/j.matdes.2009.04.030.

[11] Ahn D, Kim H, and Lee S. (2009). Surface roughness prediction using measured data and interpolation in layered manufacturing. J. Mater. Process. Technol., 209, 664-671. DOI: 10.1016/j.jmatprotec.2008.02.050.

[12] Mohamed O, Masood S, and Bhowmik J. (2016). Mathematical modeling and FDM process parameters optimization using response surface methodology based on Q-optimal design. Appl. Math. Modell., 40, 10052-10073. DOI: 10.1016/j.apm.2016.06.055.

[13] Ahn D, Kweon J, Kwon S, Song J, and Lee S. (2009). Representation of surface roughness in fused deposition modeling. J. Mater. Process. Technol., 209, 5593-5600. DOI: 10.1016/j.jmatprotec.2009.05.016.

[14] Ibrahim D, Ding S, and Sun S. (2014). Roughness Prediction for FDM Produced Surfaces. International Conference Recent Trends in Engineering & Technology, pp. 70-74.

[15] Reddy V, Flys O, Chaparral A, Berrimi C, A V, and Rosen B.

(2018). Study on the surface texture of Fused Deposition Modeling. Procedia Manufacturing, 25, 389-396. DOI: 10.1016/j.promfg.2018.06.108.

[16] Akande S O. (2015). Dimensional accuracy and surface finish optimization of fused deposition modeling parts using desirability function analysis. International Journal of Engineering Research and Technology, 4. DOI: 10.17577/IJERTV4IS040393.

[17] Boschetto A, Bottini L, and Veniali F. (2016). Finishing of fused deposition modeling parts by CNC machining. Rob. Comput. Integr. Manuf., 41, 92-101. DOI: 10.1016/j.rcim.2016.03.004.

[18] Adel M, Abdelaal O, Gad A, Nasr A, and Khalil A. (2018). Polishing of fused deposition modeling products by hot air jet: evaluation of surface roughness. J. Mater. Process. Technol., 251, 73-82. DOI: 10.1016/j.jmatprotec.2017.07.019.

[19] Taufik M, and Jain P. (2017). Laser-assisted finishing process for improved surface finish of fused deposition modeled parts. J. Manuf. Processes, 30, 161-177. DOI: 10.1016/j.jmapro.2017.09.020.

[20] Lalehpour A, Janeteas C, and Barari A. (2017). Surface roughness of FDM parts after post-processing with acetone vapor bath smoothing process. The International Journal of Advanced Manufacturing Technology, 95, 1505-1520. DOI: 10.1007/s00170-017-1165-5.

[21] Galantucci L, Lavecchia F, and Percoco G. (2009). Experimental study aiming to enhance the surface finish of fused deposition modeled parts. CIRP Ann., 58, 189-192. DOI: 10.1016/j.cirp.2009.03.071.

[22] Galantucci L, Lavecchia F, and Percoco G. (2010). Quantitative analysis of a chemical treatment to reduce the roughness of parts fabricated using fused deposition modeling. CIRP Ann.,

59, 247-250. DOI: 10.1016/j.cirp.2010.03.074.

[23] Garg A, Bhattacharya A, and Batish A. (2016). Chemical vapor treatment of ABS parts built by FDM: Analysis of surface finish and mechanical strength. The International Journal of Advanced Manufacturing Technology, 89, 2175-2191. DOI: 10.1007/s00170-016-9257-1.

[24] Singh R, Singh S, Singh I, Fabbrocino F, and Fraternali F. (2017). Investigation for surface finish improvement of FDM parts by vapor smoothing process. Composites Part B: Engineering, 111, 228-234. DOI: 10.1016/j.compositesb.2016.11.062.

[25] Farbman D, and McCoy C. (2016). Materials testing of 3D printed ABS and PLA samples to guide mechanical design. Materials; Biomanufacturing; Properties, Applications, and Systems; Sustainable Manufacturing, 2, MSEC2016-8668, V002T01A015. DOI: 10.1115/MSEC2016-8668.

[26] Singh R, Kumar R, Farina I, Colangelo F, Feo L, and Fraternali F. (2019). Multi-material additive manufacturing of sustainable, innovative materials and structures. Polymers, 11, 62. DOI: 10.3390/polym11010062.

[27] Pei, E., Nsengimana, J., & Van Der Walt, J. G. (2021). Improvement of Surface Finish for Additive Manufactured Parts-A Comparison Study of Six Post Processing Techniques. Brunel University Research Archive (BURA), London.

[28] Kumbhar, N. N., & Mulay, A. V. (2018). Post processing methods used to improve surface finish of products which are manufactured by additive manufacturing technologies: a review. Journal of The Institution of Engineers (India): Series C, 99, 481-487. DOI: 10.1007/s40032-016-0340-z.

Effect of chemical oxidation process on adhesive performance in two component adhesive with nano particle and filament additives

İclal Avinç Akpınar[1*]

[1]Office of Occupational Health and Safety, Erzurum Technical University, 25050 Erzurum, Türkiye.

Orcid: İ. Avinc Akpinar (0000-0001-9994-6733)

Abstract: Adhesive, which is defined as the substance that binds the same or different types of materials together, is used in almost all sectors. However, the use of composite materials in the automotive, aerospace and aviation sectors due to their lightness and durability increases the importance of adhesive and adhesive joints. Adding nanostructures to the adhesive is a popular method today to improve the performance of the adhesive. However, homogeneous dispersion of nanoparticles added to the adhesive and increasing the wettability of nanofibers are very important in terms of adhesive performance. In the present study, chemically surface-treated nanoparticles and nanofibers were added to the adhesive to improve the performance of the two-component structural adhesive. In the study, DP460 structural adhesive was used as adhesive, functionalized Multi Walled Carbon Nanotubes (MWCNT-COOH) with COOH and carbon fiber (CF) chemically surface treated with HNO_3 solution were used as nanostructures. In the experimental study, eight different parameters were investigated as the nanostructure was (i) undoped, (ii) 1 wt% MWCNT-COOH added, (iii) 1wt%. untreated CF added, (iv) 0.5 wt% chemically treated CF added, (v) 1 wt% chemically treated CF added, (vi) 2 wt% chemically treated CF added, (vii) 0.5 wt% MWCNT-COOH and 0.5 wt% chemically treated CF added, and (viii) 1 wt% MWCNT-COOH and 1wt% chemically treated CF added. According to the results of the study, adding nanoparticles to the adhesive increases the performance of the adhesive by about 12%, while adding nanofibers increases the performance of the adhesive by about 18%. In addition, increasing the inertness and wettability of nanofibers by chemical treatment, as well as the use of nanoparticles and fibers together, significantly increases the performance of the adhesive. In addition, the obtained results were supported by fourier transform infrared spectroscopy (FT-IR) analysis and scanning electron microscopic (SEM) analysis.

Keywords: Polymer composites, Adhesive, Chemical oxidation, Carbon fiber, Nano particle, Strength.

1. Introduction

The use of composite materials in the automotive, aerospace and aviation sectors due to their lightness and durability increases the importance of adhesive and adhesive joints day by day. Adhesive joints; it offers important advantages in terms of not causing any change in the crystal structure as a result of melting, not forming stress concentrations, performing the joining process under melting temperatures, and also obtaining smoother and cleaner surfaces as in traditional joint methods [1].

There are important factors to improve the performance of adhesive joints. The first of these is to increase the force of attraction that exists between two different materials, which makes these two materials bond together. In order for these forces, also known as adhesion forces, to be strong, the adhesive must penetrate the roughness on the material surface and wet the entire surface. The second important factor is the cohesive force of attraction be-

tween the adhesive molecules, which keeps the adhesive together. The greater the covalent bond strengths that allow the polymer molecules to hold together, the greater the performance of the adhesive [2]. When the studies aimed at increasing these covalent bond strengths are examined, the addition of nanostructures to the adhesive comes into consideration. These studies were generally examined under the title of polymeric composites and they were named as "nano composites" because they contain nanostructures. The chemical and mechanical bonding between the nanostructure and the polymer is the main reason for the improvement in the mechanical properties of the polymer and the bond. Studies have shown that carbon nanostructures that do not have surface groups also improve the mechanical properties of the polymer [3].

The nanostructure added to the adhesive to improve the performance of the adhesive was generally carbon nano-

tube (CNT) and carbon black samples. In a study published by Park et al. [4], the epoxy adhesive used in glass/epoxy composite bonds was modified with carbon black. The results indicate that carbon black reinforcement reduces the thermal expansion coefficient of the adhesive and sufficiently increases the load bearing capacity of the joint. In addition, Sihn et al. [5] concluded that the nano-composite adhesive obtained by adding CNT to the adhesive increases the thermal conductivity of the adhesive joint. However, in modifying the epoxy adhesive with CNT, the ratio of CNT addition is an important parameter in terms of bond strength. Hsiao et al. [6] conducted a study on this subject and stated that there was a direct correlation between the CNT additive ratio and the bond strength as a result of the study.

Another non-structure added to the adhesive to increase the performance of the adhesive is filament structures. The performance of adhesives with filament structure additives is better than adhesives with nano particle additives. However, the most important disadvantage of adhesives with filament structure additives is the poor possibility of wettability with epoxy due to the chemical inertness of the filament structures added to the adhesive. This affects the performance of the adhesive. Therefore, in order to remove the chemical inertness of the filament structure and thus increase its wettability, the filament structures must be subjected to chemical surface treatments. In a study by Tiwari et al. [7], chemical surface treatment with nitric acid (oxidation with nitric acid) was applied to carbon filaments at different times (15-180 minutes) and the performances of these samples were investigated. According to the results of the study, the load carrying capacity of the filaments under tension decreased by 40% after 180 minutes of oxidation, and the best performance in terms of adhesive performance was obtained with 90 minutes of oxidation with nitric acid. In a study by Lou et al. [8], three different methods (ultrasonic surface cleaning, nitric acid oxidation and combination of ultrasonic and nitric acid oxidation) were applied to treat the surface of carbon filaments added to epoxy. In terms of the performance of the composite, they stated that the most suitable method among these applied methods is the method in which ultrasonic and nitric acid oxidation are applied together.

It is understood from the literature research that the addition of CNT and CF to the adhesive is very important for the performance of the adhesive. However, the rate of addition of CF to the adhesive, the homogeneous distribution of CNT to the epoxy and the removal of chemical inertness of CF affect the adhesive performance. In addition, the effect of using these two nanostructures together on the performance of the adhesive has not been examined. In the presented study, chemically surface-treated nanoparticles and filaments were added to the epoxy part to improve the performance of the two-component (epoxy and hardener) structural adhesive. In the study, DP460 structural adhesive was used as adhesive, functionalized Multi Walled Carbon

Nanotubes (MWCNT-COOH) with COOH and carbon filament (CF) chemically surface treated with HNO_3 solution were used as nanostructures. In the experimental study, eight different parameters were investigated as the nanostructure was (i) undoped, (ii) 1 wt% MWCNT-COOH added, (iii) 1wt%. untreated CF added, (iv) 0.5 wt% chemically treated CF added, (v) 1 wt% chemically treated CF added, (vi) 2 wt% chemically treated CF added, (vii) 0.5 wt% MWCNT-COOH and 0.5 wt% chemically treated CF added, and (viii) 1 wt% MWCNT-COOH and 1wt% chemically treated CF added. In addition, the experimental results were compared with the results of fourier transform infrared spectroscopy (FT-IR) analysis and scanning electron microscopic (SEM) analysis.

2. Material and method

In the presented study, a two-component (epoxy-hardener) DP460 (manufactured by 3M Company, St. Paul, MN, USA) structural adhesive, which is frequently used in aerospace and automotive fields, was used as the bonding material. The ratio of epoxy hardener in two-component adhesive is 2:1. The curing of this structural adhesive varies depending on temperature and time. After 30 minutes at 24^0C, the epoxy and hardener react and begin to cure. The adhesive was completely cured by keeping it at 70^0C for 120 minutes. In addition, nanostructures added into the adhesive are COOH-functionalized Multi Walled Carbon Nanotubes (outside diameter 10 to 20 nm, length 10 to 30 mm, purity 96%, surface area 200 m2/g) and 5 mm long trimmed 3K Carbon Fiber (fiber thickness : 0.22 mm, weight: 200 gr/m2, warp / scarf: 215/215 tex, weaving type: plain, filament thickness: 70μm). These nanostructures were purchased from Graphene Chemical Industry (Turkey). Mechanical properties for the adhesive and nanostructures used in experimental studies are given in Table 1.

Table 1. Material properties of the adhesive and carbon fiber [9].

	DP 460	Carbon Fiber
E (MPa)	2044 $^{±47}$	228000 $^{±2500}$
ν	0.38	-
σ_t (MPa)	44.6 $^{±1.2}$	3800 $^{±350}$
ε_t (%)	4.2	1.9

E:Young's modulus; ν: Poisson's ratio; σ_t : Ultimate tensile strength; σ_t : Ultimate tensile strain

Approximately 5 g of adhesive is required to prepare a standard bulk sample of adhesive. Since 3 samples will be produced from each parameter in the study, 15 g of adhesive was taken into account. Considering this situation, for the preparation of Multi Walled Carbon Nanotubes-COOH (MWCNT-COOH) nanostructure additive, 10 grams of epoxy and adhesive amount (15 g) of 1 wt% (0.15 g) of nanostructure was added to an empty beaker with the help of precision balance (Figure 1 a).). Then, acetone was added to the same beaker, approximately twice the amount of epoxy, and mixed in an ultrasonic mixer at a frequency of 30 KHz for 20 minutes

(Figures b and c). The aim here is to increase the distance between nanoparticles and to ensure homogeneous dispersion of the nanostructure in the adhesive. The beaker containing epoxy, MWCNT-COOH and acetone was kept at 50°C and the acetone evaporated. Whether the acetone evaporated completely or not was checked with a precision balance. Then, 5 g of hardener was added to the mixture and mixed by hand for 10 minutes. This method was first applied in a project made within the scope of Tübitak 1001 [10].

In the presented study, two different CFs were used for the Carbon filament (CF) added adhesive. These are chemically surface-treated CF and acetone-washed CF. In the chemical surface treatment of CF, 65% pure HNO_3 solution was used. The carbon filament fabric shown in Figure 2 a was kept in HNO_3 solution at 100°C for 60 minutes and then washed with distilled water. The filament fabric washed with pure water was dried in drying-oven at 120°C for 120 minutes (Figure 2 b). In the preparation of CF washed with acetone, carbon filament fabric was soaked in acetone of 95% purity for 10 minutes. Afterwards, the filaments were separated from the fiber fabric and cut into 5 mm length with scissors and trimmed filaments were obtained (Figure 2 c). The method used in the addition of the MWCNT-COOH nano-

structure was applied to the attachment of the filaments to the adhesive.

In the production of bulk samples with or without nanostructure additives, a mold covered with non-stick tape was used to adjust the thickness and dimensions (Figure 3). Prepared adhesive is poured into this mold and flattened in the mold with the help of a gauge. The curing conditions of the adhesive were provided by placing the mold in the hot press. After curing was complete, the adhesive was removed from the mold (Figure 3).

Bulk sheets obtained from adhesives were cut to ISO 2818 [11] sample sizes given in Figure 4 a (Figure 4b) and gauge length was drawn on the sample to obtain more precise displacement data with video extensometer during testing (Figure 4 c).

In the present study, chemically surface-treated filaments and nanoparticles were added to the epoxy part to improve the performance of two-component DP460 structural adhesive. The shear strength of the produced nanostructured composite adhesives was investigated under the tensile test. The parameters used in the experimental study are given in Table 2 and 3 samples were produced from each parameter.
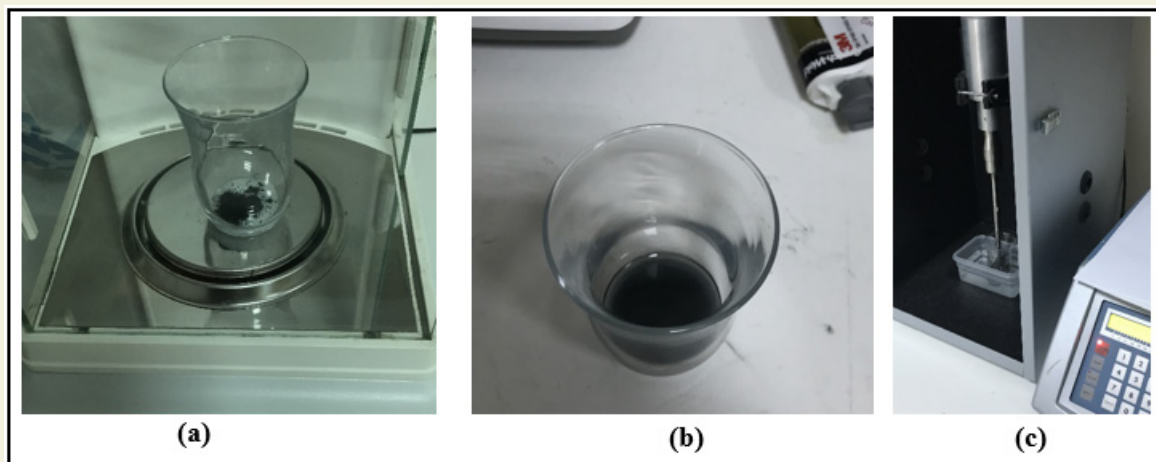

Figure 1. a) Addition of epoxy and MWCNT-COOH, b) Addition of acetone to the mixture, c) Ultrasonic mixer.
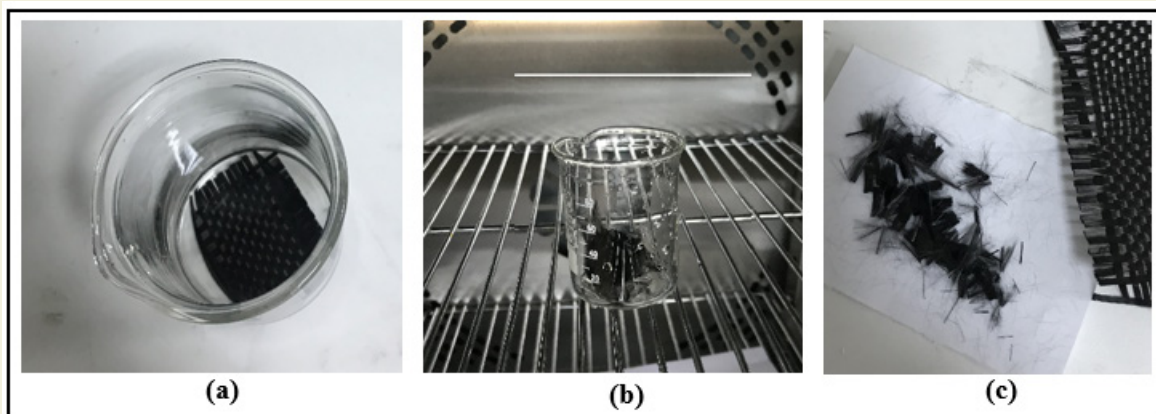

Figure 2. a) Fiber fabric in HNO_3 solution, b) drying of fiber fabric in drying-oven, c) 5 mm long CF.

The tensile test of the adhesive joints was carried out on a computer-controlled Instron-5982 (USA) universal tensile device at a tensile speed of 1 mm/min (Figure 5). The tensile test procedure applied to adhesive joints is given in Figure 5. In addition, tensile tests of a total of 24 bulk samples, three from the configuration given in Table 3, were carried out and the average shear stress and strain of the adhesives were obtained.

Fourier Transform Infrared Spectroscopy (FT-IR) analysis was performed to examine the chemical nature and interaction of nanostructured and undoped adhesives.

Table 2. Parameters used in the experimental study.

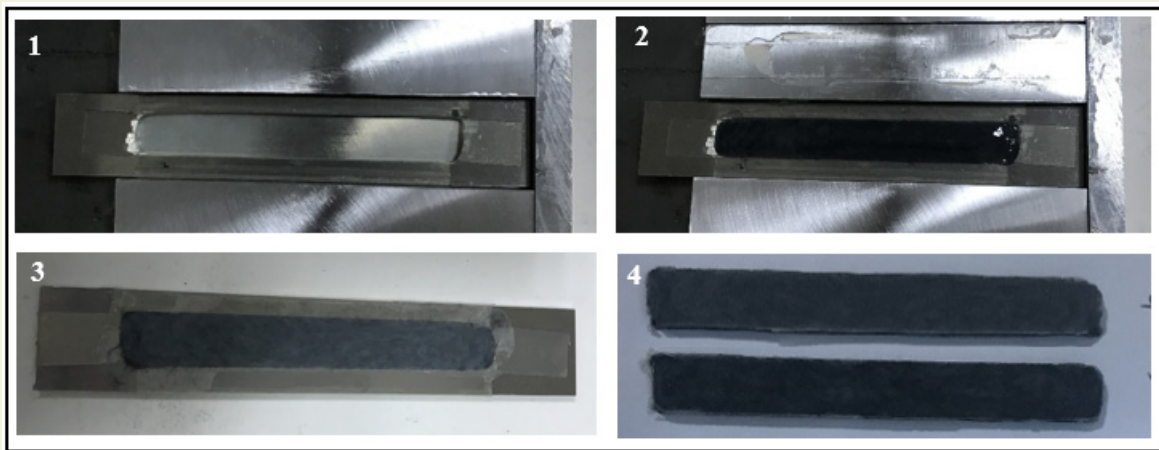| Samples	Chemical surface treatment for fiber	nanostructure	wt % nanostructure ratio
A-1	-------	--------	--------
A-2	-------	MWCNT-COOH	1
A-3	-------	CF	1
A-4	HNO_3	CF	0.5
A-5	HNO_3	CF	1
A-6	HNO_3	CF	2
A-7	HNO_3	wt % 0.5 MWCNT-COOH + wt % 0.5 CF	1
A-8	HNO_3	wt % 1 MWCNT-COOH + wt % 1 CF	2

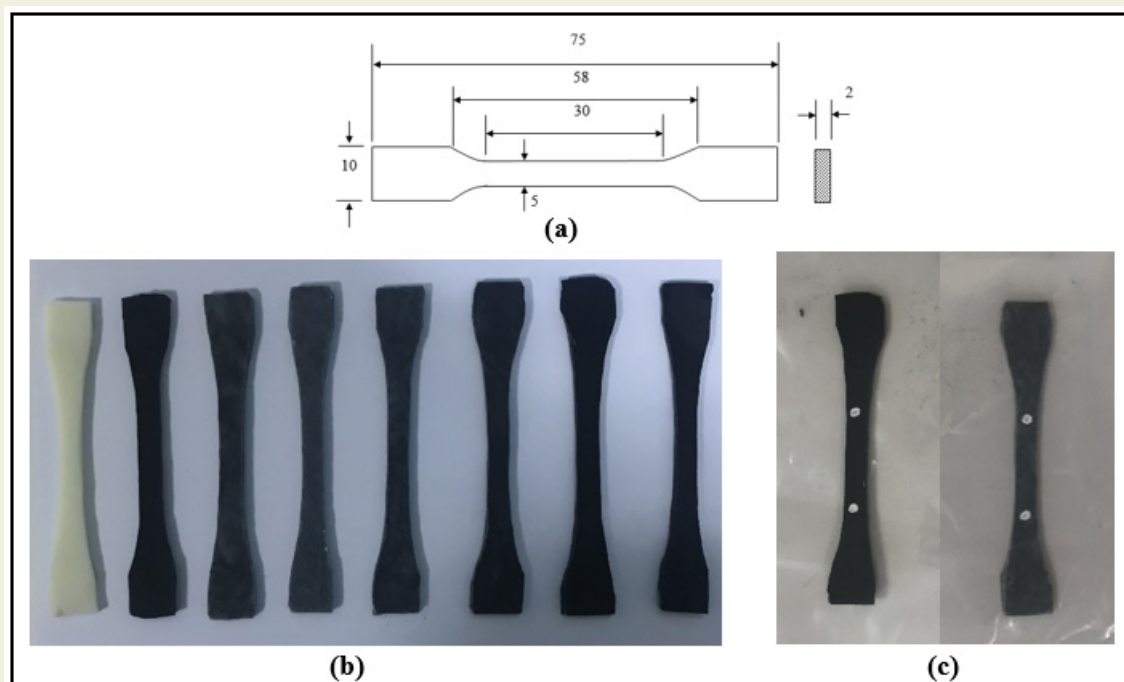**Figure 3.** Bulk adhesive production scheme.

Figure 4. a) Standard bulk sample sizes, b) produced bulk sample samples, c) gauge length marking on the sample.
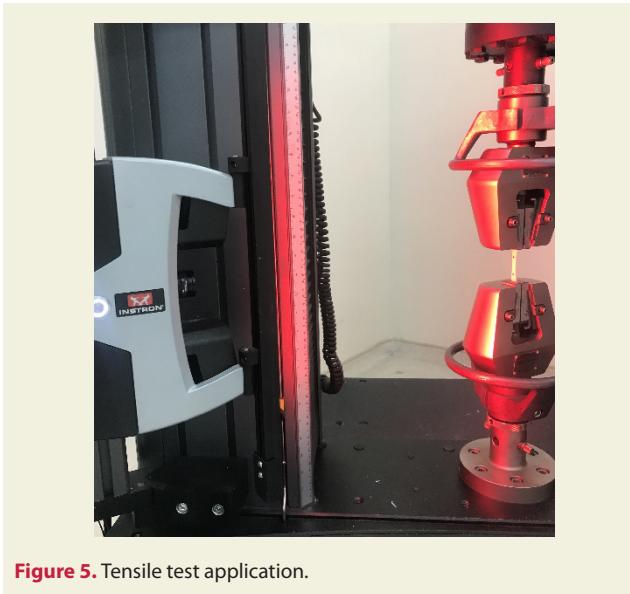
Figure 5. Tensile test application.

For FT-IR analysis of DP460 structural adhesives with no nanostructure additives, MWCNT-COOH and CF additives, an area of 5 mm^2 was taken from the produced bulk samples and placed in the reflectance unit of the FT-IR device. Spectra were made using Shimadzu IRTracer-100 model FT-IR/ATR instrument in the wavenumber range of 4000 to 400 cm^{-1}.

In addition, the surface morphology and the presence of nanostructure of carbon filaments oxidized with nitric acid were observed with a scanning electron microscope (SEM FEI-Quanta 250).

3. Results and discussion

In order to obtain force-displacement data of adhesives with and without nanostructure additives, the samples were loaded until rupture occurred. The force data obtained from the device were converted to stress by dividing the area (thickness x width) from the measuring length region of each sample prior to testing. The aim here is to see the effect of the nanostructure additive

on the adhesive independent of the area. First of all, force-elongation curves were obtained as a result of the experiments. Then, true stress-true strain (s_t-e_t) curves for adhesives were obtained using the formulas given in equation (1) (Figure 6) [10, 12].

$$\varepsilon = \frac{\Delta l}{l_0} \quad \sigma = \frac{P}{A} \quad \varepsilon_t = \ln(1+\varepsilon) \quad \sigma_t = \sigma(1+\varepsilon) \quad (1)$$

When the curves given in Figure 6 are examined, adding 1wt% of MWCNT-COOH into the medium hardness DP460 adhesive more than doubles the deformability of the adhesive. In addition, considering that the area under the stress-strain curve gives the energy absorbed by the adhesive [13], the energy absorbed by the 1 wt% MWCNT-COOH added adhesive (A-2) increased by approximately 335% compared to the adhesive without nanostructure additive (A-1). However, adding CF to the adhesive (A-3, A-4, A-5 and A-6) reduces the deformability of the adhesive somewhat and hardens the adhesive.

When the data given in Figure 7 are examined in terms of stress, adding 1wt% of MWCNT-COOH to the adhesive (A-2) increases the maximum stress by 17%, while adding 1wt% of CF without chemical surface treatment (A-3) increases the maximum stress by 21%. . However, increasing the oxidative groups on the filament surface (A-5) by chemical surface treatment of the CFs added to the adhesive increases the maximum stress by approximately 41%. In short, oxidation of the surface of CFs with HNO$_3$ solution increases the maximum stress of the adhesive by 20%. To explain the reason for this, the SEM images taken from the untreated (A-3) and chemically surface-treated (A-7) adhesive given in Figure 8 need to be examined. When these images were examined, the oxidative groups on the surface of the filaments treated with HNO$_3$ solution increased. These oxidative groups reduce the surface energy between epoxy and filament, resulting in better dispersion of epoxy and filament, as well as improving adhesive attraction forces. This situation, which prevents
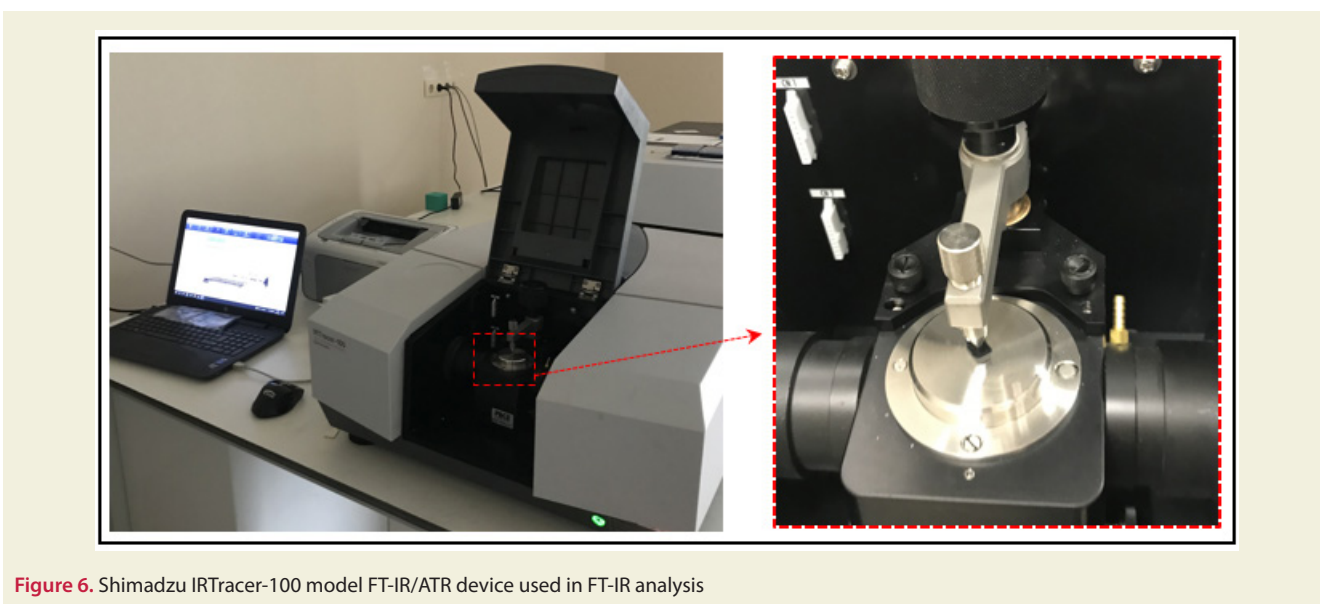
Figure 6. Shimadzu IRTracer-100 model FT-IR/ATR device used in FT-IR analysis

the filaments from being easily stripped from the epoxy, increases the performance of the adhesive.

One of the main objectives of the presented study is to examine how the performance of the adhesive changes with the addition of both MWCNT-COOH and CF

nanostructures to the adhesive. Therefore, the performance of the adhesive (A-7) formed by adding 0.5% by weight of chemically treated CF and 0.5% by weight of MWCNT-COOH to the adhesive is 46% higher than the performance of the adhesive (A-2) formed by adding only 1% by weight of MWCNT-COOH to the adhesive. At

	Max. Stress (MPa)
A-1	$44.04^{\pm0.5}$
A-2	$51.43^{\pm0.7}$
A-3	$53.45^{\pm0.9}$
A-4	$52.34^{\pm0.6}$
A-5	$62.12^{\pm0.8}$
A-6	$65.24^{\pm0.9}$
A-7	$75.21^{\pm1.1}$
A-8	$71.82^{\pm1.3}$

Figure 7. True stress-true strain curves obtained from nanostructure doped DP460 adhesive.

Figure 8. SEM images of untreated and HNO3-treated filaments, a) A-3 adhesive type, b) A-7 adhesive type.

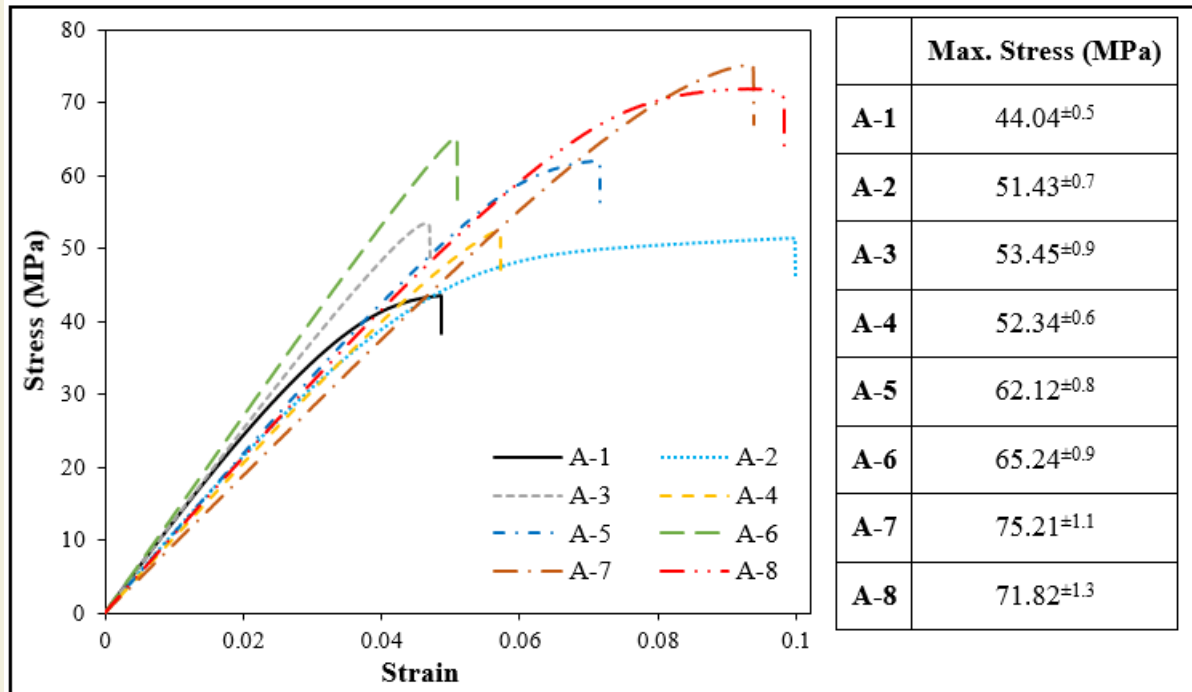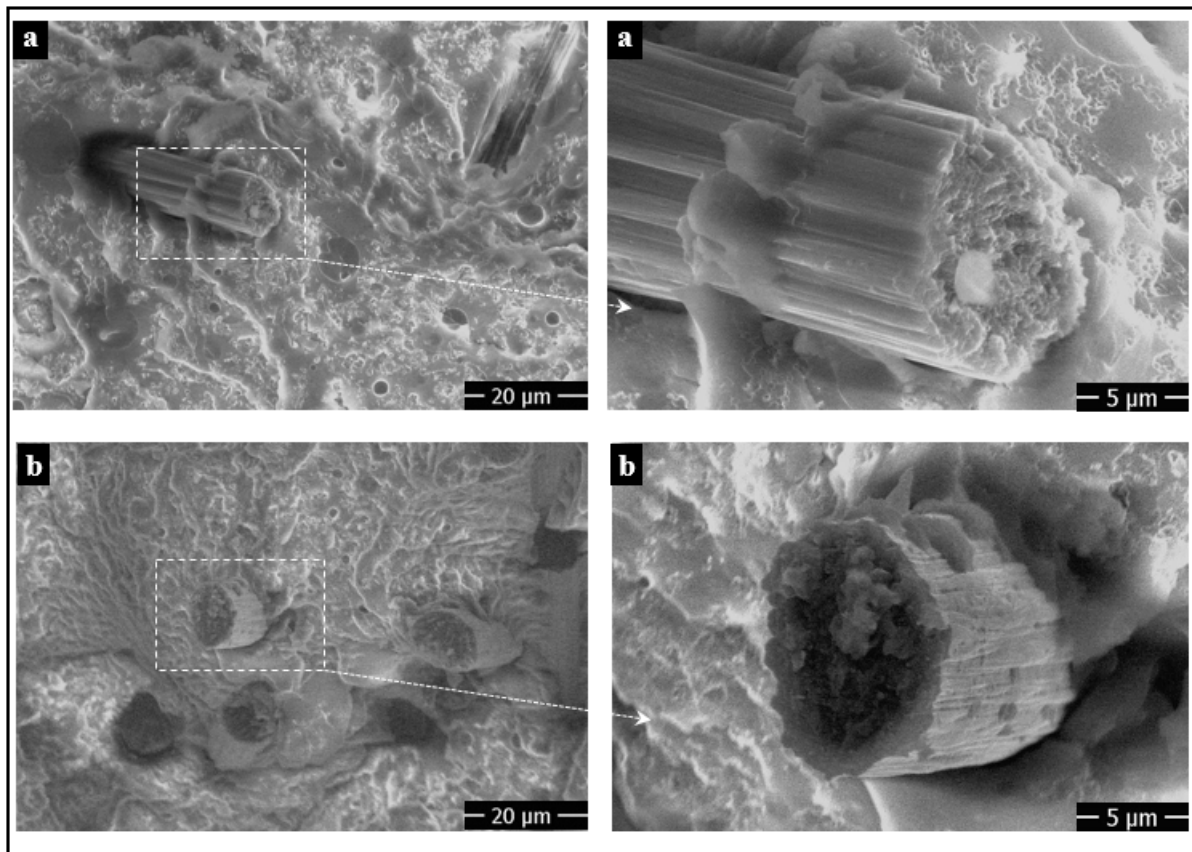the same time, it is 21% higher than the performance of the adhesive (A-5) created by adding only 1% by weight of chemically treated CF to the adhesive (Figure 7). One of the important results obtained here is that the use of chemically treated CF is more suitable than the use of MWCNT-COOH nanostructure in terms of the performance of the adhesive, and most importantly, the use of MWCNT-COOH and CF nanostructures together without changing the total nanostructure ratio in the adhesive significantly improves the performance of the adhesive. In addition, as the nanostructure ratio in the adhesive increases, the rate of increase in the maximum stress of the adhesive reduces. That is, the maximum stress obtained by adding 0.5 wt% CF to the adhesive by weight is 52.34 MPa, while the maximum stress is 62.12 MPa when the CF ratio is increased by 1 wt%, and the maximum stress is 65.24 MPa when the CF ratio is increased by 2 wt% (Figure 7).

In Figure 9, the fracture surface SEM morphology of the adhesive with no filament additives, 1 wt% MWCNT-COOH added and 1% wt CF added adhesive is given. When these images are examined, it is seen that the peaks and valleys in the fracture surface morphology of the pure adhesive are minimal and close to smooth (Figure 9 a). However, when 1% by weight of MWCNT-COOH is added to the adhesive, the adhesive becomes ductile and the fracture surface morphology becomes rough (Fig. 9 b). The reason for this may be the increase of capillary cracks that cause damage to the adhesive due to the homogeneously dispersed and epoxy coated MWCNT-COOH nanostructures of 10 to 30 mm in length. In

addition, when the fracture surface morphology of the 1% by weight CF-added adhesive given in Figure 9c is examined, it is seen that the peaks and valleys are sharp where the filament are located, and some filament are stripped from the epoxy. This situation shows the importance of applying HNO_3 oxidation to CFs.

Figure 10 shows the FTIR spectra of pure DP460 structural adhesive, adhesive containing acidic functional group-multi-walled carbon nanotube (MWCNT-COOH), adhesives containing the untreated and acid-treated carbon filament (CF), and composites containing these components in various compositions. From this figure, the peaks around 3440 cm^{-1} in the spectrum of the pure adhesive bind to the hydroxyl group (-OH), while the peaks at 2916, 2848 and 2933 cm^{-1} can be attributed to the asymmetrical and symmetrical C-H stretching, the asymmetrical stretching C-H of -CH$_3$ group and the asymmetrical C-H stretch of -CH$_2$ group, respectively.

Aromatic C-C stretch vibrations are likely represented by peaks observed at 1609, 1560, 1508, and 1449 cm^{-1}. Additionally, peaks at 1228, 1301, 1122, and 1033 cm^{-1} may signify asymmetric –CH2 deformation, asymmetric aromatic C-O stretch, asymmetric aliphatic C-O stretch, and symmetric aromatic C-O stretch, respectively. Furthermore, peaks at 960, 893, and 889 cm^{-1} could be attributed to epoxide ring vibrations, while the peak at 792 cm^{-1} may indicate out-of-plane deformation of aromatic -CH.

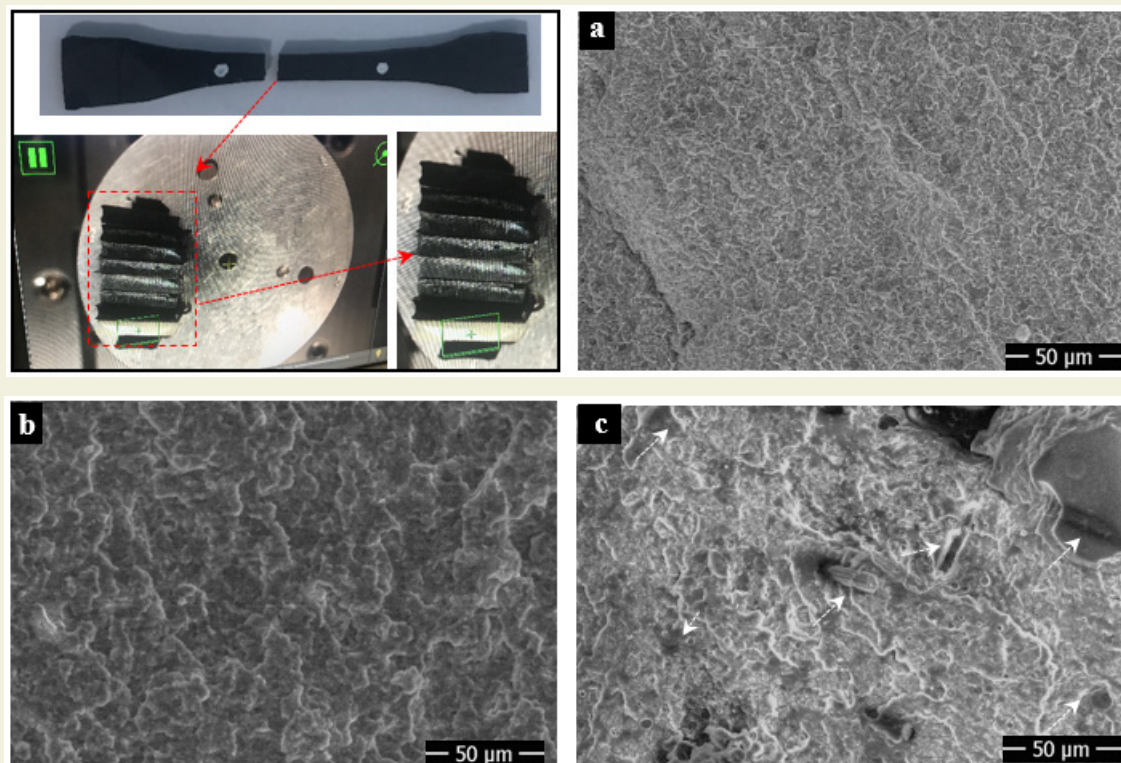In the spectrum of acid-functionalized MWCNT depicted in Figure 10, several peaks are discernible, includ-

Figure 9. Surface SEM images of the adhesive bulk samples broken after the tensile test, a) A-1 adhesive type, b) A-2 adhesive type, c) A-3 adhesive type.
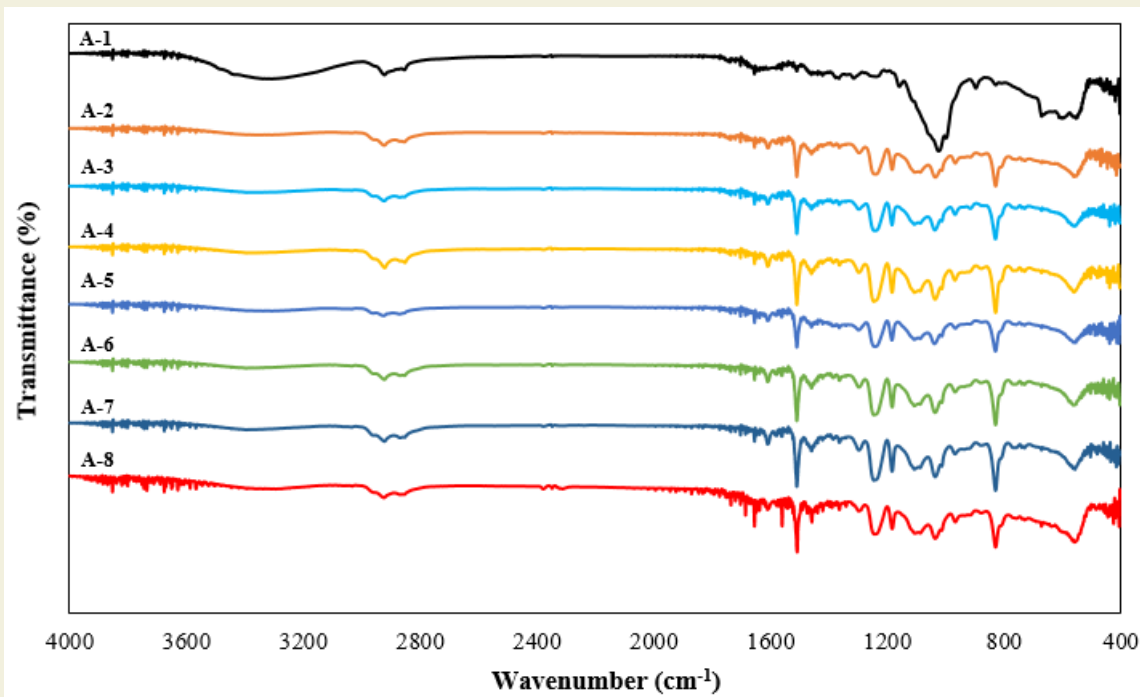
Figure 10. FT-IR spectra of DP460 structural adhesives with no nanostructure additives, MWCNT-COOH and CF additives.

ing those at 1560, 2933, 2848, and 3446 cm^{-1}. The peak around 3440 cm^{-1} is likely due to the presence of the hydroxyl group (-OH), while peaks at 2933 and 2848 cm^{-1} suggest asymmetric and symmetrical CH stretching. Moreover, peaks at 1560, 1722, and 1228 cm^{-1} may correspond to carboxylic acid group stretching modes, serving as clear indicators of the presence of -COOH groups on the nanotubes' surface.

From the spectra of the untreated and acid-treated carbon filament (CF) samples in Figure 10, it can be said that the peak at 3453 cm^{-1} corresponds to the hydroxyl (-OH) groups, the peaks at 2934 and 2849 cm^{-1} correspond to the methylene group, the low intense peak at 1772 cm^{-1} corresponds to the C=O vibrations and the peaks between 1600-1700 cm^{-1} correspond to the C=C vibration. The appearance of peaks indicating -CO and -COOH groups in the spectrum of acid-treated CF can clearly indicate the formation of oxy groups on the CF surface. On the other hand, in all spectra, the peaks at 901 cm^{-1} can be attributed to the stretching vibrations of the epoxy groups, while the peaks at 830 cm^{-1} and the peaks at 3368 and 1560 cm^{-1} can be attributed to C−O stretching vibrations and N-H vibrations, respectively.

In the spectra of the adhesive samples to which MWCNTCOOH and acid-treated CF were added in various proportions, the intense peak indicating aromatic ring -C=C- vibrations at 1506 cm^{-1}, corresponding to the subtituated -C=C- vibrations at 827 cm^{-1} severe peak and intense -C-O stretching vibration peak at 1236 cm^{-1} appeared. The intensity of these peaks especially increased with the increase of the acid-treated CF ratio. The intensity of these peaks especially increased with the increase of the acid-treated CF ratio. This may possibly have led

to a decrease in the interfacial energy of CF and epoxy, thus increasing the effectiveness of their adhesive interaction. It can also be argued that the lower interfacial energy of nano- and micro-additives with both lyophilic and lyophobic parts creates a better mixing regime with the epoxy matrix. The decrease in the intensity of the peak, which indicates the epoxy group of the pure adhesive, can also be attributed to the adhesive interactions between this group and the oxy groups.

4. Conclusions

In order to improve the performance of structural adhesives, the appropriate ratio of MWCNT-COOH and CF nanostructures to the adhesive was applied together and chemical surface treatment was applied to ensure the adhesion of the CFs to the epoxy. The removal of the oxide layer on the surface of the CFs with the HNO3 solution and the increase of the oxidative groups on the filament surface increase the performance of the adhesive by approximately 48%. In addition, different ratios of CF were added to the adhesive, and the most suitable ratio was obtained as 1% by weight.

It was concluded that adding 1% by weight of MWCNT-COOH nanostructure to the adhesive significantly increased the strain of the adhesive, but adding CF to the adhesive reduced the strain of the adhesive. Considering this situation, the addition of 1 wt% MWCNT-COOH and CF nanostructures by total weight to the adhesive both balanced the deformation of the adhesive and increased the performance of the adhesive by 71%. In addition, these experimental results were supported by SEM surface morphology images and FT-IR analyzes taken from the nanostructured and undoped adhesive.

Acknowledgment

5. References

[1] Grant, L.D.R., Adams, R.D., da Silva L.F.M. (2009). Experimental and Numerical Analysis of Single-Lap Joints for the Automotive Industry. International Journal of Adhesion and Adhesives, 29 (4), 405-413.

[2] Yang, X., Wang, Z., Xu, M., Zhao, R., Liu, X. (2013). Dramatic mechanical and thermal increments of thermoplastic composites by multi-scale synergetic reinforcement: Carbon fiber and graphene nanoplatelet, Materials and Design, 44, 74–80.

[3] Rafiee, M.A., Rafiee, J., Wang, Z., Song, H., Yu, Z.Z., Koratkar, N. (2009). Enhanced mechanical properties of nanocomposites at low graphene content. ACS Nano, 3 (12), 3884-3890.

[4] Park, S.W., Kim, B.C., Lee D.G. (2009). Tensile strength of joints bonded with a nano-particle- reinforced adhesive. Journal of Adhesion Science and Technology, 23 (1), 95-113.

[5] Sihn, S., Ganguli, S., Roy, A.K., Qu, L., Dai, L. (2008). Enhancement of through-thickness thermal conductivity in adhesively bonded joints using aligned carbon nanotubes. Composites Science and Technology, 68, 658-665.

[6] Hsiao, K.T. (2003). Use of epoxy/multiwalled carbon nanotubes as adhesives to join graphite fibre reinforced polymer composites. Nanotechnology, 14 (7), 791-793.

[7] Tiwari S., Bijwe J., Panier S. (2011). Tribological studies on polyetherimide composites based on carbon fabric with optimized oxidation treatment. Wear, 271, 2252-2260.

[8] Lou S., Ren G., Zhang H., Cheng B., Chen P. (2022). Effect of Surface Treatment on Properties of Carbon Fiber and Glass Fiber Hybrid Reinforced Composites. Fibers and Polymers, 23; 3225–3231.

[9] Akpinar S, Çalık A. (2023). The effect of fiber length and structure on joint strength in bonded joints with fiber-reinforced composite adhesive. International Journal of Adhesion & Adhesives, 124; 103365.

[10] Akpinar S., Akbulut H., Özel A., Avinç Akpinar İ., Kanar B. (2018). Improving the Thermal Cycle Performance of Structural Adhesives Used in Aerospace with Carbon Nanostructure Additives, Tubitak, Project number 114M408.

[11] ISO 2818 (2009). Plastics- Preparation of test specimens by machining.

[12] Avinc Akpinar I., Gürses A., Akpinar S., Gultekin K., Akbulut H., Ozel A. (2018). Investigation of Mechanical and Thermal Properties of Nanostructure-Doped Bulk Nanocomposite Adhesives. The Journal of Adhesion, 2018; 94,847-866.

[13] Gavgali E, Sahin R, Akpinar S. (2021). An investigation of the fatigue performance of adhesively bonded step-lap joints: An experimental and numerical analysis. International Journal of Adhesion & Adhesives, 104; 102736.

Augmentation of thermohydraulic performance in a dimpled tube using ternary hybrid nanofluid

Orhan Keklikcioglu[1*]

[1]Department of Mechanical Engineering, Faculty of Engineering, Erciyes University, Turkey

Orcid: O. Keklikcioglu (0000-0002-6227-3130)

Abstract: This computational study explores the thermal and hydraulic efficiency of heat exchanger tube configurations utilizing hybrid nanofluids and circular dimples. Seven distinct configurations incorporating different volumetric concentrations of three nanoparticles (GnP, MWCNT, and Fe_3O_4) and two circular dimple pitch ratios are examined. The investigation concentrates on crucial parameters, including Nusselt number, friction factor, and thermohydraulic performance. The numerical analysis specifically addresses single-phase flow within the Reynolds number range of 5000-30000, maintaining a constant surface heat flux during simulations. Notably, Nusselt number consistently rises with Reynolds number across all configurations. Friction factor analysis indicates minimal sensitivity to hybrid nanofluid ratios but an increase with circular dimples. Despite the elevated pressure drop, the thermohydraulic coefficient consistently surpasses 1, signifying a net energy gain from enhanced heat transfer. Optimal performance is observed in the S5-P/Dt=1 configuration, exhibiting the highest thermohydraulic coefficient at 1.35, while the P/Dt =2 variation within the same fluid model presents a slightly lower value of 1.32.

Keywords: Hybrid nanofluid, heat transfer enhancement, circular dimple, thermohydraulic performance.

1. Introduction

Improving the efficiency of cooling and heating systems can be achieved by enhancing heat transfer. Research on the enhancement of heat transfer is essential to reduce energy losses in the increasing energy demand in the current century [1-2].

In general, inserts are placed in the flow passage to enhance the heat transfer rate, resulting in a reduction in the hydraulic diameter of the flow passage [3]. Heat transfer enhancement consists of two different techniques, active and passive. Heat transfer enhancement in active methods requires external inputs such as electrostatic fields, mechanical vibration, or pulsation [4]. Passive methods deal with surface shape modifications or intensify the flow turbulence to enhance the heat transfer [5,6]. Porous materials [7-9], corrugated surfaces [10-13], extended surfaces [14-16], dimples [17-21], inserts such as wire coils, swirl flow tools, protrusions [22-25], and nanofluids [26-28] are some examples of passive techniques.

Considering the thermal-hydraulic performance, it becomes clear how significant the passive method is. In industries, improving thermal contact and reducing pumping power are crucial in terms of efficiency and economy to design better heat exchangers. The studies in the literature about passive methods show significant results

in thermal-hydraulic performance. Vicente et al. [29,30] presented that roughness has a powerful impact on the enhancement of thermal performance and, energy efficiency in their two studies with dimpled tubes and corrugated tubes, respectively. Zheng et al. [31] represented that the appliance of the inclined grooved tube enhances the heat transfer and friction factor (f) in the range of approximately 1.23 - 2.17 and 1.02 - 3.75 compared to smooth tubes, respectively. Chen et al. [32] analyzed the comparison of six different oriented dimpled copper tubes with a smooth tube. In their study, they tried to find the best performance according to the geometrical configuration of dimples. The maximum performance improvement has been found in the largest value of the ratio of the depth of the dimple to the inner diameter, the pitch of the dimple, and the number of dimples longitudinally. The heat transfer coefficient has improved between 1.25 - 2.37 times at a constant Re. In addition, the increase in f is between 1.08 to 2.35 higher than the smooth tube. In their study, the exponential Reynolds number (Re) is between 0.883 and 0.934. Piper et al. [33] probed the dimpled surface to enhance the pillow-plate heat exchanger. They showed that a dimpled surface decreased the pressure drop by around 9%. Similarly, comparing the dimpled surface with a smooth surface, the mean heat transfer coefficient has improved by 2.2%, and thermo-hydraulic performance enhanced by 11.2%. Bi

et al. [34] used two different heat passive methods dimples, grooves, and fins to improve heat transfer in their studies. In their study, apart from these three methods, they also examined different geometric configurations to select the most effective dimple. They showed that at lower Re of $Re<3323$ grooves have the highest value of PEC of around 1.35. However, dimple surfaces will reach the best performance of heat transfer augmentation as the Re increases. Moreover, the geometrical configuration of dimples in the study shows that the heat transfer enhancement is easier when the dimples are deeper with a large diameter. Xie et al. [21] analyzed the effect of cross ellipsoidal dimples on heat transfer based on different structural parameters. They indicated that although Nusselt number (Nu) and f increase with the increase in the depth of the dimples, Performance Evaluation Criteria (PEC) decreases. Moreover, another parameter in the study shows that Nu is inversely proportional to pitch. Similarly, the largest PEC is obtained in the smallest pitch in this case. Similar to pitch, PEC is inversely proportional to the axis ratio. As a result of their study, they obtained the highest PEC as 1.58 at a constant Re of 5000 with the combination of three structural parameters. Corrugated surfaces, fins, and dimples provide heat transfer improvement up to some limits due to their low heat transfer performance. Using nanoparticles with these methods improves heat transfer augmentation. Kabeel et al. [35] examined the effect of nanoparticles on the corrugated surface in their study. They have used Al_2O_3 nanomaterial in the water-based fluid with different volumetric concentrations (1-4%). In the study, the heat transfer coefficient increased up to 13% after adding nanomaterial with a 4% concentration. Khairul et al. [36] showed that using nanofluid of CuO with the corrugated surface enhanced the heat transfer coefficient up to 24.7%. Firoozi et al. [26] numerically investigated the heat transfer characteristics of nanofluid in 27 configurations of the dimple. They achieved the highest PEC of 2.50 and 3.12 for water and the flow of Al_2O_3 nanofluid, respectively. Suresh et al. [37] experimentally showed that CuO/Water nanofluid enhanced the heat transfer coefficient 1.06 times and 1.15 times based on the concentration of the nanoparticles of 0.1% and 0.3% in the helically dimpled tube, respectively.

Recently, hybrid nanofluids are attracting more attention as a new heat transfer enhancement method. Hybrid nanofluid consists of two or more different nanoparticles. In the literature, it has been seen that hybrid nano-

fluids are more effective in improving heat transfer than monotype nanofluids [38]. There are several studies about hybrid nanofluids. Toghraie et al. [39] researched the effect of hybrid nanofluids on thermal conductivity. The study showed that ZnO–TiO$_2$ hybrid nanofluids in ethylene glycol enhanced the thermal conductivity by around 32%. Sundar et al. [40] experimentally observed that nanodiamond-nickel hybrid nanofluid in water base fluid enhanced the thermal conductivity and viscosity by around 29% and 23%, respectively compared to water. Moreover, the Nu enhancement is about 25% and 35% according to 0.1% and 0.3% volumetric concentration of hybrid nanofluid. Khan et al. [41] demonstrated that alumina/silica hybrid nanofluid achieved the maximum value of PEC as 1.24 in the mini channel heat sink. Ahmed et al. [42] numerically investigated the thermo-hydraulic performance of nanofluids in a dimpled channel. The result shows that the heat transfer coefficient is 35% for the dimpled channel and around 46%, 44%, and 42% for Al_2O_3, Al_2O_3-CuO, and CuO nanofluids, respectively.

As it can be seen that different configurations of dimples and different passive methods are used in the literature review. In addition, heat transfer enhancement was made by using these passive methods with the combination of different nanofluids. As seen in these studies, it is possible to improve heat transfer at certain rates with different configurations of different methods. In this study, seven different configurations of hybrid nanofluids are studied from different volumetric concentrations of three (GnP, MWCNT, Fe$_3$O$_4$) nanoparticles. The most effective configuration is tried to be obtained by analyzing these seven different hybrid nanofluids in a pipe with a dimpled surface. In addition, graphene, carbon nanotube, and iron oxide nanoparticles with different geometrical shapes are studied as nanoparticles. The addition of iron oxide to these hybrid nanofluids will also allow for thermal performance modification using active methods in the future.

2. Materials and Method

2.1. Numerical model
The objective of this research is to investigate the thermohydraulic performance of a dimpled tube using CFD software, considering different ternary nanofluid compositions. The solution domain for a dimpled tube is illustrated in Figure 1, while Table 1 outlines the physical parameters of the numerical model.
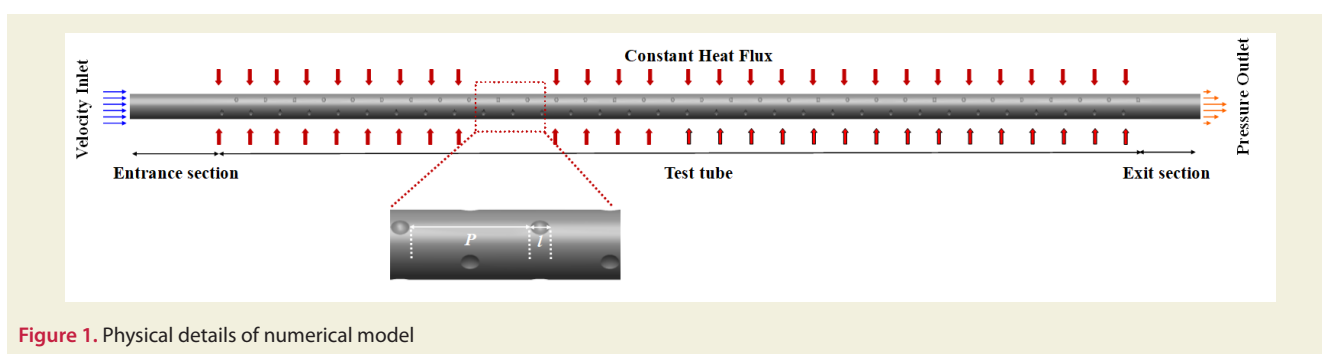

Figure 1. Physical details of numerical model

The numerical model consists of three sections: the inlet, the test, and the outlet. The inlet section generates flow hydrodynamically and prevents any disturbances at the entrance of the tube. The lengths of the inlet, test, and outlet sections are chosen to be 100 mm, 1000 mm, and 50 mm, respectively. The outer surface of the tube wall is exposed to a continuous heat flow of 20 kW/m². The investigation involves the use of ternary hybrid nanofluid configurations flowing through the tube with *Re* ranging from 5000 to 30000. The numerical analyses consider parameters such as the pitch ratio (P/D_t = 1 and 2) and nanoparticle loading fraction.

Table 1. Geometrical parameters of dimpled tube.

Geometric parameter	Value(mm)
Diameter of tube(D_t)	15
Length of entrance section(L_{ent})	100
Length of test tube(L_t)	1000
Length of exit section(L_{ex})	50
Length of dimple(l)	4
Height of dimple(h_d)	1.5
Pitch ratio (P/D_t)	1 and 2

2.2. Nanofluid configurations and thermophysical properties

In this study, the overall hybrid nanofluid volume ratio was set at 1.5%. The volumetric contribution levels of GnP, MWCNT, and FE_3O_4 nanoparticles, which compose the hybrid nanofluid, were varied within the range of 0.25-0.75% to establish seven distinct fluid configurations as given in Table 2.

Table 2. The volumetric contribution levels of nanoparticles

No	GnP	MWCNT	FE_3O_4	Total
		Volume fractions		
S1	0.0050	0.0050	0.0050	0.015
S2	0.0050	0.0075	0.0025	0.015
S3	0.0050	0.0025	0.0075	0.015
S4	0.0025	0.0050	0.0075	0.015
S5	0.0075	0.0050	0.0025	0.015
S6	0.0025	0.0075	0.0050	0.015
S7	0.0075	0.0025	0.0050	0.015

Table 3. Thermophysical properties of ternary hybrid nanofluid components[43]

Properties	Water	GnP	MWCNT	FE_3O_4
$\rho_{(kg/m^3)}$	998.2	2250	2100	5180
$C_{p(J/kg\,K)}$	4182	790	710	104
k (W/mK)	0.6	3000	2000	17.65

$$\mu_{Thnf} = \frac{\mu_f}{(1-\phi_1)^{2.5}(1-\phi_2)^{2.5}(1-\phi_3)^{2.5}} \quad (1)$$

$$\rho_{Thnf} = \left[(1-\phi_1)\{(1-\phi_2)[(1-\phi_3)\rho_f + \rho_3\phi_3] + \rho_2\phi_2\} + \rho_1\phi_1\right] \quad (2)$$

$$(\rho C_p)_{Thnf} = (1-\phi_1)\left\{(1-\phi_2)\left[(1-\phi_3)(\rho C_p)_f + (\rho C_p)_{s_3}\phi_3\right] + (\rho C_p)_{s_2}\phi_2\right\} + (\rho C_p)_{s_1}\phi_1 \quad (3)$$

$$\frac{k_{Thnf}}{k_{hnf}} = \frac{k_1 + 2k_{nf} - 2\phi_1(k_{nf} - k_1)}{k_1 + 2k_{nf} + \phi_1(k_{nf} - k_1)} \quad (4.a)$$

$$\frac{k_{hnf}}{k_{nf}} = \frac{k_2 + 2k_{nf} - 2\phi_2(k_{nf} - k_2)}{k_2 + 2k_{nf} + \phi_2(k_{nf} - k_2)} \quad (4.b)$$

$$\frac{k_{nf}}{k_f} = \frac{k_3 + 2k_{nf} - 2\phi_3(k_{nf} - k_3)}{k_3 + 2k_{nf} + \phi_3(k_{nf} - k_3)} \quad (4.c)$$

The unique thermophysical characteristics of three distinct nanoparticles and the base fluid (water), as outlined in Table 3, were utilized to calculate the viscosity, density, specific heat, and thermal conductivity of the ternary hybrid nanofluid using the Equations 1-4, respectively. Subsequently, the thermophysical properties of the seven different configurations were determined and subjected to further analysis.

2.3. Solution methodology

In this research, numerical analysis was conducted using the finite volume method in ANSYS Fluent 18. The turbulence model employed was the k - ε RNG (Re-Normalization Group), and the SIMPLE algorithm scheme was utilized to assess the correlation between pressure and velocity. For convection evaluation, the QUICK scheme was implemented. Convergence criteria for continuity, velocity, energy, k, and ε values were set at 1x10^{-5}. The k - ε RNG model, known for its precision among turbulence models, is based on three conservation equations of mass, momentum and energy, outlined in Equations 5, 6, and 7, respectively [44].

$$\nabla(\rho\vec{V}) = 0 \quad (5)$$

$$\nabla(\rho\vec{V}\vec{V}) = -\nabla P + \nabla(\mu\nabla\vec{V}) \quad (6)$$

$$\nabla(\rho c_p \vec{V}T) = \nabla(k\nabla T) \quad (7)$$

For the solution method RNG, the transport equations for k and ε are given in Equations 8 and 9, respectively.

$$\frac{\partial}{\partial t}(\rho k) + \frac{\partial}{\partial x_i}(\rho k u_i) = \frac{\partial}{\partial x_j}\left(\alpha_k \mu_{eff}\frac{\partial k}{\partial x_j}\right) + G_k + G_b - \rho\epsilon - Y_m + S_k \quad (8)$$

$$\frac{\partial}{\partial t}(\rho\epsilon) + \frac{\partial}{\partial x_i}(\rho\epsilon u_i) = \frac{\partial}{\partial x_j}\left(\alpha_\epsilon \mu_{eff}\frac{\partial\epsilon}{\partial x_j}\right) + C_{1\epsilon}\frac{\epsilon}{k}(G_k + C_{3\epsilon}G_b) - C_{2\epsilon}\rho\frac{\epsilon^2}{k} - R_\epsilon + S_\epsilon \quad (9)$$

Within these equations, G_k represents the production value of turbulent kinetic energy resulting from the velocity gradient, and G_b signifies the production value of turbulent kinetic energy arising from buoyancy. The parameters α_k and α_ε are defined as inverse effective Prandtl numbers for k and ε, respectively. Additionally, S_k and S_ε are characterized as user-input source data.

2.4. Data reduction

In addition to computing the thermophysical properties of the hybrid nanofluids, these properties were defined and analyzed using the ANSYS Fluent 18 program. The obtained data from the analysis were used to calculate the Re, Nu, f, and thermohydraulic performance coefficient based on the following equations. Specifically, the Re was determined using Equation 10.

$$Re = \frac{\rho D V}{\mu} \tag{10}$$

The convective heat transfer coefficient is determined using Equation 11, where q' represents the applied heat flux over the flow field, and ΔT denotes the temperature difference between the surface temperature of the flow field and the average temperature as the median of the inlet and the outlet fluid temperatures in the test tube.

$$h = \frac{q'}{\Delta T} \tag{11}$$

Following the computation of the heat convection coefficient, the Nu was determined using Equation 12.

$$Nu = \frac{hD}{k} \tag{12}$$

Yet another dimensionless parameter, the coefficient of friction, was computed using Equation 13.

$$f = \frac{\Delta P}{\frac{1}{2}\rho V^2 \frac{L}{D}} \tag{13}$$

The coefficient of thermohydraulic performance was calculated using Equation 14.

$$\eta = \left(Nu_{hnf}/Nu_b\right)\left(f_b/f_{hnf}\right)^{1/3} \tag{14}$$

3. Results and Discussion

3.1. Grid independence and validation of numerical methodology

To ensure the numerical results are independent of the number of cells, a grid independence study was conducted prior to the numerical analysis in this study. The impact of varying the number of cells on Nu and friction number at a Re of 5000 was investigated. The findings indicate that the deviation in Nu and f remained below 1% when the number of cells reached around 4.12 mil-
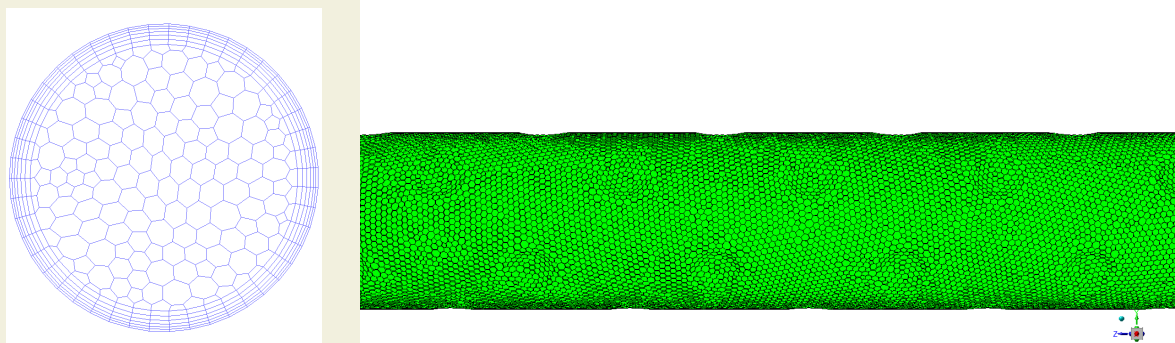

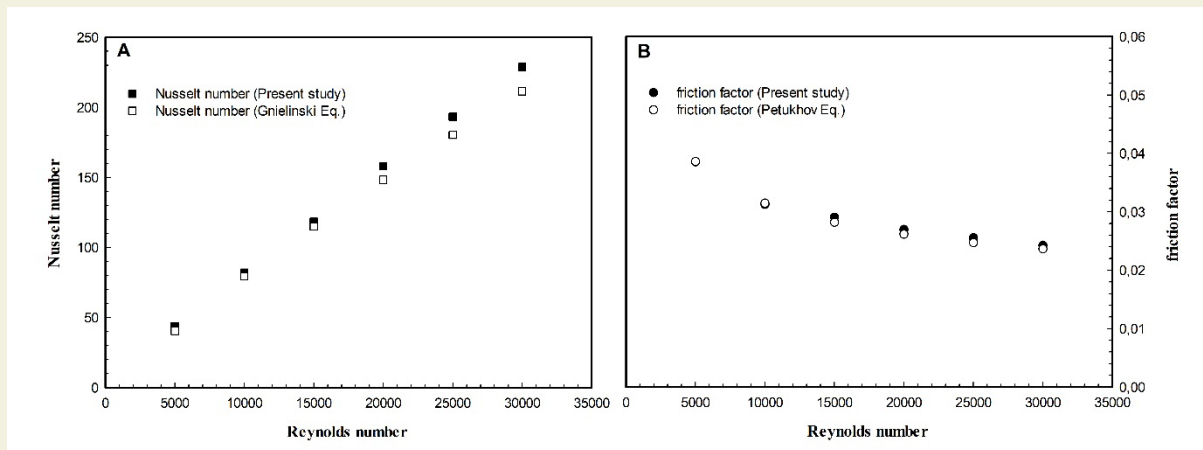**Figure 2.** Grid structure of numerical model

Figure 3. Validation results of numerical procedure

lion. The parameter y⁺, crucial for controlling mesh models, was determined to be approximately $y^+ \approx 3$ within the boundary layer region, adhering to the condition y+<5 as required. Additionally, the skewness value of the mesh structure was found to be approximately ≈0.6, while the orthogonal quality value was approximately ≈0.4. Consequently, based on this result, the polyhedral grid structure depicted in Figure 2 was selected for further analysis.

In numerical investigations, it is essential to validate the outcomes of the analogy used for parameter evaluation by comparing them with established equations. In this study, the results obtained from the analysis using water fluid were validated with the equations provided by Gnielinski [45] and Petukhov [46] for Nu and *f*, respectively, as outlined in Equations 15 and 16.

$$Nu = \frac{(f/8)(Re_D - 1000)Pr}{1 + 12.7(f/8)^{1/2}(Pr^{2/3} - 1)} \quad (15)$$

$$f = (0.79\ln(Re) - 1.64)^{-0.2} \quad (16)$$

As depicted in Figure 3, there is a remarkable agreement between the numerical results and established equations in the assessment of the Nu (Fig.3A) and *f* (Fig.3B). For the smooth heat exchanger tube utilizing water fluid, the highest observed error rates fall within the range of ±5.69% for the Nu and ±3.88% for the *f*.

3.2. Thermal and hydraulic characteristics

As illustrated in Figure 4, the Nu exhibited an ascending trend with the rise in *Re* across all configurations, aligning with expectations. The volumetric ratio of the hybrid nanofluid demonstrated a positive impact on the Nu, exhibiting an increase with the addition of the nano-additive. The incorporation of circular dimple once again resulted in enhanced heat transfer, and the *Nu* decreased as the distance between the dimples increased.

As depicted in Figure 4, the configuration S5-P/D_t=1 exhibited the most favorable thermal characteristics. The S5 fluid model comprises 0.75% GnP, 0.50% MWCNT, and 0.25% FE_3O_4, while maintaining the smallest variation in the distance between the circular dimples. In this analysis, it is substantiated that the fluid model with the highest thermal conductivity enhances thermal charac-
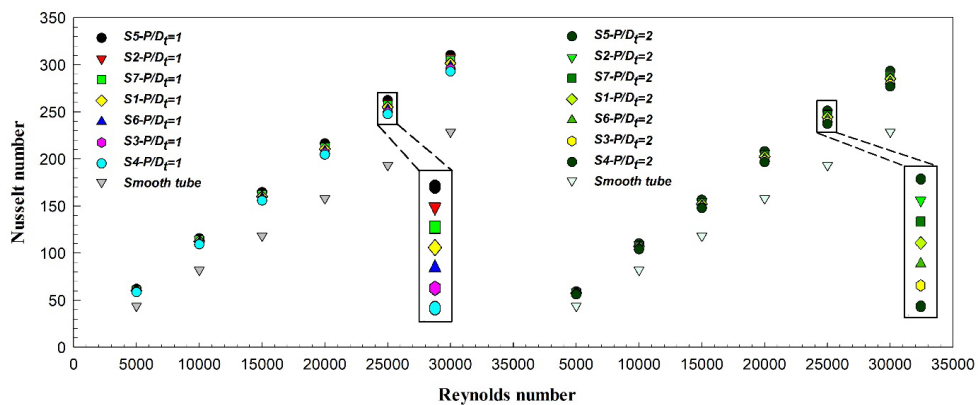

Figure 4. Distrubution of *Nu* versus *Re* for all configurations
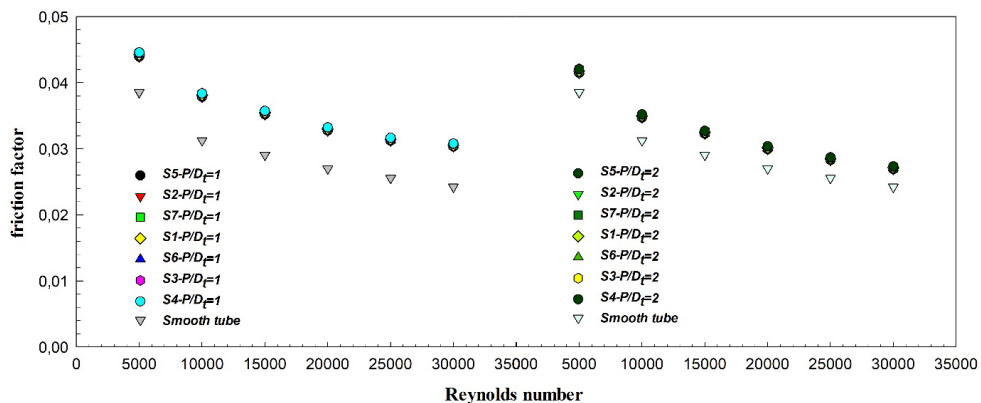

Figure 5. Distrubution of *f* versus *Re* for all configurations

teristics, and the implementation of a dimple model with a short distance is conducive to promoting turbulence.

Based on the obtained results, the S5-P/D_t =1 variation exhibited the highest Nu, reaching 61.87. This value is approximately 1.42 times higher than that of the smooth tube. In contrast, when the same fluid was used but with a P/D_t =2 variation, the Nu was slightly lower at 59.33. The lowest Nu, which was 56, occurred at P/D_t =2 for S4, representing the hybrid nanofluid model with the lowest thermal conductivity value.

As illustrated in Figure 5, the influence of hybrid nanofluid volumetric ratios on the friction coefficient appears to be quite limited. The coefficient of friction values remained approximately the same across different hybrid nanofluid mixing ratios. This consistency can be attributed to the fact that the total nanofluid volumetric ratios were consistent in all configurations.

The coefficient of friction showed an increase with the introduction of the circular dimple. Furthermore, there was a positive correlation between the coefficient of friction and the decreasing distance between the circular dimples. Conversely, a decreasing trend was observed in the coefficient of friction with an increase in Re.

Based on the results presented in Figure 5, the lowest coefficient of friction was observed for the S5-P/D_t =2 configuration at a Re of 30000. In this configuration, the f increased by 1.11 times compared to the smooth tube. On the other hand, the highest f, which was 0.04458, was found for the S4- P/D_t =1 model at the lowest Re of 5000.

3.3. Overall enhancement

In thermal systems, the implementation of heat transfer enhancement techniques is aimed at improving heat transfer, but it often comes at the cost of increased pressure drop. Recognizing that an increase in pressure drop is not a desirable outcome, Webb R.L. [47] introduced the coefficient of thermohydraulic performance. This coefficient serves as a metric to express the net energy gain in

systems where heat transfer improvement techniques are applied, offering a comprehensive assessment that considers both enhanced heat transfer and the associated increase in pressure drop.

As depicted in Figure 6, the thermohydraulic coefficient of performance for configurations employing hybrid nanofluid and circular dimple is consistently above 1. This observation suggests that the applied method is thermally and hydraulically advantageous. A coefficient of performance above 1 indicates that, despite the increase in pressure drop associated with the heat transfer enhancement techniques, the net energy gain in terms of improved heat transfer outweighs the added hydraulic losses, making the overall system more efficient.

The thermo-hydraulic results exhibit a decreasing trend with an increase in Re. Consequently, higher overall enhancement is achieved at lower Re, as the pressure drop becomes more pronounced at higher Re. Specifically, configurations with P/D_t =1 demonstrate significantly better performance values, while P/D_t =2 configurations, as anticipated, exhibit relatively lower performance.

The highest thermo-hydraulic coefficient of performance was achieved by the S5-P/D_t=1 configuration, reaching 1.35 at the lowest Re. In contrast, for the P/D_t=2 configuration within the same fluid model, this value was slightly lower at 1.32. On the other hand, the lowest performance value, amounting to 1.16, was observed at the highest Re for the S4- P/Dt =2 model. These results indicate variations in performance based on different configurations and Re, with the S5-P/Dt =1 configuration exhibiting the most favorable thermo-hydraulic performance under the specified conditions.

4. Conclusions

In conclusion, the numerical study delved into the thermal and hydraulic performance of heat exchanger configurations employing hybrid nanofluids and circular dimples. The findings offer valuable insights into various
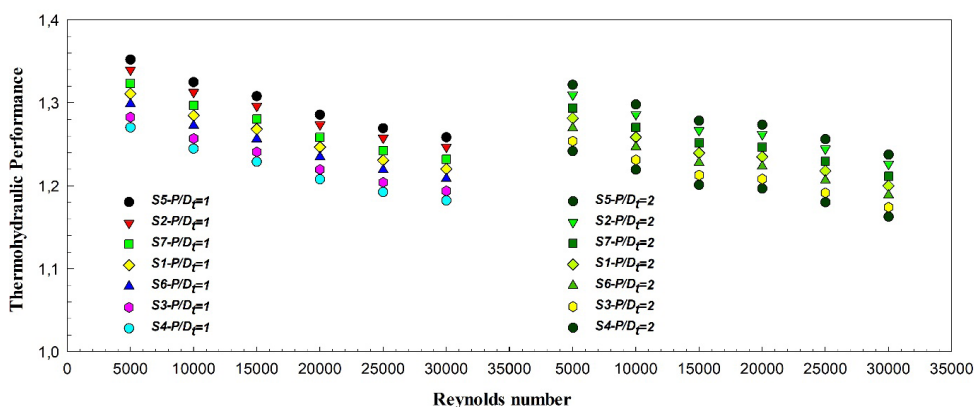

Figure 6. Distrubution of thermo-hydraulic performance versus Re for all configurations

parameters, shedding light on the effectiveness of heat transfer enhancement techniques.

- The ascending trend of Nu with increasing Reynolds number was consistently evident across all configurations, with the volumetric ratio of the hybrid nanofluid demonstrating a positive correlation, and circular dimples contributing to enhanced heat transfer. Specifically, the S5-*P/Dt*=1 configuration emerged as the most thermally favorable, showcasing superior thermal characteristics attributable to its unique fluid composition and the implementation of circular dimples with a shorter distance.

- Examining variations in the friction coefficient, the S5-*P/Dt*=2 configuration at Reynolds number 30000 yielded the lowest coefficient, albeit 1.11 times higher than the smooth tube. Conversely, the highest friction coefficient of 0.04458 was observed for the S4-*P/Dt*=1 model at the lowest Reynolds number of 5000.

- The thermohydraulic coefficient of performance consistently exceeded 1, indicating thermal and hydraulic advantages in configurations employing hybrid nanofluids and circular dimples. This signifies that, despite an associated increase in pressure drop, the net energy gain from improved heat transfer outweighs hydraulic losses.

- In terms of optimal performance, the S5-*P/Dt* =1 configuration demonstrated the highest thermohydraulic coefficient at 1.35, whereas the *P/Dt* =2 variation within the same fluid model exhibited a slightly lower value of 1.32. The lowest performance, amounting to 1.16, was observed at the highest Reynolds number for the S4-*P/Dt* =2 model.

- This comprehensive analysis offers significant insights into the intricate interplay of parameters, providing valuable guidance for the design and optimization of thermal systems employing hybrid nanofluids and circular dimples.

Nomenclature

c_p	specific heat, j/kgK
f	friction factor
FE_3O_4	Iron oxide
GnP	Graphene nanoplatelet
h	convective heat transfer coefficient, W/m^{2}K
k	thermal conductivity, W/mK
MWCNT	Multi-walled carbon nanotube
Nu	Nusselt number
P	pitch length, mm
Pr	Prandtl number
q	heat flux, W/m^2
Q	rate of heat transfer, W
r	radius of the tube, mm
Re	Reynolds number
T	temperature, K
V	average velocity, m/s
ΔP	pressure drop, Pa

Greek symbols

ρ	density, kg/m^3
μ	dynamic viscosity, kg/ms
φ	volume concentration, %

Subscripts

f	fluid
nf	nanofluid
hnf	hybrid nanofluid
$Thnf$	ternary hybrid nanofluid
b	base

Rererences

[1] Shanthi, R., Anandan, S., & Ramalingam, V. (2012). Heat transfer enhancement using nanofluids: An overview. Thermal Science, 16(2): 423–444. doi:10.2298/tsci110201003s

[2] Gürdal, M., Pazarlıoğlu, H. K., Tekir, M., Arslan, K., & Gedik, E. (2022). Numerical investigation on turbulent flow and heat transfer characteristics of Ferro-nanofluid flowing in dimpled tube under magnetic field effect. Applied Thermal Engineering, 200: 117655. https://doi.org/10.1016/j.applthermaleng.2021.117655

[3] Dewan, A., Mahanta, P., Raju, K. S., & Kumar, P. S. (2004). Review of passive heat transfer augmentation techniques. Proceedings of the Institution of Mechanical Engineers, Part A: Journal of Power and Energy. 218(7): 509–527. doi:10.1243/0957650042456953

[4] Sheikholeslami, M., Gorji-Bandpy, M., & Ganji, D. D. (2015). Review of heat transfer enhancement methods: Focus on passive

methods using swirl flow devices. Renewable and Sustainable Energy Reviews, 49: 444–469. doi:10.1016/j.rser.2015.04.113

[5] Léal, L., Miscevic, M., Lavieille, P., Amokrane, M., Pigache, F., Topin, F., … Tadrist, L. (2013). An overview of heat transfer enhancement methods and new perspectives: Focus on active methods using electroactive materials. International Journal of Heat and Mass Transfer, 61:505-524. doi:10.1016/j.ijheatmasstransfer.2013.01.083

[6] Mousavi Ajarostaghi, S. S., Zaboli, M., Javadi, H., Badenes, B., & Urchueguia, J. F. (2022). A review of recent passive heat transfer enhancement methods. Energies, 15(3): 986. https://doi.org/10.3390/en15030986

[7] Kiwan, S., & Al-Nimr, M. A. (2001). Using Porous Fins for Heat Transfer Enhancement. Journal of Heat Transfer, 123(4), 790. doi:10.1115/1.1371922

[8] Pavel, B. I., & Mohamad, A. A. (2004). An experimental and numerical study on heat transfer enhancement for gas heat exchangers fitted with porous media. International Journal of Heat and Mass Transfer, 47(23): 4939–4952. doi:10.1016/j.ijheatmasstransfer.2004.06.014

[9] Wang, B., Hong, Y., Hou, X., Xu, Z., Wang, P., Fang, X., & Ruan, X. (2015). Numerical configuration design and investigation of heat transfer enhancement in pipes filled with gradient porous materials. Energy Conversion and Management, 105: 206–215. doi:10.1016/j.enconman.2015.07.064

[10] Pethkool, S., Eiamsa-ard, S., Kwankaomeng, S., & Promvonge, P. (2011). Turbulent heat transfer enhancement in a heat exchanger using helically corrugated tube. International Communications in Heat and Mass Transfer, 38(3): 340–347. doi:10.1016/j.icheatmasstransfer.2010.11.014

[11] Kareem, Z. S., Mohd Jaafar, M. N., Lazim, T. M., Abdullah, S., & AbdulWahid, A. F. (2015). Heat transfer enhancement in two-start spirally corrugated tube. Alexandria Engineering Journal, 54(3): 415–422. doi:10.1016/j.aej.2015.04.001

[12] Kareem, Z. S., Mohd Jaafar, M. N., Lazim, T. M., Abdullah, S., & Abdulwahid, A. F. (2015). Passive heat transfer enhancement review in corrugation. Experimental Thermal and Fluid Science, 68: 22–38. doi:10.1016/j.expthermflusci.2015.04.012

[13] Kareem, Z. S., Abdullah, S., Lazim, T. M., Mohd Jaafar, M. N., & Abdul Wahid, A. F. (2015). Heat transfer enhancement in three-start spirally corrugated tube: Experimental and numerical study. Chemical Engineering Science, 134: 746.

[14] Nuntaphan, A., Vithayasai, S., Vorayos, N., Vorayos, N., & Kiatsiriroat, T. (2010). Use of oscillating heat pipe technique as an extended surface in wire-on-tube heat exchanger for heat transfer enhancement. International Communications in Heat and Mass Transfer, 37(3): 287–292. doi:10.1016/j.icheatmasstransfer.2009.11.006

[15] Nagarani, N., Mayilsamy, K., Murugesan, A., & Kumar, G. S. (2014). Review of the utilization of extended surfaces in heat transfer problems. Renewable and Sustainable Energy Reviews, 29: 604–613. doi:10.1016/j.rser.2013.08.068

[16] Yadav, V., Baghel, K., Kumar, R., & Kadam, S. T. (2016). Numerical investigation of heat transfer in extended surface microchannels. International Journal of Heat and Mass Transfer, 93: 612–622. doi:10.1016/j.ijheatmasstransfer.2015.10.023

[17] Bi, C., Tang, G. H., & Tao, W. Q. (2013). Heat transfer enhancement in mini-channel heat sinks with dimples and cylindrical grooves. Applied Thermal Engineering, 55(1-2): 121–132. doi:10.1016/j.applthermaleng.2013.03.007

[18] Turnow, J., Kornev, N., Isaev, S., & Hassel, E. (2010). Vortex mechanism of heat transfer enhancement in a channel with spherical and oval dimples. Heat and Mass Transfer, 47(3): 301–313. doi:10.1007/s00231-010-0720-5

[19] Huang, X., Yang, W., Ming, T., Shen, W., & Yu, X. (2017). Heat transfer enhancement on a microchannel heat sink with impinging jets and dimples. International Journal of Heat and Mass Transfer, 112: 113–124. doi:10.1016/j.ijheatmasstransfer.2017.04.078

[20] Huang, Z., Yu, G. L., Li, Z. Y., & Tao, W. Q. (2015). Numerical Study on Heat Transfer Enhancement in a Receiver Tube of Parabolic Trough Solar Collector with Dimples, Protrusions and Helical Fins. Energy Procedia, 69: 1306–1316. doi:10.1016/j.egypro.2015.03.149

[21] Xie, S., Liang, Z., Zhang, L., & Wang, Y. (2018). A numerical study on heat transfer enhancement and flow structure in an enhanced tube with cross ellipsoidal dimples. International Journal of Heat and Mass Transfer, 125: 434–444. doi:10.1016/j.ijheatmasstransfer.2018.04.106

[22] Tijing, L. D., Pak, B. C., Baek, B. J., & Lee, D. H. (2006). A study on heat transfer enhancement using straight and twisted internal fin inserts. International Communications in Heat and Mass Transfer, 33(6): 719–726. doi:10.1016/j.icheatmasstransfer.2006.02.006

[23] García, A., Vicente, P. G., & Viedma, A. (2005). Experimental study of heat transfer enhancement with wire coil inserts in laminar-transition-turbulent regimes at different Prandtl numbers. International Journal of Heat and Mass Transfer, 48(21-22): 4640–4651. doi:10.1016/j.ijheatmasstransfer.2005.04.024

[24] Eiamsa-ard, S., Wongcharee, K., Eiamsa-ard, P., & Thianpong, C. (2010). Heat transfer enhancement in a tube using delta-winglet twisted tape inserts. Applied Thermal Engineering, 30(4): 310–318. doi:10.1016/j.applthermaleng.2009.09.006

[25] Promvonge, P., & Eiamsa-ard, S. (2006). Heat transfer enhancement in a tube with combined conical-nozzle inserts and swirl generator. Energy Conversion and Management, 47(18-19): 2867–2882. doi:10.1016/j.enconman.2006.03.034

[26] Firoozi, A., Majidi, S., & Ameri, M. (2020). A numerical assessment of heat transfer and flow characteristics of nanofluid in tubes enhanced with a variety of dimple configurations. Thermal Science and Engineering Progress, 100578. doi:10.1016/j.tsep.2020.100578

[27] Akçay, S. (2021). Investigation of thermo-hydraulic performance of nanofluids in a zigzag channel with baffles. Adıyaman Üniversitesi Mühendislik Bilimleri Dergisi, 8 (15): 525-534.

[28] Akçay, S. (2023). Numerical analysis of hydraulic and thermal performance of al2o3-water nanofluid in a zigzag channel with central winglets. Gazi University Journal of Science, 36(1): 383-397.

[29] Vicente, P. G., Garcıa, A., & Viedma, A. (2002). Experimental study of mixed convection and pressure drop in helically dimpled tubes for laminar and transition flow. International Journal of Heat and Mass Transfer, 45(26): 5091–5105. doi:10.1016/s0017-9310(02)00215-6

[30] Vicente, P. G., Garcıa, A., & Viedma, A. (2004). Mixed convection heat transfer and isothermal pressure drop in corrugated tubes for laminar and transition flow. International Communications in Heat and Mass Transfer, 31(5): 651–662. doi:10.1016/s0735-1933(04)00052-1

[31] Zheng, N., Liu, P., Shan, F., Liu, Z., & Liu, W. (2017). Turbulent

flow and heat transfer enhancement in a heat exchanger tube fitted with novel discrete inclined grooves. International Journal of Thermal Sciences, 111: 289–300. doi:10.1016/j.ijthermalsci.2016.09.010

[32] Chen, J., Müller-Steinhagen, H., & Duffy, G. G. (2001). Heat transfer enhancement in dimpled tubes. Applied Thermal Engineering, 21(5): 535–547. doi:10.1016/s1359-4311(00)00067-3

[33] Piper, M., Zibart, A., Djakow, E., Springer, R., Homberg, W., & Kenig, E. Y. (2019). Heat transfer enhancement in pillow-plate heat exchangers with dimpled surfaces: a numerical study. Applied Thermal Engineering, 153:142-146. doi:10.1016/j.applthermaleng.2019.02.082

[34] Bi, C., Tang, G. H., & Tao, W. Q. (2013). Heat transfer enhancement in mini-channel heat sinks with dimples and cylindrical grooves. Applied Thermal Engineering, 55(1-2): 121–132. doi:10.1016/j.applthermaleng.2013.03.007

[35] Kabeel, A. E., Abou El Maaty, T., & El Samadony, Y. (2013). The effect of using nano-particles on corrugated plate heat exchanger performance. Applied Thermal Engineering, 52(1): 221–229. doi:10.1016/j.applthermaleng.2012.11.027

[36] Khairul, M. A., Alim, M. A., Mahbubul, I. M., Saidur, R., Hepbasli, A., & Hossain, A. (2014). Heat transfer performance and exergy analyses of a corrugated plate heat exchanger using metal oxide nanofluids. International Communications in Heat and Mass Transfer, 50: 8–14. doi:10.1016/j.icheatmasstransfer.2013.11.006

[37] Suresh, S., Chandrasekar, M., & handra Sekhar, S. (2011). Experimental studies on heat transfer and friction factor characteristics of CuO/water nanofluid under turbulent flow in a helically dimpled tube. Experimental Thermal and Fluid Science, 35(3): 542–549. doi:10.1016/j.expthermflusci.2010.12.008

[38] Ekiciler, R., & Samet Ali Çetinkaya, M. (2021). A comparative heat transfer study between monotype and hybrid nanofluid in a duct with various shapes of ribs. Thermal Science and Engineering Progress, 23: 100913. doi:10.1016/j.tsep.2021.100913

[39] Toghraie, D., Chaharsoghi, V. A., & Afrand, M. (2016). Measurement of thermal conductivity of ZnO–TiO2/EG hybrid nanofluid. Journal of Thermal Analysis and Calorimetry, 125(1): 527–535. doi:10.1007/s10973-016-5436-4

[40] Sundar, L. S., Singh, M. K., & Sousa, A. C. M. (2018). Turbulent heat transfer and friction factor of nanodiamond-nickel hybrid nanofluids flow in a tube: An experimental study. International Journal of Heat and Mass Transfer, 117: 223–234. doi:10.1016/j.ijheatmasstransfer.2017.09.109

[41] Khan, A., & Ali, M. (2022). Thermo-hydraulic behavior of alumina/silica hybrid nanofluids through a straight minichannel heat sink. Case Studies in Thermal Engineering, 31: 101838. https://doi.org/10.1016/j.csite.2022.101838

[42] Ahmed, F., Abir, M. A., Fuad, M., Akter, F., Bhowmik, P. K., Alam, S. B., & Kumar, D. (2021). Numerical investigation of the thermo-hydraulic performance of water-based nanofluids in a dimpled channel flow using Al2O3, CuO, and hybrid Al2O3–CuO as nanoparticles. Heat Transfer, 50(5): 5080–5105. doi:10.1002/htj.22116

[43] Mertaslan, O. M., & Keklikcioglu, O. (2024). Investigating heat exchanger tube performance: second law efficiency analysis of a novel combination of two heat transfer enhancement techniques. Journal of Thermal Analysis and Calorimetry. https://doi.org/10.1007/s10973-023-12842-6

[44] ANSYS, 2018. ANSYS Fluent Tutorial Guide, ANSYS Inc., Canonsburg.

[45] Gnielinski, V. (1976). New equations for heat and mass transfer in turbulent pipe and channel flow. International Chemical Engineering, 27; 359–368.

[46] Petukhov, B. S., Irvine, T. F., & Hartnett, J. P. (1970). Advances in heat transfer. Academic, New York, 6; 503–564.

[47] Webb, R. L. (1981). Performance evaluation criteria for use of enhanced heat transfer surfaces in heat exchanger design. International Journal of Heat and Mass Transfer, 24; 715–726.

Research Article

Theoretical comparison analysis of R134a, R1234yf, R452A and R454C refrigerants used in automobile, trailer, commercial and industrial cooling systems

Alpaslan Alkan[1*]

[1]Mechanical Engineering Department, Faculty of Technology, Sakarya of Applied Sciences University, Türkiye

Orcid: A. Alkan (0000-0001-8117-8545)

Abstract: The release of artificial substances into the environment in recent years has been the main cause of environmental disasters. Artificial refrigerants used in cooling systems have significantly contributed to the depletion of the ozone layer and global warming. In this study, theoretical performance comparisons were performed between R1234yf, which is a substitute for R134a used in automobile air conditioning (AAC) systems, and R452A, R454C refrigerants, which are used as alternative refrigerants in industrial, commercial, and trailer cooling systems. Thus, the performances of alternative refrigerants used in different cooling systems under similar conditions were comparatively evaluated. Performance analyses were carried out according to different condenser and evaporator temperatures. Analysis results are given depending on the condenser/evaporator pressure ratio, mass flow rate, compressor power, cooling effect coefficient (COP) and compressor outlet temperature. According to the study results, it was observed that the COP increased with the increase in evaporator temperature, while the compressor inlet-outlet pressure ratio, refrigerant mass flow rate, compressor power and refrigerant compressor outlet temperature decreased. According to the study, the refrigerant with the highest compressor power and mass flow rate was R452A, followed by R1234yf, R454C, and R134a. The average COP of R134a was found to be approximately 5.4%, 8.6%, and 0.6% higher than R1234yf, R452A, and R454C, respectively. The compressor powers of R134a, R1234yf, R452A, and R454C were in the range of 1.01–3.28 kW, 1.03–3.62 kW, 1.02–3.88 kW, and 0.98–3.36 kW, respectively, according to the theoretical analysis conditions.

Keywords: Automobile, Refrigeration, GWP, Energy, Theoretical, Cooling cycle.

1. Introduction

Over the last century, environmental problems in our world have increased significantly. Sudden temperature changes, solar radiation reaching the atmosphere without filtering, and large-scale pollution of the atmosphere have increased environmental problems. It is also becoming increasingly obvious how expensive and scarce energy is, especially from fossil fuels. The use of gasoline in urban automobiles and environmental pollutants have been primarily associated with gasoline consumption. Besides, vehicle air conditioning systems, also found in private and commercial vehicles, have a major impact on greenhouse gas emissions and the world's oil consumption. [1-4]. Refrigerants containing chlorofluorocarbons (CFC) and hydrochlorofluorocarbons (HCFC) interact with the ozone layer in the atmosphere and have the potential to deplete the ozone layer. This effect is called the ozone depletion potential (ODP). Chlorine atoms contained in these compounds break down ozone mol-

ecules, causing the ozone layer to weaken. Due to the ozone layer's thinning, the sun's destructive radiation reached Earth, causing environmental problems. At the same time, increasing global warming has triggered sudden meteorological events and caused the world to become even warmer. Refrigerants with high global warming potentials (GWP), when released into the environment, significantly contribute to global warming by trapping heat in the atmosphere. Efforts have been made to prevent these two situations through international agreements [5,6]. Artificial ingredients used in cooling systems can contribute to both the ozone layer and global warming. Refrigerants containing fluorine atoms are limited and prohibited to prevent ozone depletion. With the agreements taken against global warming, especially in European Union (EU) member countries, the usage of refrigerants with a GWP value of more than 150 in automobile air conditioning (AAC) systems is limited [7]. In addition to AAC systems, cooling systems are utilised in

the transportation, commercial, and industrial sectors. R404A refrigerant is used as broadcast in these cooling systems. The fact that R404A refrigerant has a GWP value of 3943 necessitated the use of an alternative refrigerant. The EU has limited the use of refrigerants with GWP values above 2500 in fixed facilities in 2020 [8]. However, the use of R404A refrigerant is allowed until 2030 under certain rules. Refrigerant R452A is increasingly being used as a replacement for R404A in trailer and pickup truck cooling systems. In recent years, there has been a shift towards using R454C refrigerant as a replacement for R404A refrigerant in commercial and industrial cooling systems. [9]. At first, R12 refrigerant was used in the AAC system. However, since it was harmful to the ozone layer, R134a refrigerant was chosen. In this case, with the understanding that R134a refrigerant has a high contribution to global warming, a widespread switch has been made to R1234yf refrigerant with a low GWP value. Some automobile companies have preferred carbon dioxide (R744) refrigerant in some of their vehicles [10].

Daviran et al. [11] simulated the cooling cycle of an AAC system with R134a and made a comparative analysis of the use of R1234yf. They stated that the cooling efficiency coefficient (COP) of the R1234yf system is 1.3 - 5% less than that of R134a at a given cooling load, and 18% higher than that of R134a at a given refrigerant mass flow rate. Zilio et al. [12] tested using R1234yf instead of R134a in an AAC system. According to their findings, R1234yf has a lower cooling capacity and COP compared to R134a. Direk and Yüksel [13] investigated the use of R1234ze(E), R152a and R444a as alternatives to R134a in an automobile heat pump system. They mentioned that R152a has a higher heating capacity than R134a, R444a, and R1234ze(E). Additionally, they noted that the heating capacity of R1234ze(E) can be increased by increasing the total compressor volume. Cho and Park [14] compared the performance of R1234yf with R134a by adding an internal heat exchanger to an AAC system. They showed that R1234yf has a lower cooling capacity in the range of 4.0–7.0% and more COP in the range of 3.6–4.5% compared to R134a. They also revealed that R1234yf had higher total exergy destruction than R134a, in the range of 0.5–3.3%. Golzari et al. [15] used a computer program to compare R134a and R1234yf and stated that R1234yf led to high exergy efficiency. Mostafa et al. [16] conducted an empirical investigation to evaluate the efficiency of R404 and R454C refrigerants in the cooling system of a cold storage facility. The experimental studies were conducted under varying outdoor and indoor air conditions, specifically considering the product's thermal load and cooling water temperature. According to their findings, R404A achieves the target temperature in the warehouse 23.1% faster than R454C, thanks to its superior cooling capability. It was discovered that R454C had a 10.8% greater COP than R404A, but its energy consumption was 20.6% higher. Aral et al. [17] compared R134a and R1234yf in an AAC system that can also operate as a heat pump. They stated that R134a has 5.8% more cooling capacity and 0.2% less heating capacity than R1234yf. Alkan and M.S İnan [18] experimentally

carried out the performance analysis of R134a refrigerant and its alternative R1234yf refrigerant in an AAC system with a variable-capacity compressor. They reported that the COP of R1234yf refrigerant decreased as compressor speed increased, except at low airflow inlet temperatures. At high airflow inlet temperatures, R134a had a COP value 20% higher than R1234yf, and at low airflow inlet temperatures, R134a had a COP value 2% higher than R1234yf. Alkan and M. S. İnan [19] conducted an experimental study to investigate the performance of R1234yf in an AAC system with variable and fixed capacity compressors. Their study showed that the COP value of the AAC system with R1234yf is 13.6% and 20.1% less than that of the variable and fixed capacity R134a system, respectively. Devecioğlu and Oruç [20] made comparisons of R404A and R452A refrigerants in a basic vapour compression refrigeration cycle according to different evaporator and condenser temperatures. They revealed that when R452A was used instead of R404A in the cooling cycle, the COP value was higher, but the power consumption of the system was less. According to them, R452A is a suitable substitute for R404A when it comes to commercial cooling applications. In another study, Devecioğlu and Oruç [21] investigated the use of R454C instead of R404A. On average, R454C's COP was 10% higher and its power consumption was 15% less than R404A. Khatoon and Karimi [22] conducted a theoretical analysis of a vapour compression system that uses two evaporators to eliminate the need for separate refrigeration and air conditioning units. They carried out energy and exergy performance evaluations, considering the changes in condenser and evaporator temperatures. They compared low-GWP refrigerants such as R1234yf, R1336mzz(Z), R513A and R450A to high-GWP refrigerants such as R134a and R452A. They found that R1336mzz(Z) had the highest exergy efficiency and COP values (31.50 and 2.47%, respectively). They also mentioned that it has the lowest compressor power. They revealed that R1336mzz(Z) was the best-performing refrigerant, while R452A exhibited the poorest thermodynamic performance.

In this study, theoretical comparisons were made between R1234yf, an alternative to R134a in AAC systems, and R452A, an alternative to R404A refrigerant in trailer-type cooling systems, and R454C refrigerants, which are used as an alternative in industrial and commercial-type cooling systems. Performance comparisons were performed for different evaporator and condenser temperatures to reveal the performance of alternatives for R134a and R404A refrigerants.

2. Theoretical Analysis

Theoretical analysis investigated the fundamental elements of the cooling cycle utilized in various systems, including AAC, trailers, industrial, and commercial cooling systems. The basic components of a cooling cycle are the compressor, condenser, evaporator, and expansion valve. A schematic view of basic cooling cycle elements is given in Figure 1.
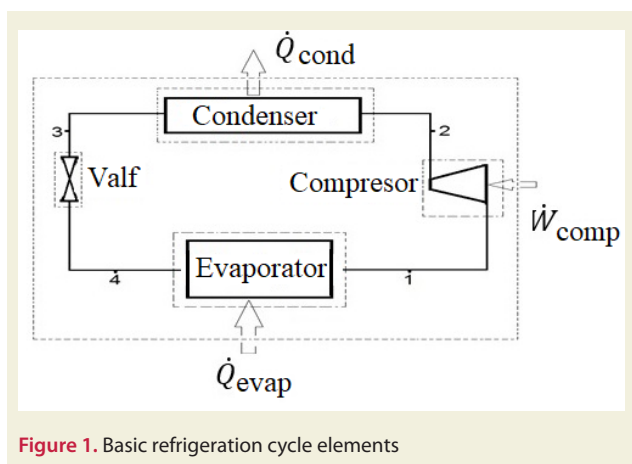
Figure 1. Basic refrigeration cycle elements

The cooling cycle in both AAC systems, trailer, industrial and commercial type cooling systems works according to the vapour compression cooling cycle. In the cycle, the element that compresses the refrigerant fluid and turns it from superheated vapour at low pressure to superheated vapour at high pressure is the compressor. In Figure 1, the refrigerant, which is in the form of superheated vapour at low pressure at point 1, is subjected to compression in the compressor and becomes superheated vapour at high pressure at point 2. There are various types of compressors used in refrigeration cycles. The condenser is the element where the refrigerant, which is in the form of superheated vapour at high pressure, turns into saturated vapour, liquid/vapour and saturated liquid by losing heat. Condensers are classified based on the type of heat rejection medium and their fin and tube types. In Figure 1, the refrigerant, which is in the form of superheated vapour at high pressure at point 2, releases heat to the environment in the condenser and becomes a saturated liquid at point 3. In the actual cooling cycle, the refrigerant in the condenser is ensured to exit at a lower temperature than the saturation temperature consistent with the condenser pressure. This difference is referred to as subcooling. Thus, the refrigerant is prevented from evaporating again by gaining heat in the liquid line. The element that lowers the saturation temperature by decreasing the pressure on the refrigerant is the expansion element. Figure 1 illustrates the transformation of the refrigerant from a high-pressure liquid state at point 3 to a low-pressure liquid/vapour state at point 4 through the reduction of pressure via the expansion valve. There are different types of expansion elements. Various accessories are used in the cooling cycle depending on the type used. The refrigerant, whose pressure drops, tries to evaporate by gaining heat. The heat exchanger element where this situation occurs is the evaporator. In Figure 1, at point 4, the refrigerant in the liquid/vapour state at low pressure draws heat from the environment in the evaporator and becomes saturated vapour at low pressure at point 1. In the real cycle, the refrigerant is required to leave the evaporator saturation temperature slightly warmer than the evaporator saturation temperature to shed heat in the suction line and condense again. This situation is called superheat. Thus, the refrigerant returns to the compressor as superheated steam at low

pressure. Thus, the vapour compression refrigeration cycle is completed.

Applying the principle of conservation of energy allows us to calculate the load on the evaporator.,

$$\dot{Q}_{evap} = \dot{m}_r (h_1 - h_4) \tag{1}$$

Here, the refrigerant's enthalpy is denoted by h, and its mass flow rate by $\dot{m}_r$.

If the evaporator load is known, then the refrigerant mass flow rate can be calculated using the following formula:

$$\dot{m}_r = \frac{\dot{Q}_{evap}}{(h_1 - h_4)} \tag{2}$$

According to the principle of conservation of energy, the inlet and outlet enthalpy will be equal in the expansion valve as there is no heat and work transfer;

$$h_3 = h_4 \tag{3}$$

Assuming that compression in the compressor is adiabatic, the power delivered to the refrigerant by the compressor is expressed as:

$$\dot{W}_{comp} = \dot{m}_r (h_2 - h_1) \tag{4}$$

The efficiency of the cooling system is as the ratio of evaporator load to compressor power;

$$COP = \frac{\dot{Q}_{evap}}{\dot{W}_{comp}} \tag{5}$$

Compressor outlet-inlet pressure ratio is defined as:

$$P_{ratio} = \frac{P_{cond}}{P_{evap}} \tag{6}$$

Compressor discharge temperature was obtained using the refrigerant superheated steam tables in the REFPROP 9.1 [23] program as a function of the condenser saturation pressure and the enthalpy values of the refrigerant at point 2.

$$T_{dis} = f(P_{cond}, h_2) \tag{7}$$

Thermodynamic properties of R134a, R1234yf, R454C and R452A refrigerants are given in Table 1. R134a and R1234yf refrigerants are pure fluids. It consists of a mixture of R32-R125-R1234yf refrigerants with R452A refrigerant and 11%-59%-30% by weight, respectively. It contains a blend of R32-R1234yf refrigerants with R454C refrigerant and 21.5%-78.5% by weight, respectively.

The comparison parameter values of the vapour compression refrigeration cycle are given in Table 2. Evaluations are based on condenser temperatures of 40 and 60 °C and evaporator temperatures increased by 5 °C between -10 and 10 °C. The superheat of the evaporator outlet refrigerants in the cooling cycle is assumed to be 6°C,

Table 1. Properties of refrigerants [8, 19, 23, 24]

ASHRAE Number	R452A	R454C	R1234yf	R134a
Molecular Mass (g mol^{-1})	103,5	90,78	114,0	102,0
Boiling Point (°C) at 1 atm	-47,0	-45,6	-29,4	-26,1
Liquid Density at 21.1°C (kg m^{-3})	1148,8	1042,4	1100	1,206
ASHRAE Class	A1	A2L	A2L	A1
Critical Temperature (°C)	74,9	85,7	94,7	101,1
Critical Pressure (bar)	40,02	43,188	33,81	40,67
GWP	2140	146	4	1430

and the subcooling temperature of the condenser outlet refrigerants is assumed to be 6°C. In addition, the compressor isentropic efficiency is supposed to be 70%, and the evaporator load is assumed to be 6 kW. Thermodynamic properties of the refrigerants to be used for evaluation in the study were found by using the REFPROP 9.1 program [23]. R134a, R1234yf, R454C and R452A refrigerants were compared depending on condenser and evaporator pressure ratio, mass flow rate, compressor power, cooling effect coefficients, and compressor outlet temperatures.

Table 2. Comparison parameters.

Input parameters	Values
Evaporator Load (kW)	5.5
Superheated temperature (°C)	8
Evaporator temperature (°C)	-6, 0, 6
Condenser temperature (°C)	40, 45, 50, 55, 60
Isentropic efficiency (%)	75
Subcooling temperature (°C)	6

3. Results and Discussion

Figure 2 depicts the comparative performance graphs of refrigerants based on evaporator temperatures from -10 to 10°C in 5°C increments and condenser temperatures of 40 °C. and 60°C.
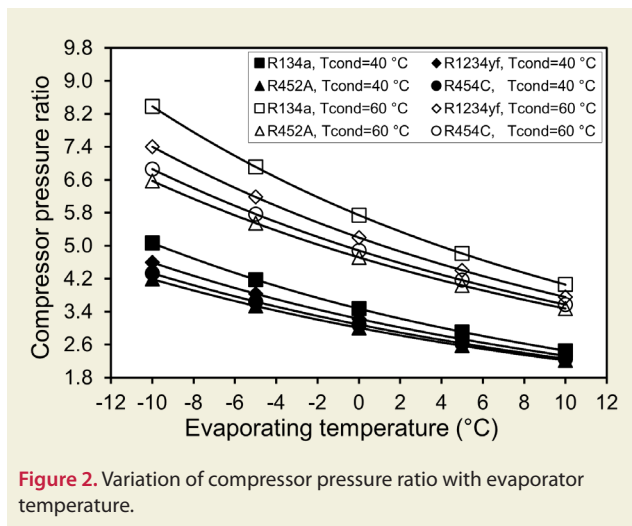

Figure 2. Variation of compressor pressure ratio with evaporator temperature.

The change in condenser and evaporator pressure ratios depending on the evaporator temperature of different refrigerants used in automobile, trailer, commercial and industrial-type cooling systems is illustrated in Figure 2. It was seen that as the evaporator temperature increased from -10°C to 10°C, the R134a, R1234yf, R452A and R454C condenser and evaporator pressure ratios decreased by about 51.6%, 49.3%, 47.2% and 47.9%, respectively. It was observed that as the condenser temperature increased from 40°C to 60°C, the R134a, R1234yf, R452A and R454C condenser and evaporator pressure ratios increased by approximately 65.4%, 61.2%, 56.9% and 58.3%, respectively. It has been observed that R134a has an average of approximately 8.4%, 15.7% and 13.1% higher condenser and evaporator pressure ratios than R1234yf, R452A and R454C, respectively.

Changes in the refrigerant mass flow rate depending on the evaporator temperature of different refrigerants used in automobile, trailer, commercial and industrial-type cooling systems is presented in Figure 3. It is seen that as the evaporator temperature increases from -10°C to 10°C, the refrigerant mass flow rates of R134a, R1234yf, R452A and R454C decrease by approximately 8.4%, 12.0%, 9.7% and 8.1%, respectively. It is understood that as the condenser temperature increases from 40°C to 60°C, the R134a, R1234yf, R452A and R454C refrigerant mass flow rates increase by approximately 24.1%, 32.2%, 37.6% and 27.1%, respectively. The results presented in Figure 3 indicate that R134a has approximately 31.9%, 38.8% and 4.2% less refrigerant mass flow rate than R1234yf, R452A and R454C, respectively.
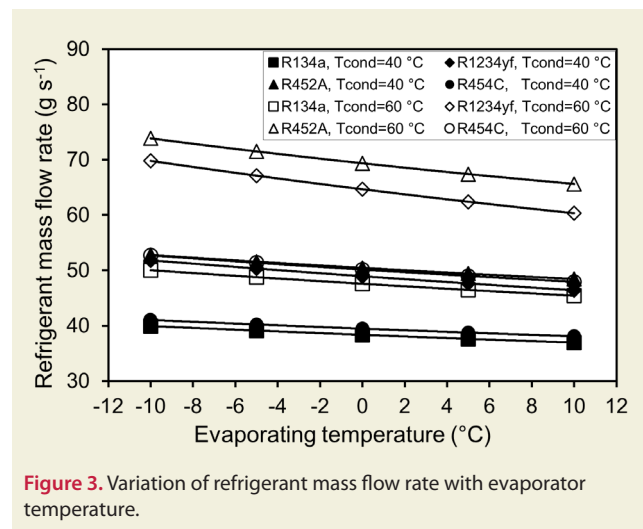

Figure 3. Variation of refrigerant mass flow rate with evaporator temperature.

The change in compressor power depending on the evaporator temperature and, changes in COP depending on the evaporator temperature of different refrigerants are shown in Figure 4 and Figure 5 respectively. It is understood that as the evaporator temperature increases from -10°C to 10°C, the compressor power of R134a, R1234yf, R452A and R454C decreases by approximately 44.9%, 44.5%, 47.9% and 46.5%, respectively. It is seen that as the condenser temperature increases from 40°C to 60°C, the compressor power of R134a, R1234yf, R452A and

R454C increases by approximately 76.4%, 85.3%, 96.1% and 80.1%, respectively. Besides, R134a has approximately 5.8%, 9.9% and 0.7% less compressor power on average than R1234yf, R452A and R454C, respectively. It is seen that the compressor powers of R134a, R1234yf, R452A and R454C are in the range of 1.01 - 3.28 kW, 1.03 - 3.62 kW, 1.02 - 3.88 kW and 0.98 - 3.36 kW, respectively, according to the theoretical analysis conditions.
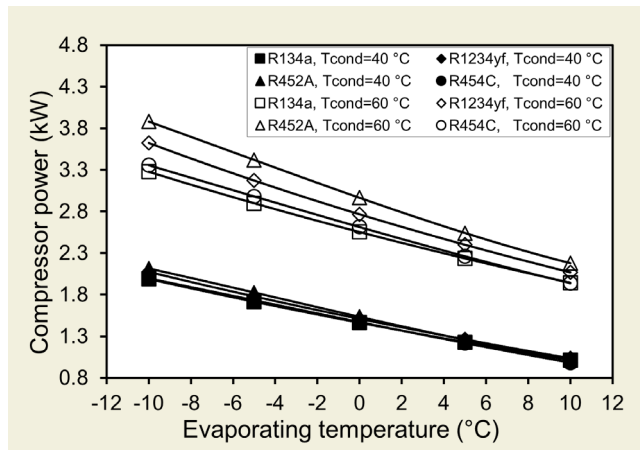

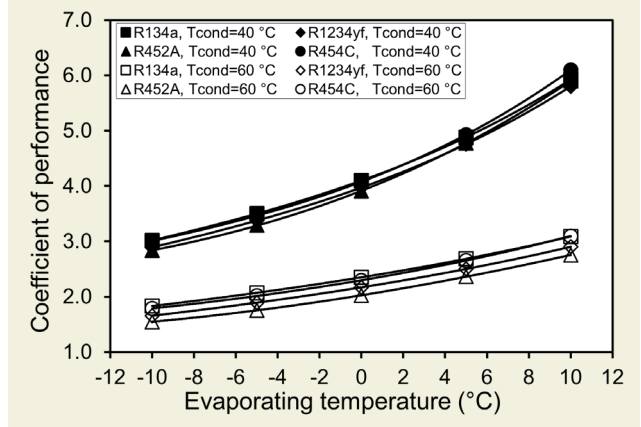**Figure 4.** Variation of compressor power with evaporator temperature.

Figure 5. Variation of COP with evaporator temperature.

Changes in COP depending on the evaporator temperature of different refrigerants used in automobile, trailer, commercial and industrial-type cooling systems is given in Figure 5. It is observed that the evaporator temperature rises from -10°C to 10°C, the COP of R134a, R1234yf, R452A and R454C increases by approximately 82.5%, 87.9%, 93.1% and 87.9% as shown in Figure 5, respectively. It is observed that as the condenser temperature increases from 40°C to 60°C, the COP of R134a, R1234yf, R452A and R454C decreases by nearly 43.2%, 45.9%, 48.8% and 44.3%, respectively. R134a appears to have an average of about 5.4%, 8.6% and 0.6% higher COP than R1234yf, R452A and R454C, respectively. The results were found to be compatible with Mostafa et al. [16] and Alkan and M.S İnan [18].

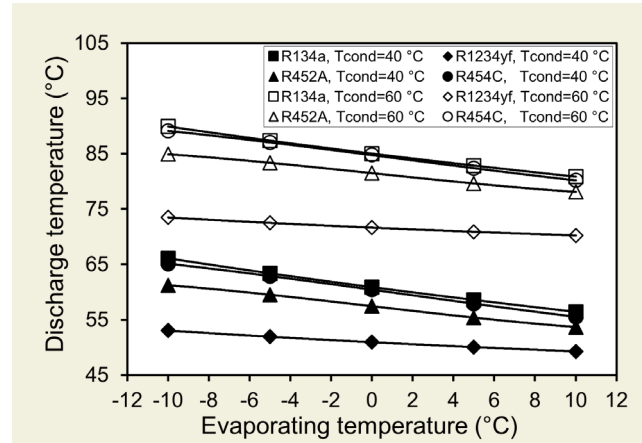Figure 6 represent the changes in compressor discharge

Figure 6. Variation of refrigerant compressor discharge temperature with evaporator temperature.

temperature depending on the evaporator temperature of different refrigerants. It has been determined that as the evaporator temperature increases from -10°C to 10°C, R134a, R1234yf, R452A and R454C refrigerants reduce the compressor discharge temperatures by approximately 12.4%, 5.8%, 10.2% and 12.4%, respectively. It is seen that as the condenser temperature increases from 40°C to 60°C, the compressor discharge temperatures of R134a, R1234yf, R452A and R454C systems increase by approximately 24.1%, 20.7%, 24.1% and 24.3%, respectively. Moreover, the R1234yf system has an average of 13.8% less compressor discharge temperature than the R455A system. It is also observed that R134a has an average of approximately 16.1%, 4.11% and 0.9% less compressor discharge temperature than R1234yf, R452A and R454C, respectively. Based on the theoretical analysis conditions in the study, compressor discharge temperatures of R134a, R1234yf, R452A and R454C are in the range of 56.42 - 89.92 °C, 49.26 - 73.47 °C, 53.67 - 84.91 °C and 55.52 - 89.12 °C, respectively.

4. Conclusions

In this theoretical study, the performances of refrigerants R134a, R1234yf, R452A, and R454C used in automobile, trailer, commercial and industrial cooling systems were compared based on their evaporator and condenser temperatures. Thus, the performances of alternative refrigerants used in different cooling systems under similar conditions were comparatively evaluated. Thermodynamic properties of refrigerants were found using the REFPROP 9.1 program. The main results obtained from the comparative theoretical analysis results of the R134a, R1234yf, R452C and R454C refrigerant systems are given below.

- R134a was found to have on average about 8.4%, 15.7% and 13.1% higher condenser and evaporator pressure ratios than R1234yf, R452A and R454C, respectively.

- It was found that the refrigerant with the highest compressor power and mass flow rate was R452A,

followed by R1234yf, R454C and R134a.

- R134a was found to have 31.9%, 38.8% and 4.2% lower mass flow than R1234yf, R452A and R454C, respectively.

- The compressor powers of R134a, R1234yf, R452A and R454C were found to be in the range of 1.01 - 3.28 kW, 1.03 - 3.62 kW, 1.02 - 3.88 kW and 0.98 - 3.36 kW, respectively, according to the theoretical analysis conditions.

- R134a showed an average COP almost 5.4%, 8.6% and 0.6% higher than R1234yf, R452A and R454C, respectively.

- It was observed that the compressor discharge temperatures of R134a, R1234yf, R452A and R454C were in the range of 56.42 – 89.92 °C, 49.26 – 73.47 °C, 53.67 – 84.91 °C and 55.52 – 89.12 °C, respectively, according to theoretical analysis conditions.

- When the temperature of the evaporator increases, the COP increases, while the pressure ratio at the compressor inlet and outlet, the refrigerant mass flow rate, the compressor capacity and the compressor outlet temperature decrease.

- It has been observed that increasing the condenser temperature results in decreasing the compressor inlet-outlet pressure ratio, refrigerant mass flow rate, COP, and compressor power while increasing the compressor discharge temperature.

Conflict of Interest Statement

The author must declare that there is no conflict of interest in the study.

References

[1] Zadeh, P. G., & Chung, J. D. (2024). Exploring adsorption refrigeration for automobile air-conditioning: A comprehensive review. Applied Thermal Engineering, 122390.

[2] Estevez, R., Aguado-Deblas, L., López-Tenllado, F. J., Bautista, F. M., Romero, A. A., & Luna, D. (2024). Internal Combustion Engines and Carbon-Neutral Fuels: A Perspective on Emission Neutrality in the European Union. Energies, 17(5), 1172.

[3] Günaydin, S., Uyumaz, A., Kocakulak, T., Coşman, S., Solmaz, H., & Aksoy, F. (2024). Evaluation of dibutyl maleate/diesel blends on combustion, performance and emissions in a DI diesel engine. Applied Thermal Engineering, 236, 121520.

[4] Coşman, S. (2023). Experimental Research of the Effects of Benzoylthiourea Derivative Fuel and Gasoline Mixtures on Engine Performance and Emissions. International Journal of Automotive Science and Technology, 7(4), 403-409.

[5] UNEP, (1987). Montreal Protocol on Substances that Deplete the Ozone Layer. Final Act. United Nations, New York.

[6] Global Environmental Change Report GCRP, (1997). A Brief Analysis Kyoto Protocol, vol. IX, p. 24.

[7] European Union. (2014). "Regulation (EU) No 517/2014 of the European Parliament and of the Council of 16 April 2014 on fluorinated greenhouse gases and repealing regulation (EC) no 842/2006 (1)." Official Journal of European Union 57, 195-230.

[8] American Society of Heating, (2013). Refrigerating and Air-Conditioning Engineers, Inc. ASHRAE Standard 34 Designation and Safety Classification of Refrigerants.

[9] Oruç V, Devecioğlu AG. (2021). Experimental investigation on the low-GWP HFC/HFO blends R454A and R454C in a R404A refrigeration system, Int. J. Refrig, 128, 242–251. https://doi.org/10.1016/j.ijrefrig.2021.04.007

[10] Zhang Z, Wang J, Feng X, Chang L, Chen Y, Wang X. (2018). The solutions to electric vehicle air conditioning systems: A review. Renew Sust Energ Rev., 91, 443–63. https://doi.org/10.1016/j.rser.2018.04.005.

[11] Daviran, S., Kasaeian, A., Golzari, S., Mahian, O., Nasirivatan, S., Wongwises, S.,. (2017). A comparative study on the performance of HFO-1234yf and HFC-134a as an alternative in automotive air conditioning systems. Appl Therm Eng. 110, 1091–1100. https://doi.org/10.1016/j.applthermaleng.2016.09.034

[12] Zilio C, Brown JS, Schiochet G, Cavallini A. (2011). The refrigerant R1234yf in air conditioning systems. Energy, 36, 6110–20. https://doi.org/10.1016/j.energy.2011.08.002

[13] Direk M, Yüksel F. (2019). Comparative experimental evaluation on heating performance of a mobile air conditioning system using R134a, R1234ze(E), R152a and R444a. J Thermal Sciences and Technology, 39,31–38.

[14] Cho H, Park C. (2016). Experimental investigation of performance and exergy analysis of automotive air conditioning systems using refrigerant R1234yf at various compressor speeds. Appl Therm Eng., 101,30–7. https://doi.org/10.1016/j.applthermaleng.2016.01.153

[15] Golzari, S., Kasaeian, A., Daviran, S., Mahian, O., Wongwises, S., Sahin, A.Z., (2017). Second law analysis of an automotive air conditioning system using HFO-1234yf, an environmentally friendly refrigerant. Int. J. Refrig., 73, 134–143. https://doi.org/10.1016/j.ijrefrig.2016.09.009

[16] Mostafa, A., Hassanain, M., Elgendy, E. (2021). An experimental study of R-454C pull-down performance as a drop-in refrigerant in a walk-in cold store system, Int. J. Refrig. 130, 170–178. https://doi.org/10.1016/j.ijrefrig.2021.05.029.

[17] Aral, M. C., Suhermanto, M., Hosoz, M. (2021). Performance evaluation of an automotive air conditioning and heat pump system using R1234yf and R134a. Science and Technology for the Built Environment, 27, 44–60. https://doi.org/10.1080/23744731.2020.1776067

[18] Inan, M. S., and Alkan, A. (2023). Performance Analysis of Different Refrigerants in Automobile Air Conditioning Equipment Using Variable Capacity Compressor. International Journal of Automotive Science and Technology, 5(4), 372-377. https://doi.org/10.30939/ijastech.992262

[19] Alkan, A., Inan, M.S., (2023). Experimental investigation of the effects of compressor types on the performance of an automobile air conditioning system using R1234yf. International Journal of Refrigeration, 155, 58-66. https://doi.org/10.1016/j.ijrefrig.2023.09.004

[20] Devecioğlu AG., Oruç V. (2021). Experimental comparison of

R404A and R452A in refrigeration systems, Sci. Technol. Built Environ, 27(1), 61–69. https://doi.org/10.1080/23744731.2020.1796419

[21] Devecioğlu AG., Oruç V. (2023). Soğutma sistemlerinde R454C kullanılmasının deneysel incelenmesi. Journal of Polytechnic, 26(1), 153-160. https://doi.org/10.2339/politeknik.898828

[22] Khatoon S. and Karimi MN. (2023). Thermodynamic analysis of two evaporator vapor compression refrigeration system with low GWP refrigerants in automobiles, Int. J. Air-Conditioning Refrig., vol. 31(1), 1-17 doi: 10.1007/s44189-022-00017-1

[23] Lemmon, E.W. , Bell, I.H. , Huber, M.L. , McLinden, M.O. (2018). NIST Standard Reference Database 23: Reference Fluid Thermodynamic and Transport Properties-REF- PROP, Version 10.0. National Institute of Standards and Technology, Standard Reference Data Program, Gaithersburg.

[24] Honeywell, 2017, Solstice R452A, (https://www.honeywell-refrigerants.com/europe/wp-   content/uploads/2017/10/FPR-029-2017-09_Solstice_452A_A4_2892017.pdf).